Time Resolved Momentum Microscopy on Strongly Correlated Materials

Dissertation
zur Erlangung des Grades
Doktor der Naturwissenschaften (Dr. rer. nat.)
am Fachbereich Physik, Mathematik und Informatik
der Johannes Gutenberg-Universität Mainz

von:
Steinn Ýmir Ágústsson
geboren in Reykjavík (IS)
Mainz, 2022

Steinn Ýmir Ágústsson
Time Resolved Momentum Microscopy on Strongly Correlated Materials

Datum der mündlichen Prüfung: *8. März, 2022*

Gutachter:	Prof. Dr. Jure Demsar
	omitted in online version
Kommission:	*omitted in online version*
	omitted in online version
Vorsitz:	*omitted in online version*

Johannes Gutenberg Universität Mainz
AG Demsar
Institut für Physik
Staudingerweg 7
55128, Mainz

Eidesstattliche Erklärung

Hiermit erkläre ich an Eides statt, dass ich meine Dissertation selbständig und ohne fremde Hilfe verfasst und keine anderen als die von mir angegebenen Quellen und Hilfsmittel zur Erstellung meiner Dissertation verwendet habe. Die Arbeit ist in vorliegender oder ähnlicher Form bei keiner anderen Prüfungsbehörde zur Erlangung eines Doktorgrades eingereicht worden.

Mainz, den

Steinn Ýmir Ágústsson

Abstract

Intriguing phenomena in strongly correlated electron systems arise from the interplay between multiple degrees of freedom. Time-resolved Momentum Microscopy (trMM) is the ideal tool for studies of such systems. It provides access to copulings between these degrees of freedom (charge, spin and lattice) by studying their dynamics upon optical excitation on the femtosecond timescale. This is crucial for the understanding of many open questions as e.g. the nature of photodoping in antiferromagnetic Mott insulators. To this end we applied trMM to study the dynamics of photodoping in a parent compound of a prototypical high-T_c superconductor: La_2CuO_4 (LCO). These results suggest that upon excitations in-gap states are formed, in agreement with previous indirect observations from core level spectroscopy.[1]

From a wider perspective, Multidimensional Photoemission Spectroscopy (MPES), as the generalization of photoemission spectroscopy beyond the 3 dimensions (energy and parallel momenta), can help shed light on different exotic phenomena. Using High Energy X-Ray Photoelectron Spectroscopy (HAXPES), we investigated the prototypical Kondo compound $YbRh_2Si_2$, resolving the full 3D momentum space to track the transition between a large and small Fermi surface, as a function of temperature.

In this Thesis, great attention is dedicated to the description of the methods we developed to efficiently process (photo)electron resolved data streams, recorded together with a large set of parameters that identify the experimental conditions in which each electrons was detected. Among these parameters, timing jitters, photon energies, excitation laser fluence and many others can be used to correct artifacts and calibrate physical axes (i.e. convert time-of-flight (ToF) to kinetic energy). This delivers a data

structure which makes it possible to exploit fluctuations and isolate outliers and artifacts, to greatly increase information density and signal-to-noise ratio (SNR) ratio of these complex experiments. Furthermore, parametric correction methods allow to track the changes applied to the raw data, enabling full reproducibility of the workflow applied. This is one of the key ingredients for data and data processing/analysis tools to be future-proof and ready for the application novel Artificial Intelligence (AI) methods.

Contents

Acronyms

AFM	antiferromagnetic. 6, 8, 96
AI	Artificial Intelligence. iv, 3, 4, 29, 42, 122
ARPES	Angle Resolved Photoelectron Spectroscopy. 14, 15, 19, 98
BAM	Beam Arrival Monitor. 25, 57, 58, 61
BBO	Beta-Barium Borate. 58
Bi2212	$Bi_2Sr_2CaCuO_{8+y}$. 96, 103, 114, 118, 119, 124
BZ	Brillouin Zone. 15, 87, 89, 90, 96, 108, 116–118, 123
CB	Conduction Band. 100, 113
CCD	Charge-coupled device. 18, 31
DAQ	Data Acquisition System. 33, 35, 37
DESY	Deutsches Elektronen-Synchrotron. 5, 21, 32, 40, 86, 123
DFT	Density Functional Theory. 3
DLD	delay-line-detector. 16–18, 21, 31, 32, 36–38, 43, 46, 48, 52, 68, 69, 88, 118, 122
DOS	Density of States. 6–8, 97
EDC	Energy Distribution Curve. 6–8, 11, 33, 48–52, 59, 62, 73, 75–80, 84, 90, 91, 98, 104, 107–111, 113, 115
ESCA	Electron Spectroscopy for Chemical Analysis. 14
FEL	Free Electron Laser. 14–16, 19, 21–26, 32, 35–37, 41, 57, 62, 64, 67, 70, 73, 75, 77, 78
FLASH	Free-electron -LASer in Hamburg. 2, 5, 6, 21, 22, 25–27, 30, 32–35, 50, 57, 63, 69, 76, 78, 95, 102, 105, 107, 121, 123
FM	ferromagnetic. 6–8

FOV	Field of View. 2, 16, 26, 38, 53, 54, 56, 79, 83, 86, 87, 93, 108, 116, 123
FWHM	Full Width at Half Maximum. 21, 23, 24, 26, 61, 65, 112
HAXPES	High Energy X-Ray Photoelectron Spectroscopy. iii, 2, 54, 55, 83, 85, 92
HEXTOF	High Energy X-ray Time of Flight. 2, 5, 21, 23, 24, 26, 27, 30, 32, 33, 35, 36, 38, 46, 56, 60, 64, 69, 75, 76, 85, 95, 107, 121
HHG	High Harmonic Generation. 14–16
LAPE	Laser-Assisted PhotoEmission. 77
LBCO	$La_{2-x}Ba_xCuO_4$. 95
LCO	La_2CuO_4. iii, 8, 50, 52, 60, 72, 95, 96, 101–108, 112, 114, 115, 117–119, 123–125
LDA	Local-Density Approximation. 98
LHB	Lower Hubbard Band. 99
LSCO	$La_{2-x}Sr_xCuO_4$. 95, 96, 98, 102, 106–109, 112, 113
MCP	Multi-Channel Plate. 17, 18
MD	Molecular Dynamics. 3
MDC	Momentum Distribution Curve. 33, 91
MIR	Mid-InfraRed. 100, 101, 118
ML	Machine Learning. 3, 29, 42
MM	Momentum Microscopy. 2, 9, 17, 19, 29, 36, 62, 71
MPES	Multidimensional Photoemission Spectroscopy. iii, 1, 30, 42, 122
nPPE	multi-photon photoemission. 59, 60, 63–66, 73
openCOMPES	Open Community of Multidimensional Photoemission Spectroscopy. 42
RF	Radio-Frequency. 22, 25
ROI	Region of Interest. 26
SASE	Self-Amplified Spontaneous Emission. 22, 25, 57
SC	Space-Charge. 7, 19, 20, 24, 26, 35, 45, 50, 69–71, 73–76, 78–81, 104, 112, 116, 122
SCam	Streak Camera. 25, 57, 58, 61, 67, 68

SED	Single Event Data frame. 5, 31–41, 43, 48–51, 55, 67, 87, 88, 112, 121, 123
SNR	signal-to-noise ratio. iv, 43, 66, 92, 112, 116, 124
ToF	time-of-flight. iii, 5, 16, 17, 26, 31, 46–51, 62, 79
trMM	time-resolved Momentum Microscopy. iii, 2, 5, 9, 20, 27, 29, 30, 38, 114
UHB	Upper Hubbard Band. 99
UHV	Ultra-High Vacuum. 109
VB	Valence Band. 99, 100, 107–109, 111, 113, 114
VUV	Vacuum UltraViolet. 22
XPS	X-ray Photoelectron Spectroscopy. 14, 106, 107
XUV	eXtreme UltraViolet. 21, 63
YBCO	$YBa_2Cu_3O_{7-y}$. 96, 119, 124

CHAPTER 1

INTRODUCTION

Strongly correlated electron systems have been at the forefront of research in condensed matter physics for decades. However the physics behind many body interactions still remain elusive. In particular, the microscopic origin of superconductivity in high-T_c superconductors is still unclear, as the complex interplay among many degrees of freedom make it difficult to achieve consensus across a large community.

There is wide consensus on the crucial role that the electronic structure near to the Fermi level plays in superconductivity, as well as in other correlated electron systems such as heavy fermion materials, spintronic materials and multiferroics. Photoemission spectroscopy is therefore the ideal tool to investigate such systems, as it makes it possible to directly explore the electronic structure at the low binding energies. Besides, studying the dynamics of such systems upon optical excitation, can shed light on the coupling between the different degrees of freedom, different long range orders and their interplay.

The work presented in this Thesis focuses on the experimental technique of Multidimensional Photoemission Spectroscopy (MPES), where at least 4 dimensions are

recorded, simultaneously. First we present the High Energy X-Ray Photoelectron Spectroscopy (HAXPES) investigations of the temperature dependence of the Kondo system $YbRh_2Si_2$.[2] The high photon energy of 5 keV used, allowed us to obtain both bulk sensitivity and a large Field of View (FOV), with varying perpendicular momentum k_z. We exploited such variations to reconstruct 3D energy isosurfaces and track the transition between small and large Fermi surfaces in this compound as a function of temperature. Our data suggests such a transition takes place between 100 K and 200 K, far above the Kondo temperature T_k.

The time-resolved photoemission studies of the superconducting cuprate parent compound La_2CuO_4 constitute the main results presented in this Thesis. The experiments, performed with the Momentum Microscopy (MM) High Energy X-ray Time of Flight (HEXTOF) at the Free-electron -LASer in Hamburg (FLASH), focused on the transient electronic structure of this Mott insulator, upon photoexcitation with 3.1 eV photons, inducing excitations across the charge-transfer gap. Time-resolved all-optical studies[3,4] show a parallelism between optical excitations and chemical doping, with the shift of spectral weight to a resonance at 0.5 eV, within the optical gap. The single-particle picture provided by photoemission experiments, as opposed to tracking optical excitations (2-particle process) may allow the identification of the origin of such a resonance in the electronic structure. Our time-resolved Momentum Microscopy (trMM) studies suggest the formation of photoinduced in-gap states, with dynamics on the same time-scale as the one observed for the 0.5 eV resonance in all-optical measurements.

Multidimensional photoemission experiments face various challenges, from the extreme surface sensitivity to the complex experimental setups required. An increasingly important role is played by data acquisition and processing, which has in the recent years grown by orders of magnitude in size and complexity, up to the point it is being called a new paradigm of science.

The field of material science has evolved over millennia. From the first discoveries

enabling us how to make use of stones and then how to melt and forge metals to make tools to improve conditions of life and work. These development were most probably achieved by trial-and-error, and therefore took "ages" (stone age, bronze age, iron age...) before another step forward was made. This empirical approach can be seen as the first paradigm of material science.

The development of the hypothetical deductive scientific experimental method is at the very heart of the second paradigm. Structured experiments became the cornerstone of scientific research, as we started understanding relations between different phenomena. The second paradigm is therefore defined by the introduction of theoretical, or model-based science. The use of mathematical models, provided a powerful framework to describe the observations we made with our empirical experiments.

The advent of computers in the 1950s paved the way for a third paradigm. The development of computational methods such as Density Functional Theory (DFT) and Molecular Dynamics (MD) allowed to simulate the models we could describe mathematically. Experimental results could then be directly compared to the mathematical models. This ever increasing computational capacity has driven material research over the last decades and pushed the generation of more and more data.

In recent years, the scale of the generation of such data has exploded, and has brought us to the fourth paradigm: data-driven science. The increased computational power that has given rise to ever more detailed and vast simulations, coupled together with sensors and detectors acquiring experimental data at unprecedented rates, has opened the way to more advanced analytical methods, but more importantly to a completely new approach to materials discovery and design.[5] This has taken shape in the field of *material informatics*.

Artificial Intelligence (AI) and Machine Learning (ML), processing enormous sets of experimental data are able to find hidden correlations which can go beyond our model-based understanding. These new approaches and tools can shed light on novel material

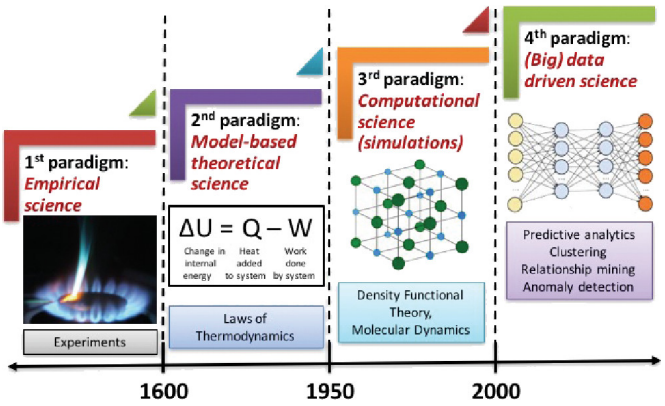

Figure 1.1: The historical evolution of the paradigms of (material) science. From Agrawal and Choudhary [5].

properties as well as give new perspectives on those which are still not fully understood.

However, a considerable and sustained effort is needed in all levels of the scientific community to harness the power and potentiality of these new tools. This has inspired the formation of many large material science databases[6–10], with the goal of collecting experimental and simulated data from a vast variety of experimental techniques and transform the heterogeneous landscape of data in material science, to AI-ready. The F.A.I.R. principles[11] present guidelines on how to think about data, in the framework of data-driven science.

The efforts needed to consolidate this new paradigm cannot come exclusively from above, with institutes and research partners gathering to create the large infrastructure required. An equally important step needs to be taken by the individual scientists, who need to re-think how to change their experimental habits to fulfil the requirements of this new scientific approach.

The raw data produced during an experiment can all too often realistically only be interpreted by the scientist who performed the experiment, and not even by his colleagues working in the same field. Open source development of software and data formats is crucial to overcome such barriers, as it provides clear and transparent view on all steps in data processing. Innovative workflows systems, built with open source processing meth-

ods, are therefore essential to ensure portable, maintainable, reproducible and shareable data.[12]

In this thesis I present the work I have carried out in the field of photoemission spectroscopy, in collaboration with many other researchers at different institutions in Germany and abroad. Most of this work is based on the experimental data obtained from the HEXTOF end-station installed at FLASH at Deutsches Elektronen-Synchrotron (DESY) in Hamburg. Throughout the first chapters, I introduce the trMM technique which we used to study a variety of different materials over the last years.

Chapter 3 presents an overview of the novel workflow we have developed. It explains in detail the path between raw data and the final, ready-for-analysis data structures. In this chapter I introduce the Single Event Data frame (SED), a data structure we developed to handle the stream of detected events (photoemitted electrons) with an arbitrarily large parameter space, that can fully describe the conditions at which each event is recorded.

I then illustrate in detail most of the data processing methods developed to run the workflow, from calibrating experimentally measured quantities into physical quantities of interest (e.g. time-of-flight (ToF) to energy) to artifact corrections and denoising methods.

I dedicated most of my time as a doctoral student to the development and implementation of such methods, exclusively in open-source projects, and cultivating collaborations with other like-minded researchers whenever possible. This has led me to participate in many and various experimental efforts where many diverse material systems and different physics was under scrutiny. As is always the case with new complex experimental setups, many difficulties arise in the early experiments. Many of these raised from simply accessing the recorded data, which made it clear that in order to run such complex experiments, together with beamline scientists and machine operators, a *data scientist* is also required. This data scientist needs to have solid expertise that can bring together

data science and physics.

The cause of these difficulties lies in the high dimensionality of the data, with inherent 3D detection (energy and two momentum components) of the momentum microscope, coupled with a pump-probe scheme resolving excitation dynamics time scale. The four physical quantities measured were then recorded in parallel with more than 20 selected relevant parameters (of the over 200 provided by FLASH). These parameters include jitters and intensity monitors which were used both to monitor and to correct fluctuations throughout the measurements. This will all be described in detail in Chapter 4.

These post-processing methods allow calibration and correction of data using measured parameters, as for example the energy axis can be computed from the time-of-flight by evaluating photon energy and electric potentials applied between sample and input lens (see Section 4.1). Such calibrations and many of the corrections can be applied directly for rapid data evaluation, even during the data acquisition. This is extremely important during valuable beam-times, where for an experiment one is typically assigned just a few days of data acquisition time. Making the right decision, about how long to integrate a certain measurement, or to change a parameter, for example the excitation laser fluence, based on how it is really affecting the data, can save time and result in more data recorded[1].

A good example of successful decision-making based on data evaluation, are the results obtained on FeRh, published by Pressacco et al. [13]. This metallic compound undergoes a phase transition from antiferromagnetic (AFM) to ferromagnetic (FM) at $\approx$ 400 K, which can also be triggered by laser excitation.[14] The aim of the experiment was to observe the changes induced by laser excitation on the picosecond time scale to the electronic structure, by studying the Energy Distribution Curve (EDC). The EDC can be obtained as $DOS(E) \times f_{FD}(T)$ where the Density of States (DOS) represents the num-

[1]This is evaluated as a difference of effective acquisition time in the first beam-times I participated in, where less than 30% of the available time was used for valuable data acquisition, against the later beam-times, in which more than 80% of the acquisition time recorded significant data.

ber of electron states at energy E, while $f_{FD}(T)$ is the Fermi distribution at temperature T.

We identified a "peak" in the signal close to the Fermi energy which is typical of the FM phase and wrote a small analysis routine to evaluate the relative strength of this feature as a function of delay after the excitation pulse. This evaluation allowed us to selectively detect the optimal excitation fluence to minimize Space-Charge (SC) effects (described in Section 4.5) and yet maximise the photoinduced effect.

The results obtained are plotted in Figure 1.2, where in panel a, the EDC is plotted as function of time delay, showing a prominent signal at the time overlap $t = 0$ ps. The right panel shows the EDC after subtraction of the average EDC before the laser excitation. The aforementioned peak at the Fermi energy is clearly visible in pink, close to the dotted line at $E = E_F$.

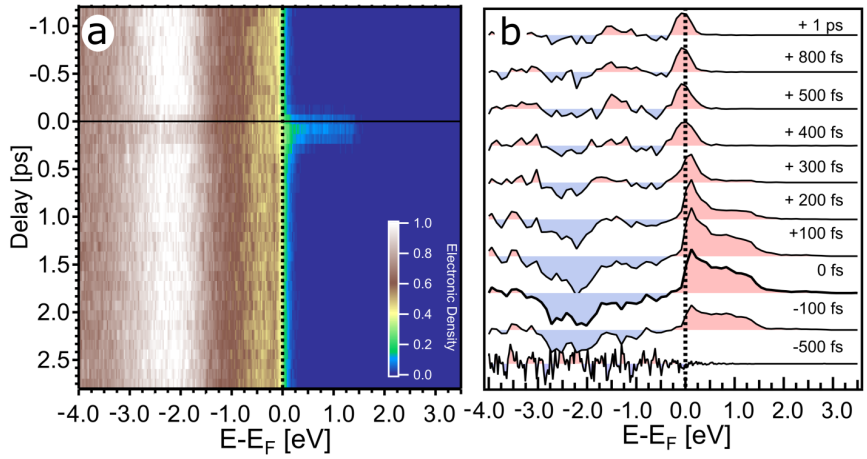

Figure 1.2: In a, EDC of FeRh as function of time delay form an excitation pulse. In b, the EDCs after subtracting the EDC integrated at negative time delays. Adapted from Pressacco et al. [13]

The signal at time zero shows a peculiar redistribution of charge. Normally, optical excitation induce changes in the Fermi distribution only, i.e. $f_{FD}(T, t)$ is time dependent while the DOS is constant. Here the results indicate a major change in the electronic structure, which is manifested in the changes in the DOS. These changes can be observed

in panel (b) of Figure 1.2, where the EDCs is plotted as function of time, after subtracting EDC before excitation. Typically, a symmetric change with respect to the Fermi level is expected in a metal, while here, the non symmetric distribution indicates the presence of changes in the DOS as well. This change in the band structure results in a relaxation on the 200 fs time scale towards the electronic structure of the FM state, and not to the initial AFM state.

When combined with previous measurements, which show a 10 ps time scale for the structural change which follow the phase transition, and a 200 ps time scale for the full magnetization, governed by domain alignment, these results allowed us to clock the full phase transition from the early time scale until the full reconstruction of the macroscopic magnetic phase.

As the work just described was done in a large collaboration with other groups, I omitted the full description from this thesis, and leave the interested reader to look up the published article instead.

The last two chapters, will present the results of the two main scientific topics introduced earlier. Chapter 5 is the study of the Kondo compound $YbRh_2Si_2$, and Chapter 6, contains the investigation of photodoping in the cuprate parent compound La_2CuO_4 (LCO).

CHAPTER 2

Momentum Microscopy

The main experimental technique used for the work presented in this Thesis is MM, a form of Photoemission Spectroscopy. In this chapter, at first, the background and basic principles of this experimental technique are presented. Then, after describing the specific variant of this technique trMM, the details of the experimental setup which produced the majority of the data presented in this Thesis will be given.

2.1 Photoemission Theory

Photoemission spectroscopy is a powerful tool, which enables the study of the electronic structure of crystals and molecules.[15–17] It is of relevance in many different fields and has a profound impact not only in solid state physics, where it furthers understanding some of its most intriguing phenomena, such as high T_c superconductivity[18,19] and topological insulators, but also in surface chemistry and material science in general.

The interactions between light and charge were first investigated through the photovoltaic effect in 1839 by Alexandre Edmond Becquerel. Although fundamentally different, this effect was instrumental in developing the interaction between electromagnetic waves and charge, which led to the discovery of the photoelectric effect by Heinrich

Hertz in 1887.[20] He observed that a spark could be seen when illuminating a metal with ultraviolet light.

It was not until 1905 when Albert Einstein, in one of his *Annus Mirabilis papers*[21] proposed a mathematical description, where interactions of photons with matter were the origin the photoelectric effect. He expressed this in terms of the maximum kinetic energy a photoemitted electron could have, as:

$$E_{Kin}^{max} = h\nu - \Phi_0, \tag{2.1}$$

where $h\nu$ introduces the concept of photons, as quanta of light with energy proportional to frequency, through the constant h, later called the *Planck constant*. Φ_0 is a characteristic constant of the surface of the sample, the so called work function, and indicates the minimum energy an electron needs to be removed from the sample to vacuum. This fundamental photoemission equation awarded Einstein the Nobel Prize in Physics in 1921 for the "discovery of the law of the photoelectric effect". In 1914 Robert Millikan, with the results from his oil drop experiment, supported this model.[22] He was also later awarded the Nobel Price in Physics in 1923 for "his work on the elementary charge of electricity and on the photoelectric effect".

Over a century of development of the "photon-in electron-out" experiments have drastically changed in efficiency, complexity and applications, but are still based on on the same principle. Photons with sufficiently high (monochromatic) energy (typically ultraviolet or X-ray, in the range of a few electronvolts 1 eV to 10 keV) excite electrons from a sample (crystal, molecule...) which are then detected by an analyzer sensitive to the electrons kinetic energy and emission angle.

Kinetic energy and emission angle can then be mapped to the binding energy and momentum $(E_B, \vec{k})$ of the original state of the photoemitted electron. Such a description can be modelled with the intuitive *3 step model*. This assumes that the photoemission process can be divided in three independent steps:

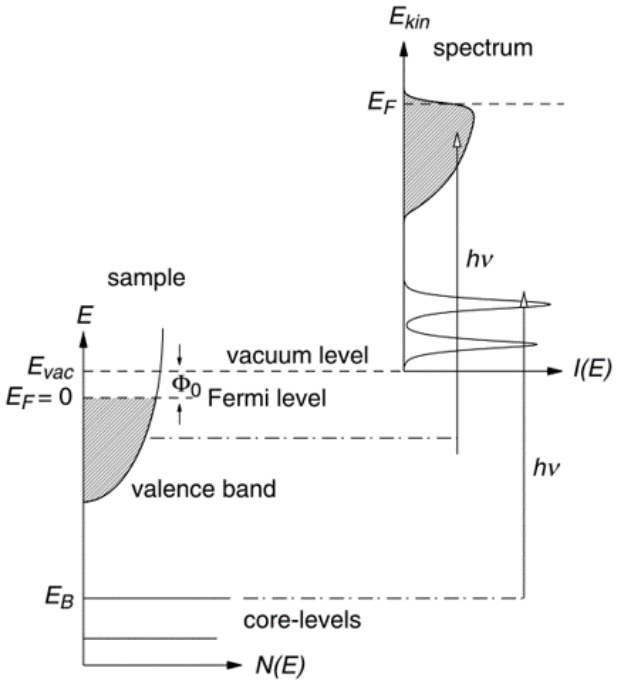

Figure 2.1: Sketch of the photoemission process. Photons with energy $h\nu$ extract electrons from a crystal to the vacuum, overcoming the work function Φ_0. Measuring the kinetic energy of the *photoemitted* electrons produces a spectrum, an Energy Distribution Curve (EDC) which describes the distribution of electronic states in the crystal. From Reinert and Hüfner [16].

- The bound electron absorbs the energy $h\nu$ of the incoming photon. Energy is fully conserved and momentum is conserved, when including the photon momentum, within multiples of the lattice vector $\vec{G}$.

- The electron travels through the crystal to its surface. Here, the electron *mean free path* defines the probability of the electron propagating without scattering and therefore conserving its energy and momentum. (In)elastically scattered electrons instead will loose all momentum information and reduce their energy, contributing only to the photoemission background. Such photoemitted electrons are often referred to as *secondary electrons* (see Section 4.5.1).

- Once at the surface, the electron needs to overcome the surface potential barrier, i.e. the work function Φ_0, to reach the free-electron-like state invacuum. The re-

maining energy and momentum define the velocity (kinetic energy) and emission angle (momentum) which will be measured by the analyser.

In this picture, the measured kinetic energy relates directly to the original binding energy as $E_{kin} = h\nu - E_B - \Phi_0$. Momentum components parallel to the surface are conserved in the photoemission process, and can be obtained as:

$$k_{||} = \frac{\sqrt{2m_e E_{kin}}}{\hbar} \sin\theta. \tag{2.2}$$

Symmetry breaking at the sample surface between the crystal and vacuum, breaks the conservation of the momentum component perpendicular to the surface $k_\perp$. This can be obtained by taking into account the electron energy loss at the surface, introducing the inner potential V_0,[23] as

$$k_\perp = \frac{\sqrt{2m_e E_{kin}\cos\theta + V_0}}{\hbar}. \tag{2.3}$$

When using high energy photons, with $h\nu > 100$ eV, the photon momentum is no longer negligible, and needs to be taken into account.[24]

This simple model is sufficient to describe most of the photoemission experiments, in which the modelling of the measured spectral features does not go into detail about line shapes, polarization effects or high energy resolutions.[16]

A more rigorous treatment of the photoemission process is the *one-step model*, in which many-body interactions are taken into account. This is done by describing the evolution of the photoemitted electron with the remaining N-1 electron system it leaves behind. In other words, the photo-current can be described as the interaction of a photon with a system in its ground state $|\Psi_i\rangle$, which brings it to its final state $\left|\Psi_f\right\rangle = \left|\Psi_{\vec{k},s}\right\rangle$ with a photoelectron of momentum $\vec{k}$ and kinetic energy $\epsilon_{\vec{k}} = \frac{\hbar^2 k^2}{2m_e}$ and a N-1 electron system:

$$J_k(h\nu) = \frac{2\pi}{\hbar} \sum_s \left| \left\langle \Psi_{\vec{k},s} \right| H_{PE} \left| \Psi_i \right\rangle \right|^2 \delta\left(\epsilon_{\vec{k}} - \epsilon_s - h\nu\right) \tag{2.4}$$

The index s stands for the combination of all possible excitations in the final state (including, for example, phonon and plasmon interactions).[16]

A common simplification required for the calculation of the spectrum is the so called *sudden approximation* (s.a.), which assumes the time for the electron to be extracted to be much faster (in the order of tens of attoseconds) than the relaxation rate for the N-1 system left behind.[25] Such an approximation consist in decoupling the photoelectron from the rest of the solid, in the final state $\left|\psi_f\right\rangle = \left|\psi_{\vec{k},s}\right\rangle$. This can be expressed as:

$$\left|\Psi_{\vec{k},s}\right\rangle = \left|\vec{k}; N-1, s\right\rangle \xrightarrow{s.a.} c^{\dagger}_{\vec{k},s}\left|N-1, s\right\rangle \tag{2.5}$$

with the photoelectron creation operator $c^{\dagger}_{\vec{k},s}$.[16] With this assumption, equation 2.4 can be written as:

$$J_k(h\nu) = \frac{2\pi}{\hbar}\sum_i \left|\Delta_{if}\right|^2 A_i\left(\epsilon_{\vec{k}} - h\nu\right) \tag{2.6}$$

with the photoemission matrix element $\Delta_{if} = \left\langle \Psi_f \right| H_{PE} \left|\Psi_i\right\rangle$ describing the transition probability for an electron from the state $\left|\Psi_i\right\rangle$ to the state $\left|\Psi_f\right\rangle$. The *spectral function* $A_i(h\nu)$ describes the probability to add or remove an electron from the ground state of a many body electron system, taking into account the response of the system to the excitation.[23] The spectral function is related, through the Fermi-Dirac distribution $f(\omega, T)$ to the imaginary part of the single particle Green's function:

$$A_i(\omega) = -\frac{1}{\pi}\Im G_i(\omega) f(\omega, T), \tag{2.7}$$

where the Green's function

$$G_k(\omega) = \frac{1}{\omega - \epsilon_i - \Sigma_i(\omega)} \tag{2.8}$$

contains all the many-body like contributions in the complex self energy $\Sigma_i(\omega)$. This term is the origin for the characteristic line shapes observed in photoemission spectra. An example is the asymmetric Doniach-Šunjić line shape for core levels.[26]

For more detailed descriptions of the theory of photoemission, we refer to Cardona and Ley [15], Hüfner [23], Kevan [27], Kittel and Holcomb [28], Rogalski and Palmer [29], and Suga and Sekiyama [30].

2.2 Photoemission Spectroscopy

In 1967, Kai Siegbahn[31] first developed the Electron Spectroscopy for Chemical Analysis (ESCA) technique, which granted him the Nobel price in 1981 "for his contribution to the development of high-resolution electron spectroscopy". His technique would today be called X-ray Photoelectron Spectroscopy (XPS), and has since gathered increasing interest and given rise to many applications throughout various fields of both physics and chemistry.

More than half a century of developments have brought photoemission to a fuller maturity in terms of energy and angle-resolving analysers. Hemispherical analysers, which have been the main workhorse for Angle Resolved Photoelectron Spectroscopy (ARPES), can reach energy resolutions down to 1 meV[32] and angle resolutions of less than 1°.[33,34]

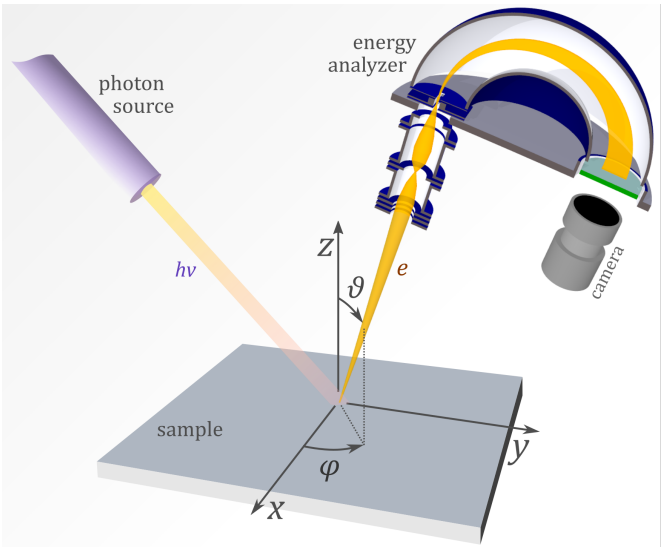

Figure 2.2: Simple cartoon of ARPES, showing the polar coordinates and rotations needed for 2D band structure mapping. Author: Ponor Licence: CC BY-SA 4.0

Moreover, advancements in photon sources such as synchrotrons, Free Electron Lasers (FELs) and table-top High Harmonic Generation (HHG) lasers, open up a whole new range of possibilities.[35] Short pulses in the femtosecond regime are now well established, and allow exploration of ultra-fast dynamics and transient states in complex correlated

materials.

Higher brilliance of synchrotrons, together with the high repetition rate of short pulsed sources like FELs and HHGs, allow photoemission experiments to move beyond the conventional energy-angle (momentum) resolved studies and increase the simultaneous parameter space recorded to time, real-space or spin. Great interest is devoted to the development of techniques able to measure the spin-state of the photoemitted electrons. This allows to characterize magnetic phenomena and disentangle the spin texture from the electronic structures.

Of greater interest for the work presented in this thesis, is the development of *time resolved* experiments, with which the ultrafast electron dynamics can be observed on the femtosecond time scale. These new tools now enable the exploration of complex systems, where the interplay between different phenomena gives rise to exotic behaviours such as high$-T_c$ superconductivity, topological insulators, 3D Weyl semimetals, Kondo lattices, charge density waves and Mott insulators.

2.3 Time-of-Flight Momentum Microscopy

Traditional ARPES setups using hemispherical analysers with a 2D detector simultaneously measure the energy and azimuthal emission angle, typically in the range of ±15 °. This angle can be directly mapped to one parallel momentum direction, but in order to resolve a 2D band structure, also the polar angle needs to be rotated (see Figure 2.2). This is usually achieved by tilting the sample, repeating the measurement for each slice. All the developments and optimizations this technique has seen over decades, has lead to systems which are capable of extremely high energy and momentum resolutions, but when it comes to measuring a large portion of momentum space, i.e. a whole Brillouin Zone (BZ) or even multiple BZs, the necessity of scanning sequences of slices makes this data acquisition procedure inefficient.

To overcome such limitations and increase detection efficiency, the group of G. Schön-

hense from the University of Mainz, in collaboration with the group of J. Kirschner from the Max Plank Institute for Microstructure Physics in Halle developed the concept of a *Momentum Microscope*.[36,37] It exploits the basic concept from optics where, in an optical imaging system, the reciprocal of an image corresponds to its *Fourier transform*. Hence, due to the conservation of parallel momentum in the photoemission process, the reciprocal image of the photoemitted electrons yields directly, in the back focal plane of a cathode-lens microscope[38,39], the projected band structure of the sample under investigation. Such a lens design enables extended mapping of the momentum space by collecting electrons from the full half sphere above the sample, maximizing the momentum FOV at any given photon energy. A schematic view of the electron trajectories through the electron optics of the momentum microscope is presented in Figure 2.3.

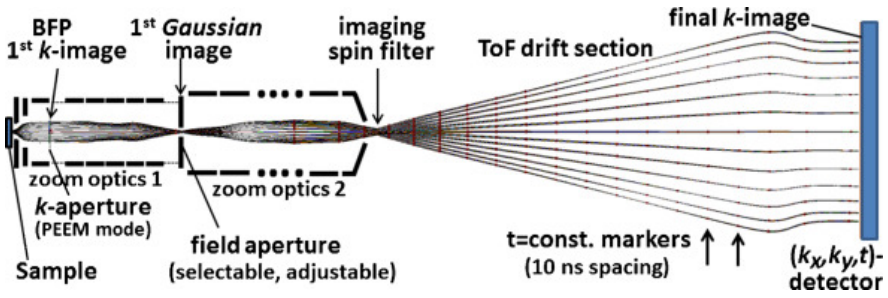

Figure 2.3: Cross section of the ToF momentum microscope. Lines represent ray-tracing simulation of the electron trajectories from the sample (left) to the DLD detector (right). The two zoom optics sections of the microscope are sketched to the left, followed by the low energy ToF drift section to the right. For details see Section 2.6.4. Adapted from Schönhense, Medjanik, and Elmers [35]

The kinetic energies of photoelectrons are resolved through a time-of-flight spectrometer, which consists of a field free drift tube where photoelectrons are separated in energy due to their difference in velocity, and finally hit the detector at different times. This adds the requirement of pulsed photon sources, such as FELs, lasers (e.g. HHGs) or synchrotrons.

2.3.1 Delay Line Detector

At the heart of a time-of-flight momentum microscope lies the DLD[40,41]. This is a 2D detector able to detect single electrons, while simultaneously resolving 3 dimensions: ToF

(converted to energy E) and the two parallel momenta (k_x, k_y). The detection principle is shown in Figure 2.4.

After travelling through the ToF drift tube, each electron is amplified through a Multi-Channel Plate (MCP). The resulting electron shower then crosses a meander-like delay line, wound around a base plate. The signal generated on the wire travels through it, in both directions, towards the ends of the wire. The arrival time at each end is then recorded by an electronic clock. The difference between the travel times in the two directions yields the the position along the detected axis.[40,41] Stacking two meanders rotated with respect to each other by 90° allows 2 dimensional resolution, in the x and y direction. The average of all arrival times detected, is directly related to the electrons drift time[1] through the ToF tube. In order to obtain absolute values of the dimensions resolved, the timings detected need to be related to an external clock synchronized with the photon source.

Spatial resolution, which in turn relates to momentum resolution for a momentum microscope, is limited by the pore size of the MCP as well as by the geometry and design of the wire structure in the meander. It can be as low as 25 µm, when sacrificing sensitivity and time resolution, but values in the range of $80-100$ µm, for active areas of 18 mm to 120 mm in diameter, are the most common compromises. Drift time is digitized with steps of 7 ps, however the resolution is limited by the electronic detection hardware, and lies around 150 ps.[41,42]

Conversion from detector position to momentum is linear in the first approximation, in the case of MM. When looking at high resolutions, however, some care needs to be taken to correct for artifacts and aberrations. Converting from drift time to energy is more complex, as the relation between the time-of-flight and the kinetic energy is non-

[1]To be noted that, in the context of DLDs, *time* refers to the drift time of the ToF spectrometer, and is therefore related to the kinetic energy of the photoemitted electron in analysis. This is particularly confusing when in the field of time-resolved experiments, where with *time* one refers to the delay between excitation and probing pulse (see Section 2.5). Therefore here I will refer to the times in the context of time-of-flight and DLDs as *drift time*, leaving the word *time* for the ultrafast time scale context.

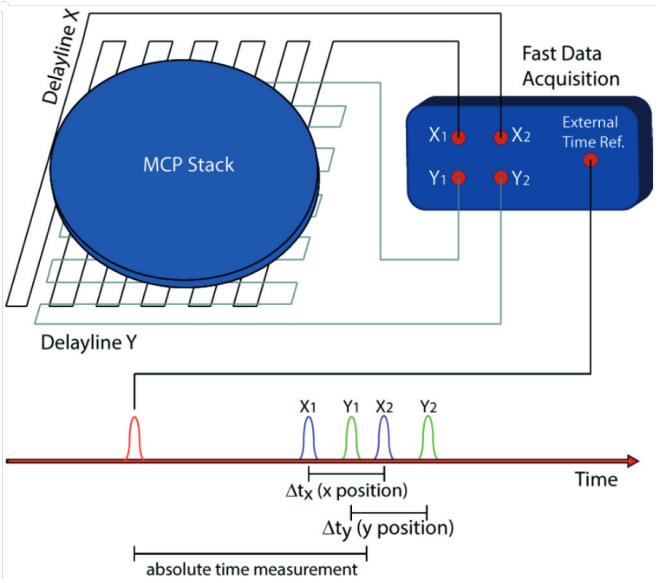

Figure 2.4: Working principle of a single channelDLD. Electrons are multiplied in the MCP plate and generate a pulse in each of the wires of the underlying meanders. From the timing of the pulse recorded at the two ends of the wires, position and absolute measurement time with respect to an external trigger can be determined, therefore resolving position (x,y) and time (t). Source: Surface Concept

linear and various artifacts due to chromatic and geometric aberrations must be taken into account. Also, the non-linearity of such conversion makes the uncertainties and resolutions change across the recorded spectra. In Section 3.6 of this Thesis, methods and examples of how to handle such corrections will be discussed.

An important aspect, which distinguishes DLD detectors from Charge-coupled devices (CCDs) or other integrating methods, is the ability to resolve single (photo)electrons. While being able to reach very high spatial (momentum) contrast and drift time (energy) resolutions, DLDs impose a limit to the detected count rate. Currently, the specifications claim maximum continuous count rates of the order of $8 \cdot 10^6$ Counts/s and burst rates up to 10^8 Counts/s. This limit arises from the 15 ns dead-time the meanders experience after detecting an electron, combined with the Poissonian statistics of distribution of counts across the detector. Developments of multi-channel detectors aim at drastically reducing this problem by stacking up to 128 (or even 256!) meanders together. Such devices will be a game-changer for all experiments using such detection techniques at

brilliant sources, as the limited number of counts detectable "per pulse" is currently the strongest limitation in terms of the data acquisition rate. The other way to increase measurement statistics is to increase the repetition rate of the photon source, a direction in which many FELs facilities are already working towards.

2.4 Space Charge

An issue that plays a central role in MM is posed by the Coulomb repulsion that electrons induce on each other. This effect, commonly known as the Space-Charge (SC) effect, is not unique to momentum microscopes as it plays a major role in all experiments where free-propagating electrons are involved. This process can be described as higher energy photoelectrons being "pushed" by the slower secondary electrons (which were inelastically scattered during the photoemission process), accellerating them and therefore increasing their kinetic energy. The result is a broadening and a shift of the entire recorded photoemission spectra.

These effects can be counteracted by band-pass filtering the fast electrons, as is done by the hemisphere and small entrance slits in conventional ARPES setups. In momentum microscopes this is not usually the case as here every electron emitted from the sample is collected in the microscope column and will therefore contribute to SC.

Reducing the intensity of the photoionization beam helps to reduce SC, which limits the distortion by reducing the number of photoelectrons generated. However, this also strongly affects the data quality, as less photoelectrons will be measured in a given time window. Hence, higher repetition rate systems, which would allow high acquisition rates with low number of photoelectrons per pulse would be greatly beneficial.

The SC problem becomes much more severe in ultrafast experiments as compared to *static* (i.e. *non time-resolved*) experiments. Here a optical pump pulse also generates photoelectrons which contribute to the SC deformations. However, in this case the slow electrons generated by the pump pulse are not so easily filtered from the main photo-

electrons, as the shift and broadening they exert depends on the delay between pump and probe pulse. This makes it difficult to disentangle pump-induced SC effects from dynamics characteristic of the sample under investigation.

In Section 4.5 of this thesis, more details of the SC effect will be discussed, together with the measures we take to limit this effect in trMM.

2.5 Time-Resolved Momentum Microscopy

The Pump-Probe measurement scheme is nowadays a common technique to study ultrafast dynamics of systems following perturbations. This consists of *exciting* (bring out of equilibrium) a system with a short laser pulse and *probing* how its state changes with another short pulse. Studying the changes induced by the excitation as function of delay between these two pulses can reveal ultrafast dynamics on the time scale of femtoseconds.

The most simple variation of this technique is the *all-optical* pump-probe spectroscopy, where a pulsed laser beam is spatially separated in two paths, the "pump" and the "probe". These are then delayed with respect to each other by use of a delay-stage (or in more advanced cases a shaker) and then aligned again on the sample under investigation. Measuring the change in intensity of the reflected beam from the sample, as a function of position of the delay stage, allows to track the changes in the optical properties of the sample before and after excitation by the pump pulse. However, the pump and probe pulses do not need to originate from the same laser source. As a matter of fact they do not need anything in common except for having the same repetition rate and, ideally, a similar time profile.

In a time-resolved photoemission experiment, increasing time resolution limits the energy resolution which can be achieved. This is caused by the Fourier-transform limit:

$$\Delta\tau\Delta E >= 1825 \text{ fs meV} \tag{2.9}$$

which is here expressed in convenient units, assuming a Gaussian time profile with $\Delta\tau$ and energy dispersion ΔE for the "probe" pulse, both taken as Full Width at Half Maximum (FWHM).[17] For example, a 100 fs eXtreme UltraViolet (XUV) pulse (as what is provided at FLASH, see next section), will have, at best, an energy resolution of $>$ 18.25 meV.

2.6 HEXTOF

The HEXTOF end-station, commissioned at the PG2 beamline of the FEL FLASH at DESY, is a time- and momentum-resolved time-of-flight momentum microscope with optional spin sensitivity.[43]

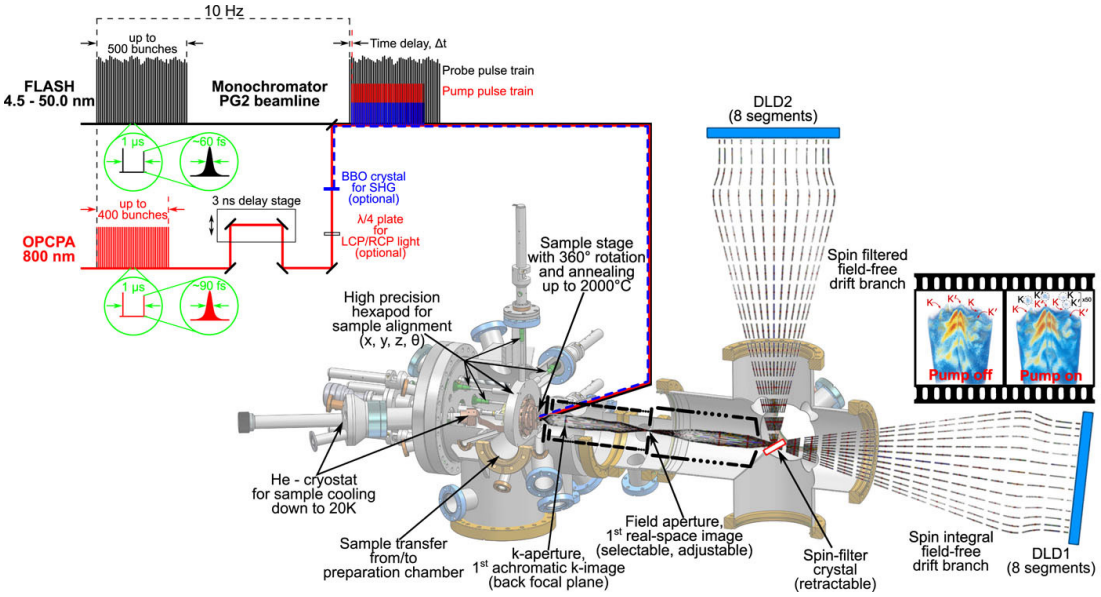

Figure 2.5: Simplified overview of the HEXTOF setup together with the pulse timing structure of FLASH and of the optical excitation laser. From Kutnyakhov et al. [43].

The strength of this machine stands in it's versatility, thanks to the broad tunable spectrum of photons from the XUV to the soft X-ray regime, coupled to a multi-dimensional momentum microscope able to resolve time and spin together with the conventional momentum and energy of the recorded photoelectrons, using a highly efficient detection scheme using DLDs. All data presented in this Thesis, unless otherwise specified, were acquired with this experimental setup.

2.6.1 PG2 @ FLASH

FLASH[44–47] emerged from the TESLA Test Facility, a test project for the development of superconducting accelerator technology.[48] Here the first prototype Vacuum UltraViolet (VUV) FEL was opened to user experiments in 2000. It became FLASH in 2003, and has been upgraded regularly ever since. Its working principle is based on the Self-Amplified Spontaneous Emission (SASE) process, where electrons generated in a Radio-Frequency (RF) gun propagate through a long undulator, where the generated radiation is amplified until saturation. This process generates transversly coherent laser-like radiation in the range of VUV up to tender X-ray.

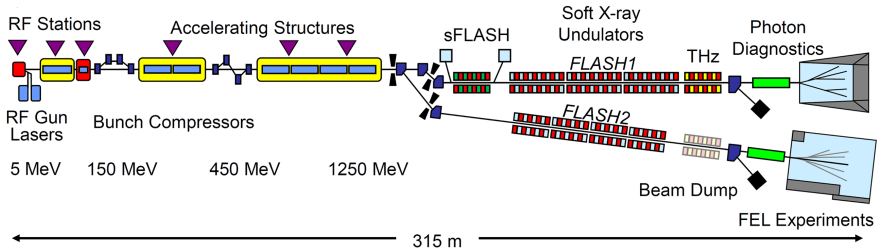

Figure 2.6: Schematic layout of the FLASH facility. The electron beam is generated in the RF gun on the left, and travel through the superconducting accelerating units before being split between the dedicated undulators of FLASH1 and FLASH2 where the X-ray photons are generated and directed to the end-stations. From Schreiber and Faatz [45].

After the linear acceleration units, the electrons are split in two beams, feeding FLASH1 and FLASH2. FLASH1 is composed of six fixed-gap undulator segments which, with electron beam energies between 350 MeV and 1.25 GeV, achieve lasing with energies (wavelengths) between 23 eV (52 nm) and 295 eV (4.2 nm).[45] The 2^{nd}, 3^{rd} and 5^{th} harmonics of the fundamental have also been detected, which push the available energies even higher. FLASH2 is instead equipped with 12 variable gap undulators, providing photons in the range of 13 eV (90 nm) to 309 eV (4.0 nm).[49]

One of the most important aspects of FELs photon sources, together with their high brilliance (10^{28} to 10^{31} photons/s mm^2) is their time structure. FLASH can provide X-ray pulses with pulse duration from 200 fs down to 30 fs (or 10 fs for FLASH2). These pulses are structured in bunches delivered at a rate of 10 Hz. Each bunch (commonly named

pulse train) consists of up to 800 pulses with 1 MHz repetition rate (see top left of Figure 2.5), giving an effective 8000 pulses per second.[50] Typically however not more than 500 pulses are provided (5000 pulses per second), to ensure a homogeneous profile across the bunch, and due to parallel operation of FLASH1 and FLASH2.

A crucial parameter for photoemission experiments is the bandwidth of the photon beam, as this directly affects the energy resolution of the experiment. The PG2 beamline[51,52] offers the possibility of selecting a narrow-band section of the photon beam using a plane grating monochromator (hence the name "PG"). It is equipped with a 200 lines/mm grating for the energy range between 20 and 200 eV and a higher resolution 1200 lines/mm grating for the higher energy range of 100−600 eV.[51] The resolving power $\frac{E}{\Delta E}$ of the high resolution grating goes from 10 000 at 600 eV up to 50 000 below 100 eV. The lower resolution 200 lines/mm grating can achieve resolving powers in the order of 5000 with photon energies between 20 eV and 70 eV.[53] This would correspond, for monochromatized photons of 50 eV, a bandwidth of 10 meV.

Due to the chromatic dispersion induced by gratings, the time profile of the pulses is also stretched. Therefore, when both time and energy resolutions are of importance, such as in the case of time resolved photoemission experiments, low groove density gratings and opportune focusing constants can be set in order to obtain reasonable compromise.[52] Typically, at HEXTOF photon energy bandwidth and time resolutions of the order of 100 meV and 100 fs respectively can be reached.

2.6.2 Pump Laser

Pump-probe experiments require, together with the probe pulses also excitation (pump) pulses which bring the system out of equilibrium. The FLASH1 hall is equipped with two optical lasers synchronized to the FEL pulses, which are fed to the different beamlines for this purpose. The beam path of both FEL and optical are shown in Figure 2.7.

The first laser system is a high pulse energy laser, with up to 20 mJ pulses, 50 fs (FWHM) long, at a repetition rate of 10 Hz, synchronized to the low repetition rate of

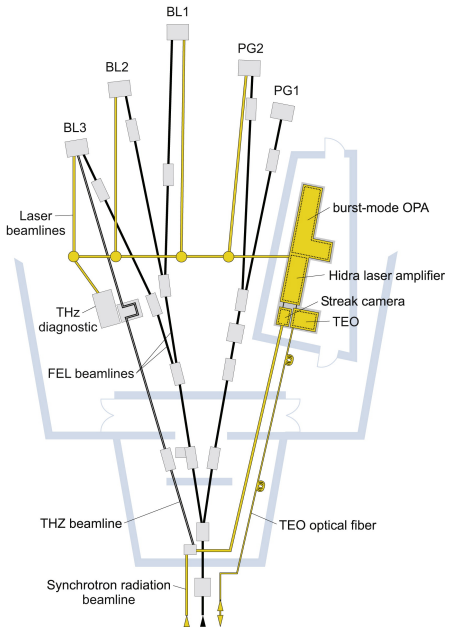

Figure 2.7: FEL and optical laser path to the different beamlines of the FLASH1 experimental hall. From Redlin et al. [54]

the FEL pulse train. The second, provides 60 µJ pulses of < 120 fs FWHM, synchronized with the complex burst pulse structure with MHz repetition rate[54]. Both systems can be directed to any of the end stations in the FLASH1 hall. For the photoemission experiments with HEXTOF, the choice falls on the latter, given the requirement of high repetition rate and the limits on maximum fluence imposed by SC effects.

This laser system is no longer available, but was still described here since it is the system which was used for the experiments presented in this Thesis. It has now been substituted by a new laser system, named PIGLET.[55]

2.6.3 Timing Synchronization

Time resolution in pump-probe experiments is determined by three factors: the pulse duration of pump and probe pulses, as well as the jitter of the timing difference between the two. Laser based pump-probe setups have no jitter, as both pump and probe are split from the same pulse. However, in experiments when pump and probe pulses are generated by two different systems, synchronization between the sources plays a major

role and can introduce jitter.

Furthermore, in a SASE FEL, the temporal compression of short pulses depends on the energy and momentum distribution of the electrons in the bunch.[2] This results in strong shot-to-shot fluctuation of pulse duration and intensity of the FEL pulses, as well as jitter. Therefore, proper synchronization between FEL pulses and optical laser pulses is critical to perform ultrafast experiments with FELs. At FLASH, an all-optical synchronization system, based on a master laser oscillator is used as a master clock for all critical elements throughout the FEL facility, as well as for the optical laser, leading to an rms jitter of 30 fs for X-ray pulses of 90 fs.[56]

The small jitter on the FEL pulse timings, as well as drifts in the laser amplifier can however still be present. To enable post-processing correction of these deviations, two methods are being used in parallel at FLASH: the Beam Arrival Monitor (BAM) and the Streak Camera (SCam).[54]

The BAM measures the difference between the arrival time of a relativistic electron bunch and the master laser clock. The bipolar transient signal generated by the electron bunch in an antenna is used to drive an electro-optical modulator, which in turn modulates the intensity of the master clock laser pulse, measured by a balanced photodiode.[56] This gives a high resolution (5 fs) readout of the jitter between optical the laser and the electron pulse, but is limited to a small timing window of 4 ps.[57] Although an RF signal is used to keep the BAM in the right timing window, for slow and larger drifts, the SCam is required.

The SCam[3] monitors the relative timing between the optical laser and the dipole radiation generated by the electron bunch, when being separated from the X-ray radiation after the undulators.[57] This is however measured as an average over 2 seconds and cannot therefore be used as a shot-to-shot monitor, but only as a slow drift correction.

[2]These are the electrons from the RF gun which generate the X-ray radiation in the FEL, not to be confused with the electrons extracted from a sample in the photoemission process.

[3]The SCam is no longer available with the new laser system PIGLET.

Details of how these two measured quantities can be used to correct jitter and in turn increase the pump-probe time resolution will be discussed in Section 4.3.

2.6.4 The Microscope

The microscope installed in HEXTOF is a time-of-flight momentum microscope, as described in Section 2.3. It is tuned for maximum momentum resolution as well as large zoom range for the momentum image, allowing a FOV from 1 Å up and beyond 6 $Å^{-1}$ in diameter. The first momentum image is projected in the back-focal plane of the objective lens, then projected and magnified by two groups of lenses to the drift-tube. The latter is a field-free, low-energy ToF tube, 800 mm long, where the typical drift energy is kept between 10 and 30 eV.

A series of adjustable field apertures placed in the Gauss image (real-space image between the two momentum imaging points) allow to select a Region of Interest (ROI) on the sample from which electrons will be transmitted to the ToF spectrometer. Different evaluations of the achieved energy resolutions range between 80 meV FWHM measured on a Ag sample, to $130 - 150$ meV as measured on W and FeRh samples. The same electron optics have shown energy resolutions below 15 meV in lab experiments with photon energies of 6 eV. The lower resolution achieved at FLASH can be attributed to FEL bandwidth, jitter and SC related effects.

The sample is mounted on a hexapod manipulator which allows full control of 6-degrees-of-freedom control of sample position and orientation in front of the microscope. Furthermore, cooling can be done using a liquid He cryostat, while electron bombardment can be used for high temperature flashing. More details on this setup and its performance are presented in the article by Kutnyakhov et al. [43].

Concluding remarks

The basic principles of photoemission spectroscopy were presented in the first sections of this chapter, followed by more details about the specific technique used in the work

presented in this Thesis: trMM.

An overview of the specifications of HEXTOF, the end-station installed at FLASH, with which most of the data presented in this work was obtained, covers the "hardware" aspect of these experiments. The next chapters will focus on the data stream produced by such experimental setups, and the "software" aspects which have been developed to exploit the capabilities of these complex experiments.

CHAPTER 3

Multidimensional Data Processing

The increase of data size and complexity is one of the greatest challenges of our society today, which calls for a radical change in the approach to data. This is the case also in experimental solid state physics, in particular for the field of photoemission spectroscopy.

MM, simultaneously measuring a 3D parameter space (position coordinates on the detector and time of flight), with its high dimensionality variants, such as trMM, requires a completely new approach to data acquisition. Recording data as 2D images is easy, and even for 3D data, stacks of images are not hard to handle. However, increasing the number of dimensions further, and recording stacks of stacks of images, becomes quickly unmanageable.

Moreover, the acquisition rate available at 3rd and 4th generation light sources increases the data throughput enormously. However, all these novel developments in data volume and complexity lead to a much greater information depth of recorded data, enabling experiments not possible otherwise. Such possibilities are going to increase even further, with the development of AI and ML based analytical methods. These require data to be well labeled, with metadata describing all available information about

the sample under investigation, but also of the experimental apparatus and even each post-processing step. Only a fully documented experimental dataset can then be combined or compared to other experiments or simulations, to shed light on new intriguing phenomena.

In this chapter, I will describe the work I did, together with an ever-growing community, towards tackling such problems. I will describe the data structures we have developed to record MPES data, as well as methods to exploit them to increase the signal-to-noise and resolution. I will go through the different post-processing methods and the reasons behind them, building what would be a complete workflow for a time-, energy-, momentum-resolved photoemission experiment. This will be done on an example, based on the data obtained at FLASH with the HEXTOF machine,[43] using the software tools we developed to this end, publicly available in the `hextof-processor` repository.[58]

3.1 Data Processing Workflow

A well defined workflow to process the data from raw experimental data to post-processed physically interpretable data, is key to ensure reproducibility. Every step taken needs to be documented, and any parameter used in this process needs to be saved together with the data itself. This is ensured, in `hextof-processor`, the python package we developed to process trMM measured with HEXTOF, by defining specific methods (Python functions) for each calibration/correction/conversion step. The name of these functions is saved, together with the parameters passed to them, in metadata dictionary which follows the data throughout the entire workflow. In this way, another user which would only get hold of the final volumetric data, is still able to reconstruct the entire history of the data.

The work we published in Xian et al. [59] presents a first overview of such a workflow, based on WSe_2 data measured with HEXTOF, which follows these principles and shows

how a fully described workflow can be used. This work resonated strongly in the solid state community, particularly, but not limited to, the photoemission community, which was a signal that this is indeed the path researchers need to and are willing to take for the future of scientific research.

3.2 Single Event Data Structure

As previously introduced, contrary to the use of CCD cameras, the usage of delay-line-detector (DLD) with time-of-flight (ToF) spectrometers allows each detected photoelectron to be resolved. This opens the door to a whole new approach in terms of possibilities in data post-processing by allowing each event to be corrected for independently by systematic errors or measurable jitters, thus greatly increasing the effective resolution of the measured quantities, but that also increases the challenges of handling the generated data.

The traditional approach to acquiring data in multidimensional spectroscopy is to define a grid of points in the detectors parameter space, e.g. along energy and the two component of parallel momentum and integrate over acquisition time the number of detected photoelectrons in each of these points. This approach has the advantage of having data "ready-to-plot" out of the experiment, and generates relatively small sized files on disk, as long as the number of dimensions does not grow above 3 or 4. In fact, the scaling problem induced by increasing the number of dimensions is the first motivation for the development of SEDs.

The SED is a table where each detected event is stored as a row, together with all the relevant parameters the experimental setup records as columns. Table 3.2 shows an example of a SED with a few selected parameters. Such a structure scales linearly with the number of recorded parameters, ($\propto n$) as opposed to storing the data as n-dimensional arrays, where the data size scales with the number power of the number of dimensions D ($\propto n^D$). However, resolving each event scales the size of the SED

linearly with the acquisition rate, which can lead to very large data-sets in experiments with a large number of detected events, as for example in high repetition rate or high brilliance sources. When looking at data size, SED are therefore most indicated for those experiments which can resolve a large parameter space, as the exponential size growth out-weights the linear increase from the number of recorded events.

ElectronID	PulseID	TrainID	posX	posY	ToF	enc
1	0	1	561	752	26,158	-178.21
2	1	1	458	825	31,549	-178.21
...	...	...	...	...	...	...
5,260	389	95	901	650	33,569	-181.69
5,261	391	95	565	846	28,542	-181.69
...	...	...	...	...	...	...
55,524,136	210	5261	859	589	37,289	-177.54

Table 3.1: An example of what a Single Event Data frame (SED) looks like, with fictional data. The three-level indexing, with electronID incrementing at each photoelectron added to the table and PulseID and TrainID indicating which pulse of which pulse train generated the photoelectron. The other columns, here showing the DLD channels posX, posY and ToF (position x and y and time-of-flight) and the encoder value, related to the pump-probe time delay.

This is the case in the HEXTOF experiment at FLASH, the free-electron laser facility at DESY in Hamburg.[44] The FLASH facility records hundreds of parameters regarding the state of the FEL, from the electron gun source all the way to the experimental chambers. These values can be "pulse resolved" when updated per each X-ray photon pulse, at up to 5 kHz, or in many cases "bunch-resolved", with bunches being the pattern of up to 500 pulses at 1 MHz, repeated at rate of 10 Hz. Many of these parameters do not directly influence the data recorded in the momentum microscopy experiment, but serve as monitors and controls for the steady operation of the free electron laser. Among these are ambient temperature and humidity or pressures along the beamline as well as parameters characterizing the current state of the FEL beam. Others however are strongly correlated to the dimensions recorded in the experiment and can be used to correct for jitters and drifts, such as timing jitter between FEL pulses and optical laser, or FEL and optical intensity fluctuations. Such a large parameter space, with more than

20 parameters impacting the measured data, is the perfect case for using SEDs.

Storing data in the SED format is an intermediate step between measurement and evaluation, as this cannot be directly visualized with the standard tools most often used in the field. In order to produce a plot, such as an EDC, Momentum Distribution Curve (MDC) or extract a multidimensional array, a histogram of the data-frame needs to be computed. This process can be computationally demanding, therefore making it necessary to use advanced data processing tools and parallelization methods.

3.3 Software

Handling the data produced by the HEXTOF end-station, from converting the raw data provided by the facility into the SED, to visualizing the results, requires an ad-hoc developed software. To this end, in collaboration with other users involved in the project, I have developed a software package: `hextof-processor`.[58] This project, started by Dr. Yves Acremann, is written entirely in Python. Its main scope is that of parsing the raw data structure provided by FLASH through the Data Acquisition System (DAQ),[60] and generate from it the clean table of detected photoelectrons.

All the methods described in this chapter, are available in the `hextof-processor` package in GitHub, and are under continuous development as new experiments come online with different requirements and inspire new optimization steps for existing routines. This flexibility is granted by the community driven development of this software package, which is performed in close collaboration with the users of the HEXTOF machine during and after each beam-time, always adding new features while retaining retro-compatibility for usage with data obtained in previous experiments.

Such an approach is only possible in the context of collaborative open-source projects, where the whole community can profit from the work of each researcher and grow a flexible set of tools which can be widely used and understood. This is particularly important nowadays, when the complexity of data analysis tools is growing at an ever

increasing rate, and it is no longer feasible for each researcher to develop a full data processing pipeline following all the latest standards. Commercial software can still meet most demands in terms of analysing and understanding the measured data, but this experiment, and the SED data structure are an excellent example of how an intermediate step between measurement machines and analysis is growing in complexity and requires increasing attention and dedication. Furthermore, such frameworks ensure additional features are constantly checked and tested, modified and/or fixed by the large community.

3.4 Workflow structure

The SED are not the original data structure in which data is stored at FLASH, nor are they the final shape for data to be analysed, shared or stored. They are instead an intermediate step of a workflow which brings data from the experiment, to a *readable* format, enabling post-processing methods not possible otherwise.

The workflow used in `hextof-processor` to take full advantage of this, is composed of three main components:

1. Generation of a SED clean table from the data structure provided by the experiment (FLASH in this case).

2. Physical axis calibration and artifact correction.

3. Binning: computing of the n-dimensional histogram along the dimensions of interest for analysis/visualization/storage.

A diagram of this workflow is shown in Figure 3.1,

The first step, data conversion, is closely tight to the specific experimental setup, as it needs to be tailored to the data format in produces.

The second step includes the application of many diverse elements. First of all, methods to convert measured quantities to their physically relevant counterparts, i.e. time-of-flight to energy, or detector position to momentum. Further, it contains artifact corrections such as aberrations induced by electron optics, or small energy shifts induced by SC effects. Most of these methods are general and could be applied to SEDs generated from other momentum microscopes than HEXTOF. More importantly, none of the procedures in this step are strictly *necessary* to connect data conversion (step 1) to output (step 3). This means that during beam-times, where quick data visualization takes priority over calibrated and artifact-free data, post-processing can be reduced to a minimum if not entirely skipped.

The final step is the production of volumetric data, as n-dimensional arrays, as this is the most accessible format for data to be analysed, visualized or simply stored and shared with other researches.

In the following paragraphs, the first and last steps will be discussed, while calibrations and artifact corrections, given their complexity, will get their own sections later in this chapter.

3.5 Reading the Data

Data acquired during experiments at FLASH is available to users through the Data Acquisition System, which collects all data necessary to run and monitor the entire FEL together with data provided by the specific experimental end-stations. The data provided to the end users of an experiment is composed of a subset of these parameters, containing only the information the users deem relevant for data analysis. These data are collected in a series of HDF5[1] files, composed by data-sets for each parameter.

Each data-set is a 1D, 2D or 3D array, containing values recorded form one or more

[1]HDF5 is a hierarchical data structure which allows storing *data-sets* in a familiar folder-like structure. It also allows for chunking and compression, making this a widely used data format in the scientific community.[61]

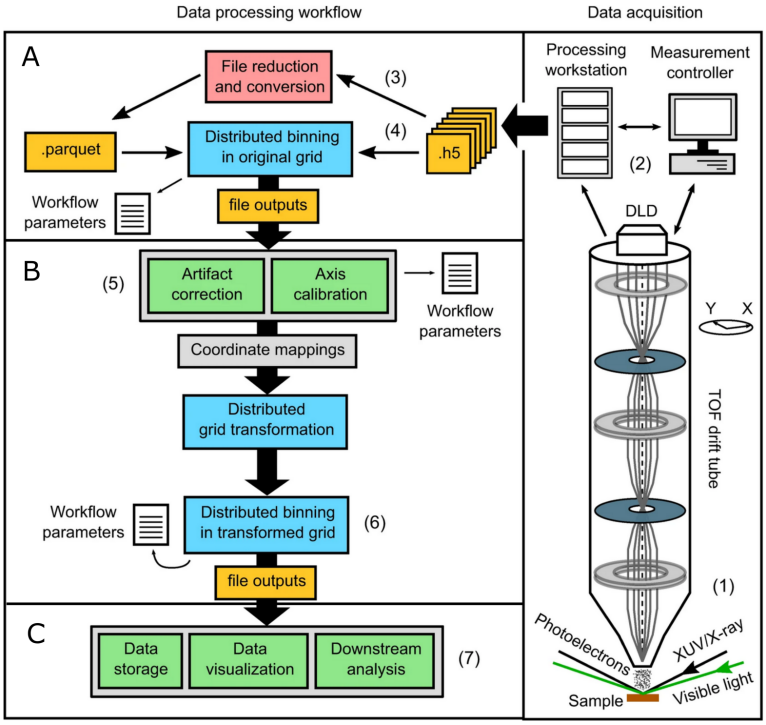

Figure 3.1: Diagram of the workflow processing, illustrating the steps taken from raw experimental data obtained by the HEXTOF Momentum Microscopy to publication quality datasets. The vertical sections, A,B and C correspond to the three workflow blocks described in the text. The raw data processed into Single Event Data frame (SED) by a workstation is stored as HDF5 (or parquet, see text). Artifact corrections and axis calibration parameters are obtained on coarsly binned datasets, or from previous datasets measured in the same conditions. These are then used to generate the calibrated dimensions in the datasets which are finally stored for fast access. Finally, these data are binned in the regions of interest with the desired resolution, and saved for publication, visualization or downstream analysis. Adapted from Xian et al. [59].

instruments. The first dimension reports values at 10 Hz, each element corresponding to a bunch train. Parameters which are FEL-pulse resolved are represented in a 2D array (table), with each row being a bunch train and each column a pulse of the train structure.

The detection scheme of the DLD allows for multi-hit detection, which implies that, for each FEL pulse, more than one event can be recorded. Therefore, the data-sets corresponding to DLD data are structured differently from the other parameters. These are also 2D arrays for each DLD quantity (time-of-flight, detector position etc..) with

each row corresponding to a pulse train. The second dimensions, the columns are filled for each event recorded with the "pulse-ID" of the FEL pulse which generated it.

This structure requires a computationally expensive step to be converted in a simple electron-ordered table, as all pulse resolved parameters need to be related to the electron-ordered structure imposed by the DLD channels. As this conversion step is time consuming, the SED is usually stored in the convenient Apache Parquet data format[2] which grants fast and highly parallel access for further processing or binning.

Since late 2020, a new data structure is in use at FLASH, which has simplified this structure conversion step. All the different sources of the parameters available in the DAQ system come from machines which report values at different rates. Some are FEL-pulse resolved, but many are updated only every second or even slower. In the old system, an algorithm was forward-filling[3] such low frequency values to have values for each pulse train. This step induced a 10 to 15 minutes delay in the arrival of the data for visualization and evaluation.

The new structure skips the forward-filling step, reporting for each parameter an indexed data-set, where the row index gives the "trainID", the pulse train number when the value was recorded. This allows the data to be available much faster, but leaves computation of forward-filling to the users. To convert this structure, we assign indexes for the "pulseID", the number of the FEL pulse inside the pulse train and for the "electronID", an increasing number for each electron generated in the same pulseID. Merging these columns as multi-index tables allows to directly create the SED. These tables are then stored as an apache parquet file for each HDF5 file provided by the DAQ, and later forward-filled.

Transformation from these data-sets to the SED requires less than one minute, and can

[2]The Apache Parquet data format is flexible columnar storage format, which allows for easy parallelization with fast access, greatly increasing performance when compared to HDF5.

[3]forward-filling is the operation of filling a sparse filled column of a table by repeating a value until a new one is found.

be done in parallel for multiple files (e.g. when reading a run which has been running for a long time, and has generated many files). The conversion time is therefore faster than that required for the old system, while also removing the 10-15 minutes delay for data availability, bringing the on-site data evaluation closer to real-time.

3.6 Physical Axes Calibration

In experiments, the measured quantity is rarely directly the physical observable one is interested in studying, as the time-of-flight is measured instead of the electron's kinetic energy. Conversion and calibrations are therefore often required. In photoemission spectroscopy, the main observables are two: the electrons energy E and momentum $\vec{k}$. The DLD however measures "when" (time-of-flight) and "where" (x and y coordinates) an electron was detected, which are directly related to the electrons kinetic energy and to the two components of parallel momentum, respectively. With sufficiently high photon energies, the large FOV in momentum space obtained allows to exploit the change of perpendicular momentum across the detected area, reconstructing part or even a full Brillouin Zone along k_z.

In multidimensional momentum microscopy, more observables are studied, such as the electrons spin in spin-resolved momentum microscopy, or, as in our case, the time delay between the pump and the probe pulses in trMM. In HEXTOF, the pump-probe delay is controlled by a delay stage, equipped with an encoder which measures its precise position.

Recording data using the SED structure allows the tracking of different monitoring parameters and use them to calculate the value of an observable for each detected event. This is as simple as defining a new column in the data-frame, where the values are assigned based on the value of other columns or other external parameters. In `hextof-processor`, each of the calibrations described in this section has a class methods (functions) which, when provided with all the external parameters, automatically takes

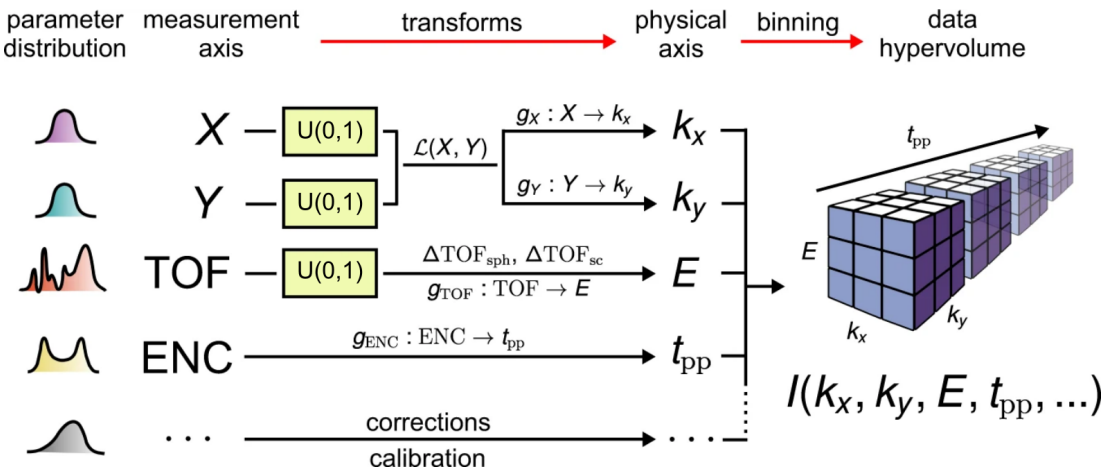

Figure 3.2: Physical axes calibration pipeline. The characteristic 1D distributions of the measured X, Y, TOF, ENC and an arbitrary axis are shown on the left. $U(0,1)$ represents uniformly distributed random noise added to suppress digitization artifacts (see section4.4.6). The transforms (g's) are calibration functions that convert the values in the measurement axes to the physical ones. The transform $L(X,Y)$ corrects the symmetry distortion, while the spherical timing aberration and space charge are compensated for by ΔTOF_{sph} and ΔTOF_{sc}, respectively. Binning of the corrected single-event data over the calibrated physical axes yields a multidimensional hypervolume (right picture) of photoemission intensity data along with the physical axes values. From Xian et al. [59]

all the available parameters (columns) from the data-frame and creates a new column with the calibrated values. All the parameters provided are then stored as metadata next to the data itself, allowing to easily trace back how each axis was obtained and ensure reproducibility. The path from raw data colums to calibrated and corrected datasets is depicted in Figure 3.2.

In sections 4.1, 4.2 and 4.3 I will walk through the methods used to convert between these measured quantities and their corresponding physical observable, as well as to reduce noise and jitter by using the additional parameters recorded in the SED.

3.7 Binning

As much as single event data-frames are optimal for handling data in a large parameter space, the data needs to be transformed to n-dimensional volumetric arrays in order to be further analyzed. The photoemission experiment is the measurement of a discrete

quantity, the number of electrons detected with a given set of parameters: momentum, energy, time delay etc.. Volumetric data can therefore be computed from the list of all events, the SED, by counting how many of these electrons fit in each voxel of an n-dimensional array. This process is called *binning* and is nothing else than computing a histogram of the number of events on a defined n-dimensional array.

Filling the n-dimensional array can be easily parallelized by computing the histogram on subsets of the SED, and later summing them up, making the process significantly faster. This comes at the cost of increased memory usage, as each subset requires a copy of the final n-dimensional array in memory, where to store the intermediate histogram.

In `hextof-processor`, the SED data-frames are handled using the `dask`[62] package, a package built to use common analytical tools for arrays (based on `numpy`[63] arrays) or tabular data (based on `pandas`[64] in a highly parallelizable fashion. In a nutshell, `dask` performs computations on the array/data-frame by mapping the workflow on subsets of the data-set (called *partitions*).

The final computation is then made using only the necessary partitions and distributing computation across multiple threads or processes on the local machine (computer) or in the cloud (cluster, supercomputer). This allows to seamlessly parallelize large tasks such as the binning required for generating the n-dimensional arrays. This, however, also adds overheads which scale with the number of partitions involved and computation steps, *tasks*, which will be performed on them. Using an optimal size for the partitions, based on the number of cores and memory available on the system, can drastically impact performance, since `dask` adds overheads to the computation which increase with the number of operations, that is proportional to the number of partitions.

As an example, processing SED on the *Maxwell Cluster* from DESY, with 96 cores and 350 GB of RAM memory on a single node, shows best performance with partitions from 50 MB to 1 GB each.

Another important aspect to improve performance is in the choice of the data-type of the different columns stored in the SED. It is often assumed that scientific data needs to be stored with the maximum precision, in this case as floating point values with 64 bit precision. However, most instruments do not reach near to such precision, and can be represented in 32 or even 16 bits with no loss of information. Values are often recorded as integers, for example timestamps, and these should also be stored with the lowest precision which allows their full representation. For example, the *pulseID*, the number of the FEL pulse in a pulse train cannot be more than 800, the number of pulses in a train. Therefore, a 16 bit unsigned integer, which can represent values up to 65 535, is more than sufficient. Such details can easily reduce both storage size and evaluation time by over an order of magnitude.

Furthermore, storing on disk a parquet file of the calibrated and corrected data-set on which to perform the binning also strongly reduces the overhead, induced by the many intermediate steps of the workflow.

To give a feeling of the importance of these optimizations, learning and implementing them over the last years has brought the time required to process and *bin* one hour of data acquisition at FLASH from over 90 minutes (no parallelization, direct binning) down to just a few seconds (using highly optimized parquet files, which require about a minute to create).

3.8 Data storage and publication

The advancement in data complexity and information depth calls for new approaches for data treatment and analysis as well as new means for storage, re-usage and sharing. The F.A.I.R. principles are a series of principles for how modern scientific data should be handled, introduced by Mark D. Wilkinson *et al.* in *The F.A.I.R. Guiding Principles for scientific data management and stewardship*[11]. The acronym stands for **F**indable, **A**ccessible, **I**nteroperable and **R**eusable. The goal of these principles is to make scien-

tific data understandable by machines with no further human intervention. These are requisites for the novel AI and ML tools which are nowadays growing at incredible rates.

The main requirement for data to be *AI ready* is to couple data with as much relevant information as possible on how it was generated or treated, and to gather this in a commonly agreed format which can be read and understood by others without further information. In other words, data should be always accompanied by a set of metadata which describe all (or as close to all as possible) the information required to reproduce the data. The list of elements which fit in an experiment's metadata can be very long. It is easy to imagine how many possible parameters can influence the outcome of a measurement: all the settings of the experimental apparatus, the sample and its history (production method, surface treatment processes, age, temperature, etc...) as well as who was involved in the measurement, acquisition and post-processing software used, their version and all the parameters involved...

As the list goes on, an immediate issue arises: how can the entire community find the right terms with which to describe all these metadata in a unambiguous manner? It requires agreement on the definitions (ontology) across a community of researchers who are dealing with similar experiments.

In the field of MPES a collaboration, Open Community of Multidimensional Photoemission Spectroscopy (openCOMPES)[65] is being set up, aimed at defining a standard set of metadata descriptors as well as a format to store and access data and metadata. The proposed structure and rules are those defined by the *NeXus*[66] project. This consists of generating HDF5 files with a fixed structure of groups and data-sets, as well as defined names for each parameter (i.e. the temperature of the sample should always be labeled as *sample temperature* and not other variation of it). Should such a file structure be employed by a sufficiently large number of participants, this could set a standard for future photoemission experiments which would greatly facilitate development of next generation AI based analytical tools, which might be key to revealing and understanding

new physics.

Concluding remarks

This chapter introduced the importance of advanced processing methods for experimental science, in the times when the data size and complexity are growing at an incredible rate.

The introduction of the Single Event Data frame (SED) as a data structure to handle electron-resolved data streams produced by DLD detectors allowed to define a new approach to artifact correction and axes calibration. We defined a workflow to process the raw data stream into fully described n-dimensional data-sets ready for analysis, storage or publication.

In the next chapter we will discuss the different steps that compose such a workflow, from axes calibration to artifact corrections and methods to enhance signal-to-noise ratio (SNR).

CHAPTER 4

Calibrations and Corrections

This chapter describes the technical "behind the scenes" of the data processing workflow developed for time-resolved momentum microscopy. The aim of this chapter is to give an overview to the reader who is interested in handling such data, and offer all the experience and insights I have gained in my work on momentum microscopy.

The first sections will describe the calibrations of the main physical axis of interest: the kinetic energy, momentum and the pump-probe time delay. In between, the most relevant artifact correction methods will be described, describing both the artefact's origin as well as how it can be treated numerically. The post-processing Section 4.4 lists some useful methods to correct for numerical artifacts as well as methods to obtain important parameters from the data.

Finally, a more detailed section is dedicated to the treatment of Space-Charge (SC) effects. After describing a simple phenomenological model to understand the origin of these effects, some numerical methods to model them will be presented. This section concludes with an outlook to machine optimizations for the next generation of momentum microscopes, which aim to suppress a large part of SC effects, allowing to perform

experiments with greatly increased optical pumping fluences.

Most of the functions and methods here described are written in python code in the `hextof-processor` package in GitHub.

4.1 The Energy Axis

As in any "spectroscopic" experiment, the main axis of interest is the *energy* axis. In photoemission, this axis can represent two quantities: the *kinetic energy* of the photoelectrons after being extracted from the crystal, or the *binding energy* the original electron had, inside the crystal before being photoemitted. These quantities are closely related to each other, but in different parts of the photoemission community, one or the other is most commonly used.

In a ToF momentum microscope such as HEXTOF the energy axis is resolved by means of a ToF spectrometer. This is a drift tube in which electrons travel free of any electromagnetic field before hitting the detector.

4.1.1 Kinetic Energy

The kinetic energy of an electron can be obtained by measuring the time it takes to travel through the drift tube, using the relation

$$E_k = \frac{1}{2} m_e v^2 = \frac{1}{2} m_e \left(\frac{l}{t} \right)^2 \tag{4.1}$$

where l is the length of the path the electron takes from the sample to the detector and t is the time it took. This time can be measured by referencing the arrival time recorded by the DLD to the master clock, synchronized with the photon source which generated the photoelectron. The non-linear relation between travelling time and energy leads also to an energy dependent energy (and momentum) resolution.[38]

The path length, however, is a more complex problem as electrons with different initial energy and momenta (or spatial position if working in microscope mode) might have significantly different travelling paths. Depending on the lens setup, a constant value

of l can still be used for all electrons in a narrower energy range around the focus. A more sophisticated approach could be that of using ray-tracing software to simulate the electron paths and travel times, and determine the path length as a function of kinetic energy and detector position. Nevertheless this requires an exact modelling of the electron optics used, which is not always available, especially when changes in settings are done manually between experimental runs, and no automatic logging is in place.

Secondly, equation 4.1 holds for free electrons which do not see any additional potential exiting the sample. In a momentum microscope , a voltage is applied between sample and microscope, which directs the electrons into the mouth of the microscope. Also, any voltage applied in the ToF tube accelerates the electrons further and that needs to be taken into account. The final kinetic energy an electron will have, when drifting along the field free tube, can therefore be obtained as

$$E_k = \frac{1}{2} m_e \left(\frac{l}{t}\right)^2 - V_{sample} + V_{ToF} \tag{4.2}$$

with V_{sample} and V_{ToF} being the sample bias voltage and the ToF voltage respectively.

4.1.2 Binding Energy

Given that energy is conserved in the photoemission process, the initial *binding energy* E_b of an electron can be obtained as:

$$E_k = h\nu - \Phi - E_b. \tag{4.3}$$

Here $h\nu$ is the photon energy and Φ is the work function of the material, i.e. the energy an electron at the Fermi edge needs to be extracted to the vacuum. Combining equations 4.3 and 4.2, we obtain the relation between the time-of-flight and the binding energy as

$$E_b = h\nu - \frac{1}{2}m_e\left(\frac{l}{t-t_0}\right)^2 - \Phi + V_{sample} - V_{ToF} \tag{4.4}$$

where t_0 is the time at which the electron is extracted from the sample, referenced to the same clock to which the DLD is referenced. This t_0 can be determined by recording the so called *photon peak*, a sharp peak in the energy spectra generated by photons reflected from the sample and illuminating the detector. Given that the speed of any photoelectron is far from the speed of light, the time of arrival of the photon peak can be assumed, in the time scale of the electron drift time, to be simultaneous with the time of the photoemission process.

4.1.3 ToF binning vs Energy binning

The importance of applying non-linear conversion to data on the SED level, and binning in the correct energy axis is evident when observing Figure 4.1. Here, two EDCs from the same dataset are plotted. The blue curve shows the data binned in time of flight, with the conversion to binding energy applied to the ToF axis values, while the orange curve, shows the same data, binned directly on the energy axis. In both cases, the calibration function, and all associated parameters are identical. The difference between these curves, with the artificial increase in counts with decreasing binding energy, is due to the change of bin size.

The non-linear transformation changes the effective "size" of the bins on the x axis for the energy binning, meaning that the time-of-flight window which corresponds to 100 meV at $E_b = 0$ is larger at lower binding energies. Therefore, binning linear in ToF, i.e. counting how many events were recorded per ToF interval, will return smaller values at lower binding energy as compared to binning linear in energy. This effect can cause errors in the analysis, as it will strongly affect the spectral shapes of, for example, core levels.

One solution would be to normalize each point of the curve binned in ToF to the size of the corresponding energy window. Directly binning in the calibrated physical quantity

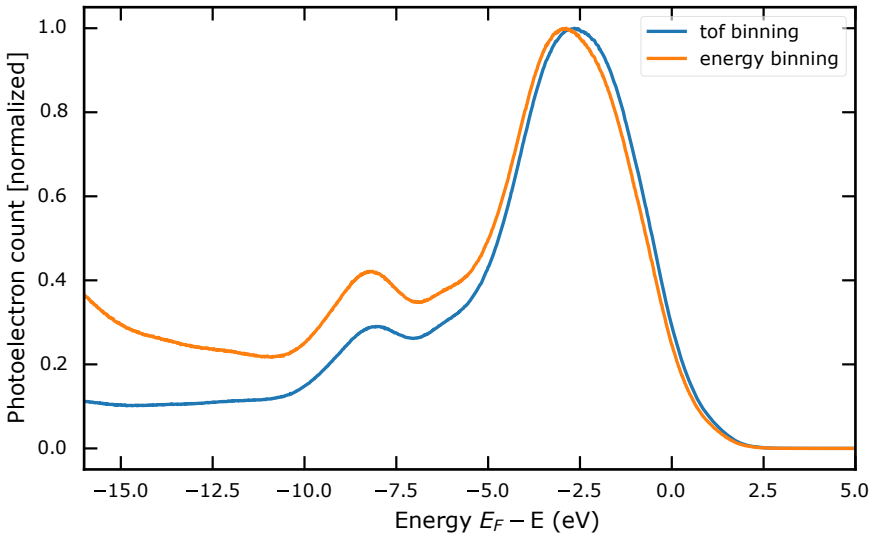

Figure 4.1: La_2CuO_4 EDC obtained by binning in time-of-flight and converting to energy compared to binning in energy, computing the calibration for each event. The discrepancy between the apparent intensity at lower binding energy arises from the relative change in bin size due to the non-linear transformation.

(i.e. energy) however is still to be preferred, as it reduces the number of calibration steps (no normalization required) and can be properly combined with other calibration methods.

4.1.4 The Energy Calibration

All quantities in equation 4.4, with exception of the work function Φ, are directly recorded and available in the raw data provided by glsflash, and in turn in the SED. For example, the photon energy selected by the monochromator is one of the available parameters, as are the voltages applied to the sample and in the ToF tube.

The `calibrateEnergy` available in `hextof-processor`, which takes care of generating the calibrated energy column in the SED, when run with the default arguments, will use the available data from the SED to evaluate photon energy and electrostatic potentials in the microscope. However, if needed, these values can also be passed manually.

The same logic applies to all calibration functions used in `hextof-processor`, where default values will look for the measured data but can be manually overwritten. Should

they be overwritten, the arguments passed to the function are saved in a dictionary to ensure this information is retained in the final metadata which will be stored together with the data in its final shape.

Once the conversion between ToF and energy are computed, further corrections, based on evaluation of the EDCs, can be applied. Among such corrections is the shift in kinetic energy caused by SC effect (SC) (see sections 2.4 and 4.5). As previously described, the main effect of the space-charge is to rigidly shift the energy spectra towards higher kinetic energies, with a 2D Lorentzian profile across the detector, centered around the optical axis of the microscope.[67] The details of this the space-charge effect, its origin and what steps can be taken to compensate it, will be treated in Section 4.5. As here the focus is on post-processing methods, an *a-posteriori* method to correct kinetic energy shifts strongly correlated to one or more parameters in the SED will be described.

4.1.5 Energy Shift Corrections

Independent of what the physical origin is, rigid shifts of the EDC across the detector, as induced by aberrations from the electron lenses or by weak space-charge effects (see Section 4.5) can be corrected by modelling one (or more) dispersion-less features of which the binding energy is known.

This method will be explained here based on the example of La_2CuO_4 data I obtained at FLASH, results from which are presented in Chapter 6. In this data, a clear 2D Lorentzian deformation of the energy isosurfaces is observed. Each step of this correction method is depicted in Figure 4.2.

The first step is to identify a dispersion-less feature of the EDC, which in this case is the −9.5 eV peak (see 6.3.2). It is important that the feature which is being tracked does not intrinsically change across the dimension one is tracking (e.g. the detector coordinates x,y)[1].

[1]For example, a core level peak, whose position is expected not to depend on momentum, is a good

As a second step, the volumetric data should be computed (binning) along the energy axis in the range containing the spectral feature in question, and along the detector positions X and Y. In order to track the shifts across the detector position, a model best describing the spectral feature, typically a peak-like function, can be fit to the EDC of each position on the detector (see Figure 4.2 panel a). By extracting the centroid of the fitting model, a map of the energy shifts as function of detector position can be created.

A second model, which describes the shape of the energy shift across the detector position can then be fitted to this map (figure 4.2 panel b). In this case, the most prominent effect, which is a result of space-charge, can be fit with a 2D Lorentzian function.

Using the fit parameters of the 2D Lorentzian fitted to the map, the kinetic energy of each electron can then be corrected, directly in the SED, by evaluating the Lorentzian shift from the resulting fit parameters, at the detector position where the electron was detected.

Finally, re-binning the corrected energy column in the SED will reproduce a space-charge corrected energy-momentum volume. In our case, this is shown in Figure 4.2, where the data before (panel c) and after (panel d) the correction is plotted, showing a flat top of the valence band, as expected.

The evaluation of such shifts in kinetic energy based on a single spectral feature however is valid only in case the shift does not change with energy or ToF. In this case, a more complex evaluation, based on multiple spectral features, could be used, where the correction value would then be dependent not only on the detector coordinates but also on the energy value itself.

Furthermore, such methodology can can also be applied along other dimensions than the detector position. An example can be the pump laser fluence, to study or correct the

candidate. The Fermi edge is generally not a good candidate, as in most materials the bands forming it will have some degree of momentum dependence, typically forming a Fermi surface which does not cover the entire momentum space.

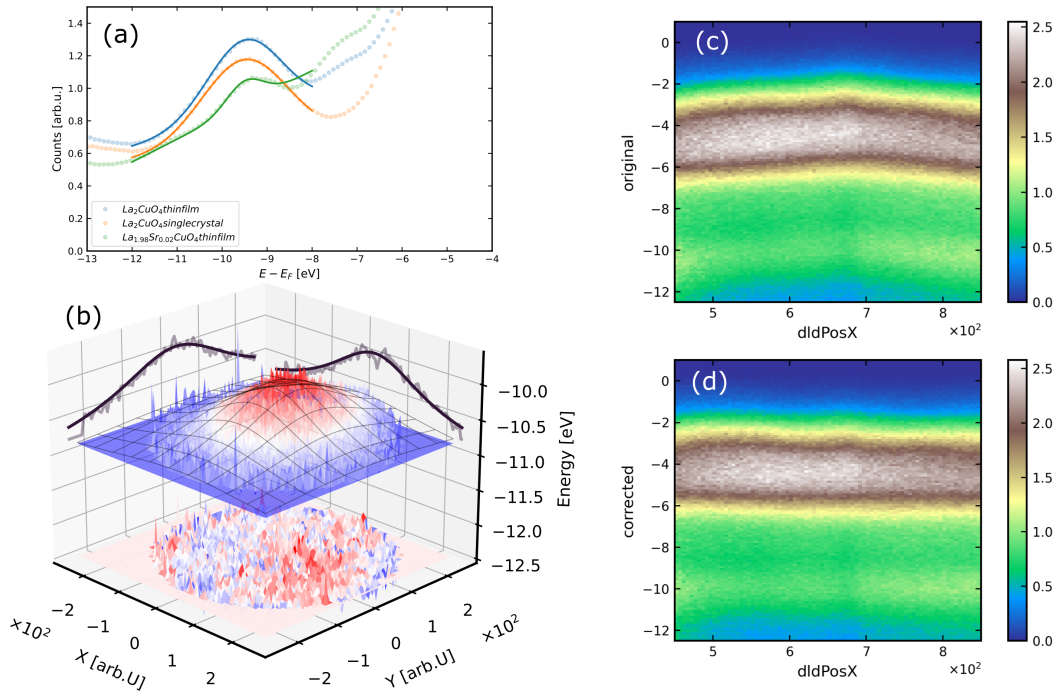

Figure 4.2: Energy shift correction applied across the 2D detector on LCO. Panel (a) shows the fit of a Gaussian plus linear background to a peak in the EDC of LCO, centered at $E = -9.5$ eV. The center of the fitted Gaussian, plotted as a function of detector position (x and y) in panel (b), is used to track shifts across the detector, as this peak is assumed to have no dispersion. A 2D Lorentzian (grid lines) was used fit the data modeling the deformation induced by the space-charge effect (see Section 4.5). The residual from the fit of this model to the data is plotted below the surface. The color coding of the two surface plots extend between their respective minimum and maximum values for visual clarity. Panels (c) and (d) show the EDCs as a function of detector position before and after the correction, respectively.

change in space-charge induced shift due to the variation in pump laser intensity.

4.2 The Momentum Axes

The momentum of the photoemitted electron measured by a momentum microscope can be reconstructed by the direction it takes when emitted. This is resolved by placing a 2D detector, as the DLD, in the back-focal plane of the microscope. The position coordinate where the electron is detected will then linearly relate to the two parallel momentum components. The image obtained on the detector directly reproduces momentum space,

which can be shifted and rotated. Therefore, the two parallel momentum components, k_x and k_y can be reconstructed using simple trigonometry as:

$$\begin{aligned} k_x &= A((X-X_0)\cos\alpha + (Y-Y_0)\sin\alpha), \\ k_y &= A((Y-Y_0)\cos\alpha - (X-X_0)\sin\alpha) \end{aligned} \tag{4.5}$$

where X and Y are the detector coordinates, X_0 and Y_0 the coordinates on the detector of the center of momentum space (i.e. the Γ point), α the angle between detector coordinates and momentum coordinates and finally A is the linear relation between the detector coordinate (pixel) and momentum coordinate (Å^{-1}).

The center of momentum space can only be defined by looking at the momentum image and identifying high symmetry points, or clear features. This is because the momentum image will be shifted on the detector by changes in angle between the sample and the optical axis of the microscope, and cannot therefore be calibrated on one sample for another. This makes it particularly difficult for measuring materials with low contrast dispersion, as the expected symmetries cannot be easily exploited to increase signal-to-noise.

Conversion between detector pixel size and reciprocal space can be coarsely done from the known settings, as one can roughly estimate of the total FOV illuminating the detector. However, determination of an exact conversion requires identifying known points in momentum space (high symmetry points, or repeated Brillouin zones) and measuring the relative distances.

4.2.1 Perpendicular momentum component

The perpendicular component of the momentum vector, k_z can also be resolved, but is not as straight forward as the other components. At first, we need to evaluate the final momentum k_f of the photoemitted electron, as

$$k_{final} = 0.512\frac{m_{eff}}{m}\sqrt{h\nu - E_B + V_0} \tag{4.6}$$

where $h\nu$ is the photo-ionization photon energy, E_B the original binding energy of the electron and V_0 the inner potential referenced to the Fermi energy. As the parallel components of the electrons momentum are conserved in the photoemission process, changes to the photon energy reflect a change in the perpendicular component of momentum. Thks can be explotied to resolve k_z by tuning the photon energy.

Another approach, which can be achieved in a single measurement is to exploit the large momentum FOV and the fact that final states lie on a curved isosurface.[24] When measuring with sufficiently high photo-ionization energies, i.e. in HAXPES, multiple Brillouin zones can fit in the detector FOV. The free-electron-like final states lie on a sphere, whose center is displaced by ${k_{h\nu}}^2$ and with radius k_{final}, as shown in Figure 4.3. The image on the detector maps a section of this sphere on a flat surface, which for different k_x and k_y coordinates will correspond also to different k_z values.

Exploiting this curvature, the perpendicular momentum component k_z can be obtained as

$$k_z = k_{final}\left(1-\cos\left(\arcsin\frac{d}{k_{final}}\right)\right) \tag{4.7}$$

where d is the distance, in momentum space, between the given point and the center of momentum space.

4.2.2 Momentum Distortion Correction

As imaging momentum space on the detector is done with electron lenses, distortions such as barrel or pincushion distortions are common. Many image processing methods are freely available through multiple Python packages, such as `scikit-image` and `OpenCV` will provide plenty of methods to correct for such known distortions for 2D images. Stray fields in the electron optics might however induce higher order distortions, which are not easy to describe mathematically and won't have straight forward correc-

[2] with high photon energy experiments, it is important to take into account the incident photon momentum, as it will result in a shift of the center of momentum space, away from the center of the optical axis of the microscope.

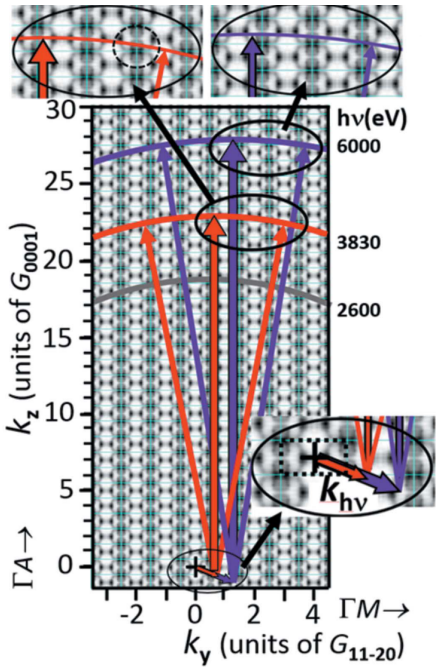

Figure 4.3: Final state sphere and $\vec{k}_{final}$ with photo-ionization energies of 3830 eV (red) and 6 keV (blue) plotted on a background of repeated Brillouin zones of Re(0001) in the xz plane. On the top, a zoomed view shows how the final states cross through the Brillouin zones, giving rise to a k_z variation with k_y (same goes for k_x, not plotted here). Adapted from Medjanik et al. [24]

tion methods. Furthermore, to apply corrections on the SED level, ad-hoc methods need to be defined.

As there is no indication of the relation between position on the detector and momentum space, other than the measured momentum dispersion, the key component is to have sufficiently resolved momentum images. High symmetry points can be used to warp the distorted image onto a regular grid, especially when multiple Brillouin zones are visible. This method can be seen applied in Figure 4.4, applied to an isoenergy surface of the HAXPES measurement performed on YRh_2Si_2. First, the high symmetry points which should sit on a regular grid (a square was used in Figure 4.4 in this case) are labelled, together with the corresponding regular grid points. Then, we identify 4 neighbouring points, and apply a perspective warp, to transform the selection to a square. Tiling together all squares this way, a warped un-distorted image is obtained.

More general approaches also exist, such as those described in Xian, Rettig, and Ernstorfer [68], where symmetrization constrains are used to force image landmarks to fit the expected symmetry.

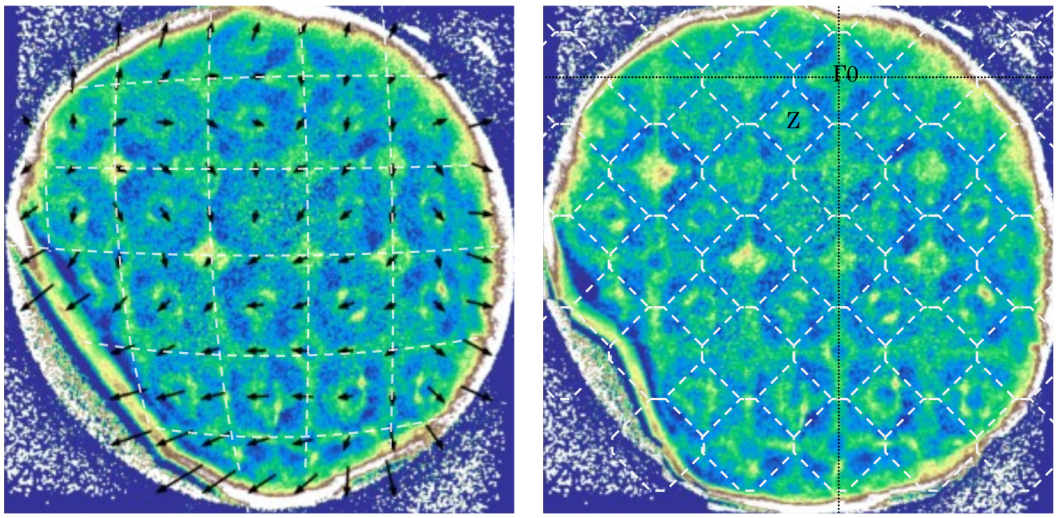

Figure 4.4: Momentum image of an isosurface of YRh_2Si_2 measured with 6 keV showing multiple Brillouin zones in the Field of View. In panel (a) a series of points which should lie on a square grid were selected. The black arrows point from these points to the corresponding regular grid positions they should occupy. In panel (b) shows the image after the per-square perspective warping using these points.

4.3 Pump-Probe Delay

The time axis, or pump-probe delay, on which we aim to observe dynamics induced by bringing the system out of equilibrium using an excitation laser pulse (pump), is encoded in the delay between pump and probe. This is, in HEXTOF, obtained by means of a mechanical delay stage, which varies the optical path of the pump pulse from the pump laser source to the sample. The time delay is therefore resolved by recording the value of the position encoder of the delay stage for each recorded event (detected electron).

The linear relation between encoder value and pump-probe delay time Δt is given by:

$$\Delta t = -enc + t_0 \tag{4.8}$$

where *enc* is the recorded encoder position expressed in picoseconds[3] and t_0 is *time zero*: the encoder value for which the optical path of pump and probe are such that these pulses simultaneously hit the sample.

The SASE process (see Section 2.6.1) behind the FEL lasing is prone to strong fluctuations in the arrival time of each bunch, which results in jitter between the X-ray and the optical pulses. At FLASH, great care has been taken to ensure the best possible synchronization between the electron pulse, and in turn the high energy photon pulse, and the optical laser used to generate the excitation (pump) pulse[56] (see Section 2.6.3). The remaining fluctuations are recorded by means of two separate sensors: the BAM and the Streak Camera (SCam).

- The BAM records the arrival time of the electron bunch at the end of the undulator section. This keeps track of the small fluctuations of the FEL, on the order of few to tens of femtoseconds, for each FEL electron pulse, giving therefore a shot-to-shot correction.
- The SCam, on the other hand, measures the cross-correlation between the optical pump pulse and the high energy FEL pulse. This is done on the average signal of tens of pulses, and can be best used to track long term drifts of the laser system as well as jumps in the laser synchronization, as these would not be picked up by the BAM.

The BAM signal can be used directly for each event, while due to the additional fluctuations in measuring the signal in the SCam, this is usually filtered using a rolling average over acquisition time, as explained in Section 4.4.4 and depicted in Figure 4.5.

Taking into account these corrections, equation 4.8 becomes:

$$\Delta t = -enc + t_0 - t_{SCam} - t_{BAM} \tag{4.9}$$

[3]Internally, the encoder value is converted as $enc_{time} = 2\frac{enc_{position}}{c}$, where c is the speed of light. The laser pulses travel twice the length of the delay stage, as it is typically reflected by a mirror mounted on the moving section of the stage, hence the factor 2.

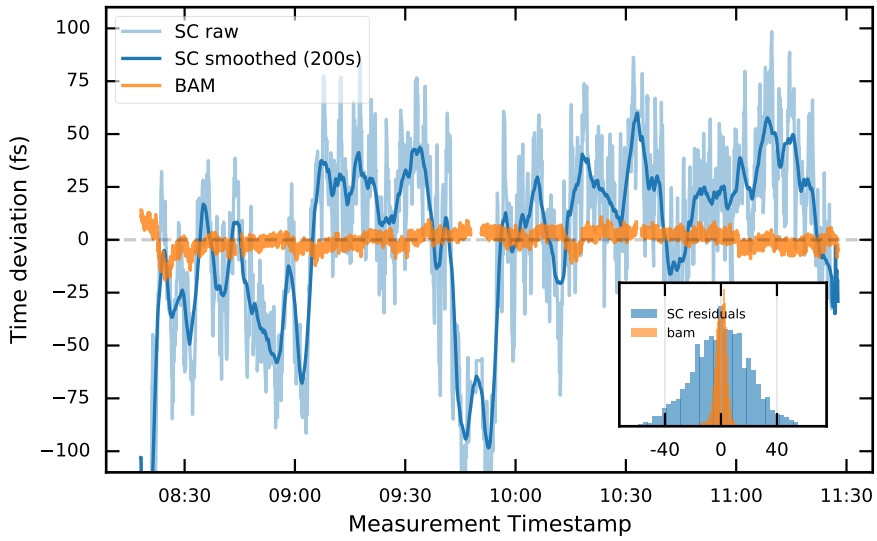

Figure 4.5: Beam Arrival Monitor (BAM) (orange) and Streak Camera (SCam) signal (light blue) over acquisition time. The dark blue curve shows the rolling average of the SC signal with 200 s window. The inset, compares the residual uncertainty filtered out by the rolling average (blue) compared to the distribution of BAM values, emphasizing the timing uncertainty reduction gained with such averaging.

with t_{SCam} being the filtered signal from the SCam and t_{BAM} the direct shot-to-shot values recorded by the BAM.

4.3.1 Pump-probe time overlap

Determination of pump-probe time overlap is an obvious but not trivial task in ultrafast spectroscopy. In all optical experiments, this is easily performed, as cross correlation of the two optical pulses in a non-linear crystal (e.g. a Beta-Barium Borate (BBO)) generates through wave mixing a signal which can be measured by a photodiode. This is not the case inside a photoemission setup, where addition of optics in ultrahigh vacuum would not be possible. Furthermore, the wave mixing method would not work with X-ray and optical pulses.

A first, nanosecond resolution evaluation of the time-overlap can be done by illuminating a metal rod, used as an antenna and connected to an oscilloscope. Aligning in time the rising slope of the singal on the antenna, allows to obtain pump-probe overlap in a time window of around 100 ps. To refine this further, the pump-induced space

charge can be exploited. The so called in-column time overlap, described in detail in Section 4.5.4, produces a strong distortion of the EDC at positive time delays, giving an indication of where the real pump-probe time overlap might sit, with a precision of few tens of picoseconds.

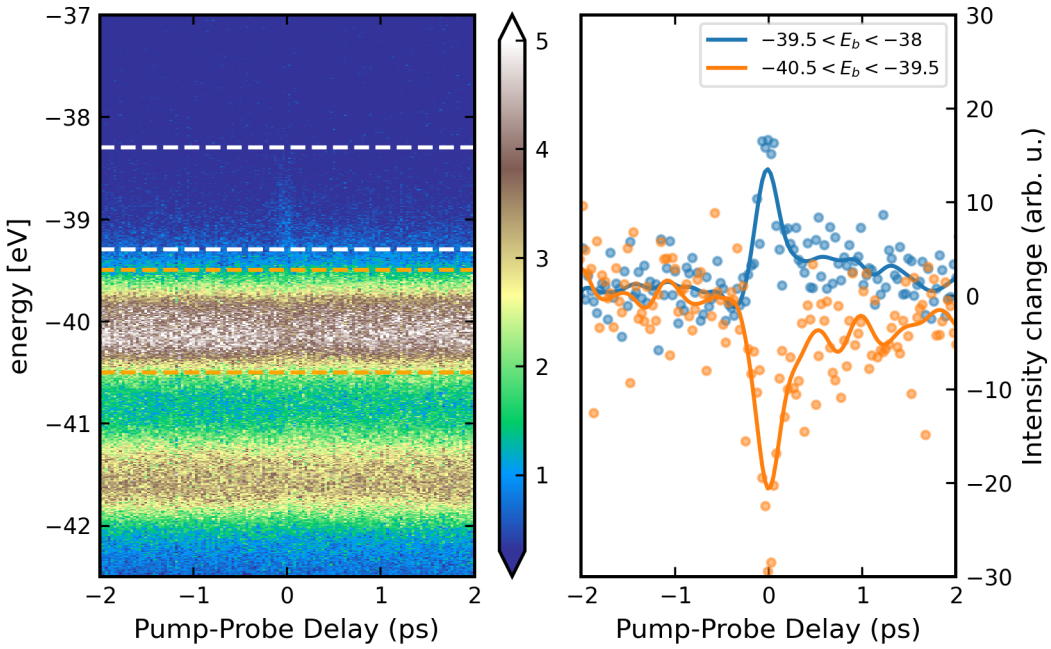

Figure 4.6: Left: Te 4*d* core levels as function of pump-probe delay, measured with *p* polarization. The nPPE signal generating side peaks is clearly visible at $\Delta t = 0$. Integrated energy ranges around the lower binding energy peak (orange) and 1 eV above(blue) are plotted in the right panel. Such features are a common method to track pump-probe time overlap, but require *p* polarization of the pump laser.

Finally, to obtain femtosecond resolution time overlap, signals from the samples one aims to measure need to be used. A phenomena which can accurately indicate the time overlap between pump and probe is multi-photon photoemission (nPPE). When using p-polarized pump pulses, some photoemitted electrons might absorb an optical photon (pump), increasing (or decreasing) its kinetic energy. This leads to side peaks, at higher (lower) binding energies of the main spectroscopic features in the EDC. in Figure 4.6, the side peaks of the Te 4*d* peak in WTe_2 are visible in the left panel. In the right panel, integrated energy ranges show the increase (decrease) of electron counts on the side peak (main peak) region. The time profile can also be used to determine time

resolution, in this case by fitting a Gaussian to the fast nPPE process.

This phenomena does not however manifest as clearly in all materials, as for example in the case of undoped LCO. In the experiment which is presented in Chapter 6, we studied the dynamics in LCO pumped by 3.1 eV photons. Determination of time zero here was done by evaluating the nPPE on a different sample, $TaTe_2$, as plotted in Figure 4.7, and "blindly" measuring in the same region on the actual LCO sample. Once sufficient data had been acquired to observe a small, yet visible step in time, close to the expected time overlap, could be fitted with an ad-hoc defined function to track eventual changes over long acquisition times.

4.3.2 Normalization

The delay stage used in HEXTOF is a linear mechanical stage which is programmed to move back and forth between two set points at a given speed. Because of the algorithm used to ensure smooth movement, the stage lingers on the edges of the swipe ranges for some time. This leads to an uneven amount of time which is spent at each time delay over the acquisition, which produces artifacts in the histogram, as it will show artificially high count rates. Such effect is shown in Figure 4.7 where an artificial spike is evident at 2 ps in panel a.

This artifact can be corrected by normalizing each binned time step in the computed histogram by the result of an identical histogram (along the stage delay axis) performed on a data-frame which instead of electrons, is comprised a row for each probe pulse. This effectively measures the number of photon pulses recorded in each time delay range, Δt, and therefore the acquisition time spent at each time step. The effect of such a normalization is shown in Figure 4.7 panel b, where the artificial side peaks vanish. A less evident but still relevant effect, also corrected with this normalization, is the presence of two steps, at the start and stop points of the scan, as the stage will start and stop at an arbitrary position at the beginning and the end of a measurement run.

Such a normalization can only be performed on the uncorrected delay stage values as

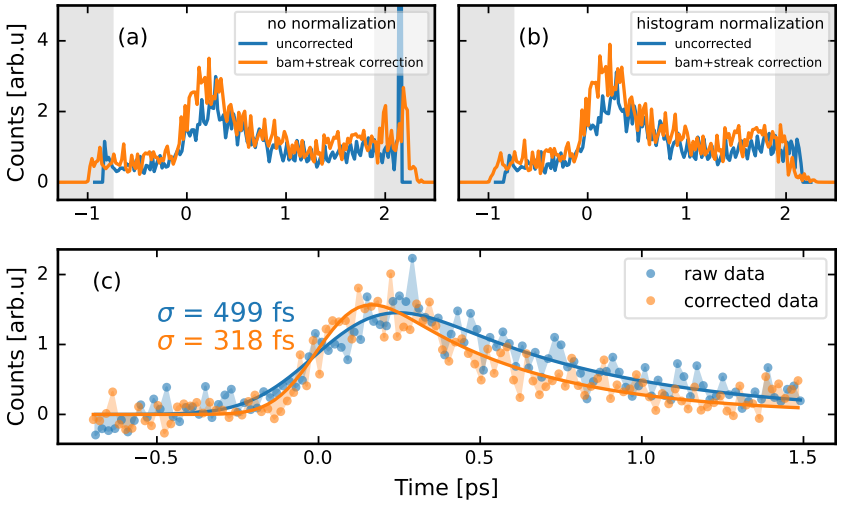

Figure 4.7: Time evolution of electrons above the Fermi level in $TaTe_2$ upon pumping with 3.1eV. In (a) the blue and orange curves show the data before and after correcting for jitter and drifts (BAM and SCam). In panel (b) the same curves but normalized to the acquisition time per point is plotted (see text for details). The main evidence is the disappearance of the artificial spike present in the uncorrected curves at 2.1 ps. Panel (c) demonstrates the increase in time resolution of the BAM and SCam corrections, which reduce the rise time of the electron dynamics by over 100 fs. Here the solid lines are the fit to the data of an exponential decay to a constant level for $t > 1.5$ ps, convoluted with a Gaussian accounting for the pump-probe cross-correlation with $FWHM = \sigma$.

after correcting for BAM and SCam, the relation between each event and the original encoder position is lost. Therefore, in order to apply such normalization, the n-dimensional histogram must be calculated on two pump-probe time dimensions: the BAM and SCam corrected pump-probe time axis, and the uncorrected delay stage axis. This is however difficult when generating high dimensional data sets, for example when binning in energy, both momentum axis and time, as increasing dimensionality, in this case from 4D to 5D can lead to histograms too large to be computed.

An alternative solution is that of normalizing the time-resolved histogram to a dimension perpendicular to the time axis: i.e. the energy axis. With the assumption that the number of electrons in a given binding energy range is conserved upon excitation, e.g. if looking at states below $E_F - h\nu_{pump}$, normalizing the n-dimensional histogram to the integral of electrons in such energy range forces the integral number of detected elec-

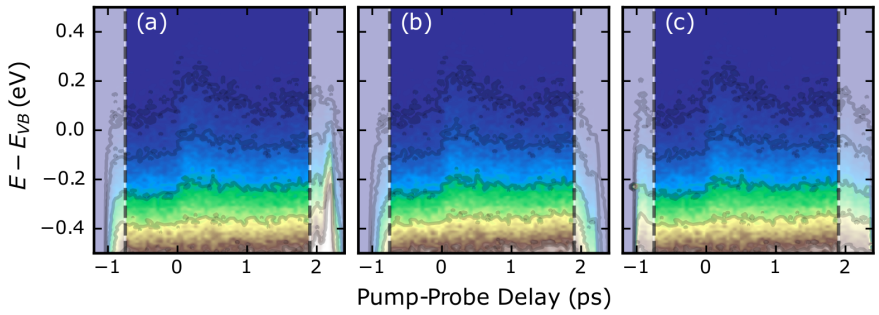

Figure 4.8: Pump-probe time normalization methods compared. All panels shows the EDC of $TaTe_2$ as function delay between FEL pulse and a 3.1eV pump pulse. Panel (a) shows the data uncorrected. Panel (b) shows the data normalized by a histogram of the acquisition time at each delay stage step. Panel (c) shows instead the data divided by the sum all electrons detected at each time step in the energy range −10 eV to −3.1 eV.

trons to be constant throughout the time delay range. In order to retain the amplitude of the EDC, and allow for comparative analysis, the normalization can be done with the mean along the energy range, instead of the sum.

This normalization method is especially useful when looking at false-color plots of 2D data, where changes in intensity along one dimension lead to very evident stripes. Panel c of Figure 4.8 shows this type of normalization, where the data was divided by the mean of the electrons in the range from −10 eV to −3.1 eV.

4.4 Post-Processing and Numerical Methods

In this section I collected some of the correction methods for the most prominent artifacts which appear in MM experiments. Some of these, such as the spherical aberration induced by ToF spectrometers, can often be neglected, as the small induced curvature is often masked by more prominent space-charge effects. Others, such as digitization artifacts are a necessary step in order to avoid introducing numerical artifacts during post-processing.

4.4.1 Pump Fluence Evaluation

Pump-probe experiments are used to study the dynamical response of a sample to an external perturbation. A proper characterization of such a perturbation is therefore crucial for analysing the samples response. The perturbation used in the experiments here presented is an optical laser pulse. The characteristics of optical excitations can be described with 3 elements: photon energy, pulse duration and the incoming fluence.The photon energy is related to the photon frequency by $E = h\nu$ and is defined by the laser system used. At FLASH, the PG2 beamline was equipped with a laser which provides 800 nm photons (1.55 eV) which can be frequency doubled to 400 nm (3.1 eV). A new laser system, PIGLET has been set into operation recently, which provides 1030 nm instead, which can be frequency doubled and tripled.[55]

The time resolution of the experiment, can be determined by measuring the cross-correlation between pump and probe pulses. This is not easily measured when combining optical pump and XUV probe, especially at the sample position within a momentum microscope. This can however still be extracted from measured data of fast processes, such as rise time of electronic excitations in metals, or more reliably the multi-photon photoemission (nPPE) process.[69]

The fluence F, which relates to the number of photons per unit area reaching the sample at each pulse, and can be expressed as

$$F = \frac{P_{avg}}{Rep\ A} = \frac{E_{pulse}}{A} \tag{4.10}$$

where E_{pulse} and P_{avg} are the pulse energy and average power (often the most accessible related measurable) of the laser source, respectively. Rep the lasers repetition rate and A the area of the sample illuminated by the laser pulse.

The absorbed energy density describes how much the system will be driven out of equilibrium. It can be obtained from the fluence, together with the optical properties of the sample under investigation, namely penetration depth d_{pen} and reflectivity R at the

given photon energy $\hbar\omega$. The absorbed energy density can then be obtained as

$$\rho_E = \frac{F\,(1-R(\omega))}{d_{pen}} \tag{4.11}$$

4.4.2 Spot Size Evaluation

As shown in equation 4.10, evaluation of the Fluence, and in turn of the absorbed energy density depends on the laser spot size on the sample.

The electron optics of the HEXTOF momentum microscope can be tuned to image real space, as well as momentum space, on the detector. This allows to take a "picture" of the laser spot, as well as of the FEL spot on the sample.

These pictures reflect the distribution of photo-emitted electrons, which is not always linear with the incident photon fluence. This is due to the work function Φ which electrons must overcome to be extracted from the material, and is linear in case $\hbar\omega > \Phi$ (as is for the FEL photons), but must rely on nPPE when $\hbar\omega < \Phi$, as in the case of the pump pulse.

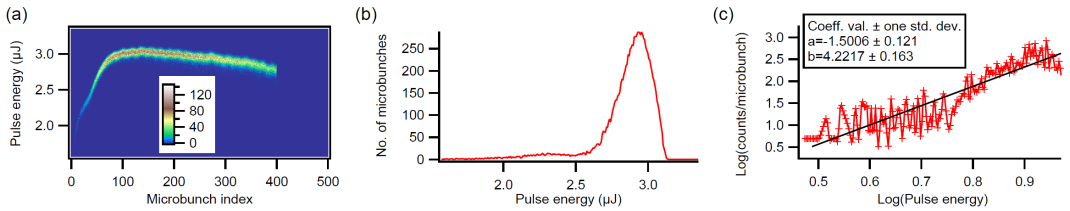

Figure 4.9: 2D histogram of the acquired nPPE generated by the pump pulse as a function of pulse energy and pulse index. In b the number of FEL pulses of the same energy, used for count rate normalization is plotted. In panel c, the Log-log plot showing the dependence of the count-rate per pulse, versus pulse energy is plotted, together with a linear fit. The table shows the fitting results. Adapted from the supplementary material of Dendzik et al. [70]

As described by Dendzik et al. [70] in the supplementary material, the real size of the laser spot is therefore larger than in the image obtained by the detector, as the nPPE process is non-linear. The intensity of the nPPE can be expressed as $I_{nPPE} \propto I^P$, with I the incident photon density (fluence) and p the sample dependent order of the multi-photon transition. As the profile of the laser spot is a (2D) Gaussian, the correct width

of the laser spot can be obtained from the measured nPPE distribution as[70]

$$W^{FWHM} = W^{FWHM}_{nPPE}\sqrt{p} \tag{4.12}$$

The order p can be easily obtained by varying the laser intensity and profiling the nPPE intensity response, since $log(I_{nPPE}) \propto plog(I)$. This is achieved by exploiting the variations of the laser intensity over the course of a measurement run by normalizing the number of events detected by the number of pulses recorded as a function of laser intensity (similar to the pump-probe time normalization, see 4.3.2). As shown in panel c of Figure 4.9, the slope of a fitted line to the log-log plot of the normalized data returns the order of the photoemission process p.

One more aspect which needs to be taken into account when evaluating the spot size from a Gaussian laser spot is how to evaluate the effective illuminated area. Often the approximation of a rectangle formed by the FWHM in the two components of the 2D Gaussian is taken, but this underestimates the area by $\approx$ 13 %. The unity integrated area can be obtained as

$$A = \frac{\pi}{4\ln 2} \cdot X_{FWHM} \cdot Y_{FWHM}. \tag{4.13}$$

Combining all these corrections and taking units into account, fluence and absorbed energy density can be written as

$$F\left[\mathrm{mJ/cm^2}\right] = \frac{4\ln 2}{\pi} \frac{E_{pulse}\,[\mu\mathrm{J}]}{X_{FWHM}\,[\mu\mathrm{m}]\, Y_{FWHM}\,[\mu\mathrm{m}] \cdot p} \cdot 10^5 \tag{4.14}$$

$$\rho_E\left[\mathrm{J/cm^3}\right] = F \cdot \frac{(1-R(\omega))}{d_{pen}(\omega)\,[\mathrm{nm}]} \cdot 10^4 \tag{4.15}$$

where E_{pulse} (µJ) is the pulse energy of the pump laser, X_{FWHM} and Y_{FWHM} are the FWHM of the two components of the 2D Gaussian spot, measured through nPPE of order p on the sample. $R(\omega)$ and $d_{pen}(\omega)$ are the reflectivity and penetration depth of the sample at the pump photon energy ω. The factors 10^5 and 10^4 ensure the correct unit conversion for unit conversion.

A tool is available in `hextof-processor` which takes these effects into account and allows to evaluate on-site the laser spot size, and by extracting the laser intensity from

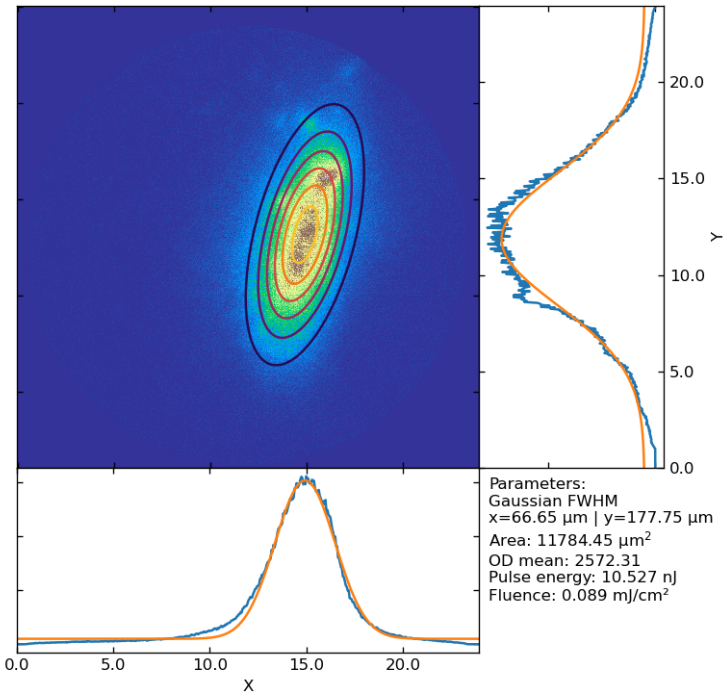

Figure 4.10: Snapshot of the spot-size evaluation tool. A 2D Gaussian is fitted to the spatial image on the detector, generated by nPPE in the main panel. the side panels are projections along the X and Y dimensions, together with the projection of the fit function.

the data, report the corresponding fluence. A snapshot of this tool is shown in Figure 4.10.

4.4.3 Fluence Filtering

The dependence of many interesting physical phenomena on fluence are not linear, and these can be very sensitive to small variations in excitation density. For this reason a stable pump laser power is crucial for high SNR measurements. Nevertheless, the ability to correlate each detected electron to the corresponding laser fluence, allows to selectively filter those events which correspond to a certain fluence range. This can be exploited both, to reduce undesired fluctuations, but also to resolve a fluence dependence in the fluctuation range.

A simple example is the case above, where the order of the photoemission process can be deduced from laser intensity fluctuations. The pump laser amplifier operates in

a burst mode, synchronized to the FEL pulse structure. Unfortunately, within the burst the pulse energy changes from pulse to pulse in a characteristic time profile. This time dependence can be rather drastic, as shown in Fig. 4.11, and needs particular attention. Especially so, as the intensity of the FEL pulses also have a built in variation of X-ray fluence within the bunch. In the worst case the intensity pattern within the X-ray bunch can have an opposite trend to that of the pump pulse train, leading to the majority of the photoemitted electrons providing information of the material excited at lower fluence than the set value.

For example, a common case is that the laser power builds up throughout the first 50 - 100 pulses in a bunch, reaching the set value. The FEL intensity instead often has the highest intensity (and in turn the highest photoelectron yield) in the first pulses of the bunch. Such a situation leads to more electrons being recorded with low pump fluence (first 50-100 bunches) than those having the desired fluence value.

This scenario is shown in Fig. 4.11, where the blue line shows the trend of the FEL intensity across the bunch, while the false-color plot indicates the number of electrons measured as a function of laser fluence across the bunch. Here, the majority of the recorded electrons were measured with a laser fluence, whose value is less than half of the set obtained from considering the average laser power entering the experimental chamber.

4.4.4 Smoothing Columns by Rolling Average

Columns in the SED which contain parameters used for data corrections, i.e, X-ray photon energy after the monochromator, sample bias or SCam, are all measured quantities, and are therefore subject to noise. In order to avoid introducing such uncertainties as noise on the physical axis (i.e. the kinetic energy), these measured parameters are first averaged using a rolling average over acquisition time.

The averaging window differs from parameter to parameter, ranging from 1 s for low noise channels, such as sample bias or monochromator photon energy, to 200 s or even

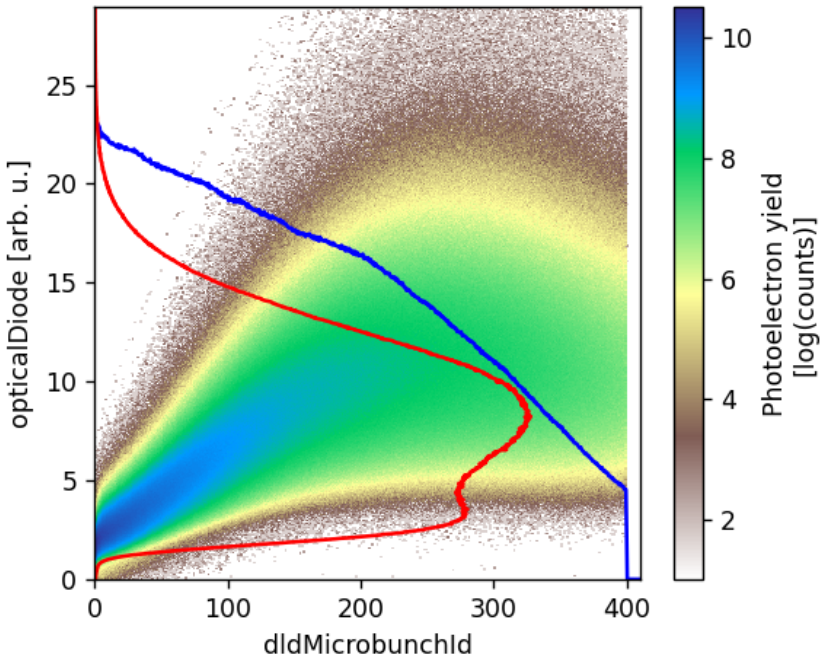

Figure 4.11: Blue curve: photoelectron yield as function of pulse ID, i.e. across a pulse train. Red Curve: photoelectron yield as function of laser intensity, plotted on the y axis. The false-color plot shows the number of photoelectrons detected as function of laser intensity across the pulse train.

more, for high noise parameters such as the SCam. This allows one to smooth out the noise while retaining possible fast changes which might occur while measuring. Figure 4.5 shows how the signal from the SCam changes before and after the rolling average filtering.

A downside of rolling averages, is that the missing data points create gaps in the filtered data, as big as the rolling window on both sides of the missing data point. In order not to loose these data, we interpolate the missing values with the average of the previous (and following) values.

4.4.5 Sector Alignment Correction

Different meanders of the DLD detectors (see Chapter 2.3.1) are sitting in slightly different positions along the electron travel direction. This creates an artificial time shift

between electrons detected in one or the other sector. Such differences are corrected for on the hardware level, but small deviations may still remain, and are visible in the data. Compensation of such time shifts can be done by measuring the arrival time of the photon peak[4], and subtracting the differences from the recorded electron arrival time.

The evaluation of such shift needs to be performed when changes to the DLD are made (bakeout, reinstallation of ACU unit), but can be stored in between and reused for multiple data acquisition runs.

4.4.6 Digitization artifact

The recorded values of the photoelectron arrival time are digitized by an analog-to-digital converter (ADC) in the DLD electronics. Applying a non-linear transformation (time-of-flight to photoelectron energy) to an axis with integer values, will result in an uneven distribution of values (e.g. of kinetic energy) which can lead to artifacts when calculating the photoemission event histogram, as can be seen in Figure 4.12. The discretized axis can be transformed to a smooth "analog-like" axis by adding noise. This noise should be formed by random values in the range of one step of the discrete axis. This, however, should be done only when the instrument resolution is much larger than one digital step, as adding such noise slightly increases the uncertainty (< 0.4 sampling steps) along this dimension. In the case of the HEXTOF machine at FLASH, the sampling step is around 1 meV while the energy resolution is at best about to 20 meV.

4.5 Space Charge

As was mentioned above, in photoemission experiments, a major limitation in the acquisition rate is caused by the Coulomb repulsion between electrons. This effect is commonly referred to as a vacuum-space-charge, or just Space-Charge (SC) effect, and poses the ultimate limitation to many improvements one can make to photoemission experi-

[4]The so called *photon peak* is the signal detected in the time-of-flight spectra, generated by photons reflected from the sample and reaching the detector. As the time it takes photons to travel through the column is negligible compared to the electrons time-of-flight, the resulting signal can be considered simultaneous with the pulse arrival time.

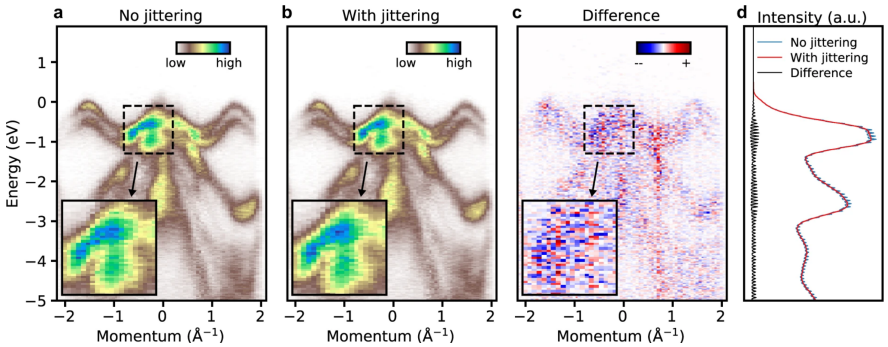

Figure 4.12: Digitization artifact correction applied to WSe_2 data. Panel **d** emphasizes the digitization artifact obtained binning with incommensurate binning and data steps. From Xian et al. [59].

ments. For example, decreasing the photo-ionization (X-ray) spot size, to target smaller and more homogeneous spots, as well as decreasing its time profile (from nanoseconds of synchrotrons to femtoseconds of FELs) to obtain short time resolutions and even increasing its intensity, all are ultimately limited by the increase in SC they produce.

This becomes even more challenging when performing pump-probe experiments, as even more electrons are being photoemitted by the, typically very intense, pump pulse. This section will describe this effect and its repercussions in simple and time-resolved photoemission. In the following pages, some correction methods will be introduced, as well as optimizations of the acquisition setup which can minimize such effects.

4.5.1 Energy Distribution and Secondary Electrons

All experiments where electrons are being detected are subject to some degree of Space-Charge, but a major difference in the case of photoemission is the large energy range of the photoemitted electrons. Illuminating a sample with a beam of photons with energy $h\nu$, leads to the emission of photoelectrons with kinetic energies ranging from 0 (originating at the Fermi edge) up to $h\nu - \phi$, where ϕ is the work function of the material.

Furthermore, photoemitted electrons leave behind holes, which cause a cascade of low-energy electrons driven by Auger processes or inelastic scattering. Amongst these, those electrons which will have more energy than the work function will be emitted to-

gether with the primary photoelectrons. These secondary electrons strongly outnumber the primary photoelectrons and create a strong, low-kinetic energy background.

In MM, almost all electrons emitted from the sample are collected by the input of the microscope and are driven through the electron optics, including these secondary-electrons. The increase in space charge effects due to the high density of secondary electrons is therefore drastic.

The polychromatic distribution of photoelectrons will have the electrons at higher kinetic energies travelling faster, and passing ahead of the slower ones. This means they will feel a Coulomb repulsion from the large density of slower electrons (those with lower kinetic energies and secondaries combined), and get accelerated to higher kinetic energies at which they will be detected.

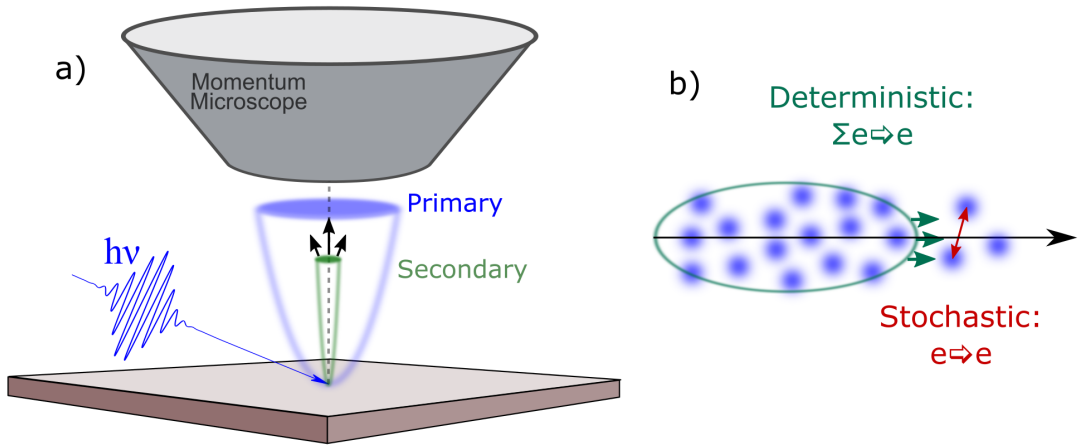

Figure 4.13: Panel (a) shows a sketch of the SC effect induced by the slower secondary on the main photoelectrons of interest. A photon pulse of energy $h\nu$ excites multiple electrons from the sample. The green cloud represents the slower secondary electrons, which result from scattered photoemitted electrons and contribute to accelerating the main photoelectrons, depicted as a blue cloud. Panel (b) illustrates the two component of the simple SC model described in the text.

4.5.2 Static Space-Charge

The main effects of the Coulomb repulsion can be treated as: (a) a deterministic part and (b) a stochastic part,[67] depicted in green and red in panel b of Figure 4.13. The stochas-

tic part, governed by single electron-electron scattering, leads to broadening/smearing of the electron distribution (similar to heating). This effect can be drastic, as both energy and momentum information can be lost in these processes. The deterministic part instead, stems from the electrostatic (average) field a single photoelectron feels, generated by the electron charge distribution (electron cloud).

While the stochastic effect is typically smaller than the deterministic effect (which only induces a rigid shift of the energies), it cannot be corrected, and can only be minimized by reducing the electron cloud density (e.g. reducing the photo-ionization fluence). The deterministic shift can instead still be compensated in post-processing, if the corresponding broadening is not too severe.

In a momentum microscope, a voltage is applied between sample and microscope, which accelerates electrons, guiding them into the microscope. This voltage affects the fast and slow electrons differently. The fast ones, which will have a larger velocity component parallel to the sample, will diverge and take a disk-like shape at the entrance of the microscope. The slow electrons will instead stay concentrated and can therefore be treated as a point source of the electric field.

The cloud of higher kinetic energy electrons will thus be "pushed" by the slow "point charge" of the slow electrons (mainly the secondaries). This push will have a radial distribution which leads to a Lorentzian-like energy shift across the detector,[71] with a stronger push in the center of the optical axis, decreasing towards the edges of the detector.

This process is depicted in panel (a) of Figure 4.13 where the cloud of primary electrons (blue) is followed by the slower secondary electron cloud (green). The transversal momenta of the secondaries is small compared to that of the primary electrons. The radius of the primary electron cloud is the maximum parallel momentum, determined by $k_{max} = 0.512\sqrt{E_{kin}}$. For a 55 eV photons[5], this yields a disk of radius 3.7 Å^{-1}, while

[5] 55 eV is the photon energy at which FLASH was tuned during our La_2CuO_4 experiments, presented

a radius of just 0.7 $\mathring{A}^{-1}$ is produced by secondaries of 2 eV.

The phenomenological model introduced in this section can be used to correct for the SC induced shift, by using the method described in Section 4.1.5, and visualized in Figure 4.2. Here a spectral feature of the EDC is used to evaluate the space-charge induced shift, i.e. the deterministic part, which is then used to correct the energy axis, while stochastic component is however neglected.

4.5.3 Pump-induced Space-Charge

The Space-Charge problem becomes even more severe when performing pump-probe experiments, as here not one but two photon sources generate electron clouds which contribute to SC. The pump pulse, with photon energies typically below the work function of the material, will generate photoelectrons through multi-photon photoemission (nPPE) by interaction of the same electron with multiple pump photons, inside the crystal.

Even though orders of magnitude less efficient than the direct photoemission with high energy photons, the high intensity pump pulses, typically required to bring the sample out of equilibrium, will result in generation of a large number of secondary photoelectrons. These will have low kinetic energies compared to the main photoelectrons, generated by the FEL pulse, and will therefore play a similar role to that of the secondary electrons generated by the photo-ionization pulse.

There is however a major difference to treating the effect of pump induced secondaries to treating the effect of secondaries generated by the FEL. Namely in the pump-probe experiment, the delay between the pump and probe is varied.

In fact, the time at which the slow electron cloud generated by the pump pulse with respect to when the primary photoelectrons will be generated by the FEL pulse, i.e. the pump-probe time-delay, will strongly affect the magnitude of the pump-induced

in Chapter 6

SC. This can be particularly detrimental to pump-probe experiments, as the time-delay dependence of the SC can deform or even completely mask the dynamics one aims to measure with such experiments.

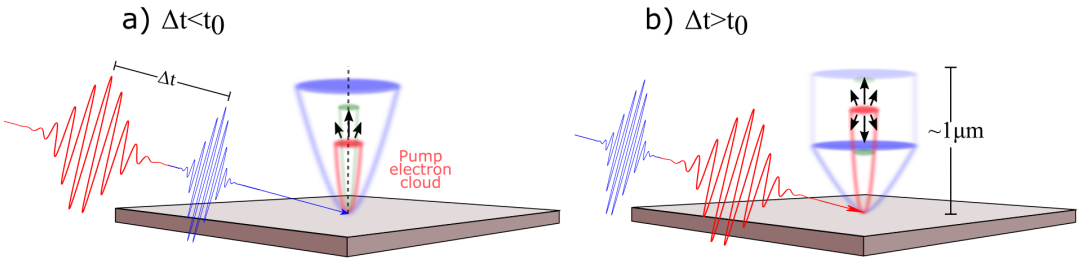

Figure 4.14: Schematic view of the pump-induced SC effect. At negative time delays, When the probe pulse hits the sample before the pump, the Coulomb repulsion felt by the primary photoelectrons will be only positive. At positive time delays instead, the slow electron cloud generated by the pump pulse forms in front of the primary photoelectrons, effectively slowing them down before they pierce through the cloud, after which they will be accelerated again. This process takes place in the first micrometers from the sample surface.

A mean-field model, based on the same models used to describe the "static" SC, can be used to describe the pump-induced SC effect. The electron cloud generated by the pump pulse can be approximated by a homogeneous disk which moves slowly along the vertical direction towards the microscope. The primary electrons, with much higher kinetic energies, can instead be assumed as single electrons, travelling (only) in the vertical direction. At negative time delays $\Delta t < 0$, the pump pulse hits the sample after the probe pulse has generated the primary electron(s). Therefore the repulsive electrostatic potential from the pump-induced electron cloud will act as a pushing force, increasing the kinetic energy of the primary electrons. At positive time delays however, with $\Delta t > 0$, the pump-induced electron cloud is being generated "ahead" of the primary electrons. This cloud will at first slow down the primary electron(s) (Figure 4.14 a). As the primaries are faster than the pump-induced (secondary) photoelectrons, they will eventually pierce through the slow electron cloud and find themselves ahead of it, feeling again the accelerating push (Figure 4.14 b). This effectively reduces the overall SC shift

induced by the pump, while still increasing the broadening induced by the stochastic effects.

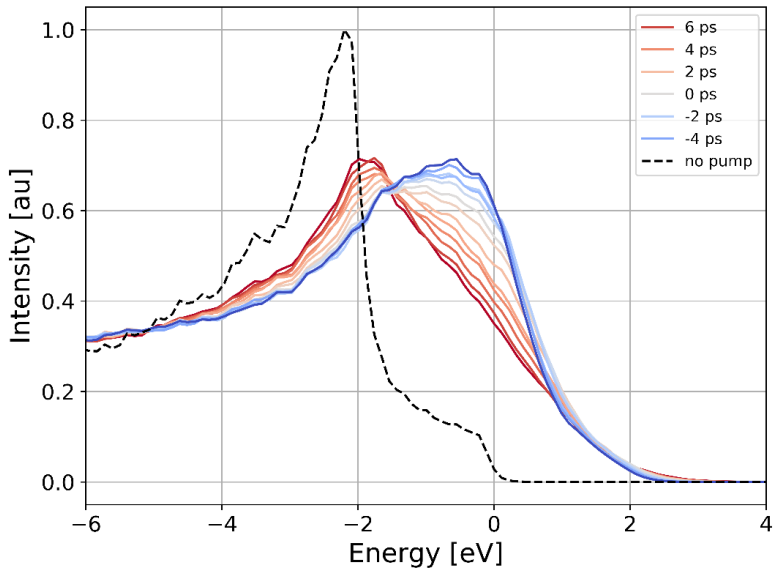

Figure 4.15: Pump-probe dependence of Cu(100) measured with HEXTOF. The black dotted line shows the un-pumped (i.e. no optical pump laser) EDC from the last pulses of each pulse train. The sharp d-band and Fermi edge indicate SC contributions from the FEL are small, or negligible. The other curves, from blue to red, show the changes in the EDC measured as function of pump-probe delay. Already at negative time delays, SC is very strong, shifting the data by over 2 eV. The peculiar "back shift" of the main peak as the delay grows beyond the time overlap, is due to the "pull-push" effect of pump-induced SC, described in the text.

In Figure 4.15 the pump-induced Space-Charge (SC) observed on a Cu(100) crystal is depicted, together with the un-pumped (pump laser off) "static" EDC. As the probe (FEL) intensity is the same in pumped and static curves, the large average shift of the EDC by $\approx$ 2 eV is entirely due to the pump-induced SC. The change of the profile as a function of time delay shows the difference between the "push only" behaviour for $\Delta t < 0$ and the "pull-push" behaviour for $\Delta t > 0$.

4.5.4 In column Pump-Probe time overlap

The characteristic time-delay-dependent shift induced by the pump-induced Space-Charge, can also be used as a "feature" in order to find the temporal overlap t_0 between the pump and the probe pulses. This can actually be very useful, as techniques commonly used in ultrafast spectroscopy to determine t_0, such as cross correlation in a non linear crystal, are not viable options in time-resolved photoemission experiments.

While attempting to find temporal overlap using this approach during a beam-time with the HEXTOF machine at FLASH, we encountered an artefact which shows a very similar behaviour, but its position does not correspond to the "time zero" we were looking for. Such feature, which we referred to as "fake time zero" or "in column time overlap", can be observed in panel a of Figure 4.16. A pronounced shift of the EDC, peaked at $\approx$ 15 ps is visible in panel (a), while panel (c) shows the shift (blue) and broadening (green) as a function of pump-probe delay. These were obtained by fitting the data to the convolution of a Gaussian function with the static data, as explained in Section 4.5.5.

The artefact is closely related to the phenomena which governs the time-delay dependent space-charge shift, with the main difference being that this effect takes place inside the electron lenses of the microscope and not at the sample position. In fact, in a standard configuration of the momentum microscope the slow pump-induced electron cloud is also collected into the microscope by the positive bias voltage applied between the sample and microscope input, i.e. the sample bias.

Ray-tracing simulations,[35] as those show in in Figure 2.3 have show that this slow electron cloud gets focused somewhere in the microscope column. In the focus it generates a strong, point-like field which is felt by the fast photoelectrons travelling through the microscope. The fast electrons which overlap with this slow cloud within the microscope column are those generated tens of picoseconds after the photo-induced slow electron of the cloud. The time-delay where this artefact appears is given by the difference in

velocities between the fast primaries and the slow pump-induced photo-electrons. As the velocity of the slow pump electrons is mainly governed by the sample bias, the time difference between "real" and "fake" time zero, can be controlled by changing this voltage.

The nature of this artifact however ensures that such fake time zero t_{fake} will always appear at positive time delays, with a rising tail which is often still seen at t_0.

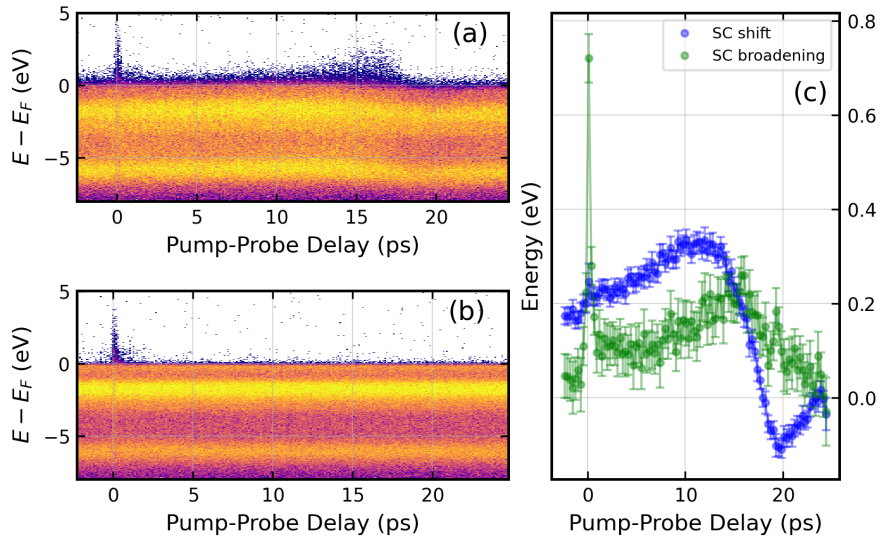

Figure 4.16: In column time overlap, or "fake time zero", shown on EDCs of $TaTe_2$. In panel (a), the data collected in extractor mode shows clearly both "real" and "fake" t_0, at $t = 0$ and $t = 17$ ps respectively. Panel (b) shows the same data, measured using the momentum microscope in "repeller" mode, where "fake time zero" has disappeared completely.In panel (c) the shift and broadening induced by the pump laser are plotted. These were obtained by fitting the convolution of a Gaussian kernel with un-pumped data (FEL only, no pump laser) to the pumped data. The spike in broadening at $t = 0$ is due to the failure of the model used to represent the LAPE which generates the prominent peak above the Fermi level, as well as the dip below, during pump-probe time overlap.

In Figure 4.16, panel (a) shows the EDC close to the Fermi edge of 1T-$TaTe_2$ as a function of pump-probe delay. Here the Laser-Assisted PhotoEmission (LAPE) signal generated during the pump-probe time overlap is visible at $t = 0$. A prominent "fake time zero" can also be seen, with the peak intensity and sign inversion at 17 ps. In panel (b), the extracted (see above) shift and broadening of the EDC, caused by the pump laser

are plotted, showing the derivative-like shape and peaked shape respectively, centered at t_{fake}. While this approach is now commonly used to get a rough estimate of the position of "real" t_0, the effect can be very detrimental to the experiment as it strongly reduces the time-delay window where the dynamics are artefacts free.

4.5.5 Fitting model for pump induced space-charge effects

The laser and FEL pulse structure available at FLASH offers more FEL pulses than optical pulses in each bunch (see Section 2.6). This allows to record, together with the time-resolved data, also "un-pumped" data simultaneously. Such data is especially useful for evaluating the pump-induced space charge. Having both pumped and un-pumped data, the two component model used to describe static SC can be used here to fit the effects of the pump-induced space-charge.

This model can be described mathematically as the convolution of a non-centered Gaussian kernel with the space-charge free EDC. The width of the Gaussian distribution in the kernel will model the broadening. The shift instead can be controlled by the deviation from the center of the kernel of the center of the Gaussian distribution.

A function can be made which applies such convolution on the un-pumped data, and can then be used to fit the pumped data. The two free parameters, set by the width and off-center deviation of the Gaussian kernel will give a good approximation of the broadening and shift induced by space-charge originating from the pump laser. This is however works only in the small SC perturbation regime, and fails when the stochastic component becomes too large.

This fitting routine was applied to the evaluations shown in Figure 4.17, where the static data (gray line) was used to fit the data pumped at different fluences. In Figure 4.16 the EDC at each time point of the data shown in panel (a) was fitted with this model. The fit parameters obtained are shown in panel (c).

4.5.6 Microscope Correction: The "Repeller" Mode

As already mentioned, the distortions induced by the in-column time overlap can be controlled by changing the voltage between the sample and the microscope input. However, the same bias voltage is used to control which kinetic energy will be in the ToF focus of the microscope, and therefore select the energy range of interest

A new electron lens design was developed, which allows to simultaneously reduce SC and prevent "fake time zero" altogether.[72] This consists mainly of applying a negative voltage between the sample and the detector. This results in the slower (secondary) electrons generated both by pump and probe pulses to be pushed back towards the sample (hence the name "repeller" mode), instead of being collected in the microscope column. Therefore the SC is dramaticaly reduced. Such a microscope mode greatly increases the excitation density range which can be used with this technique, as pump-induced SC effects kick-in at laser intensities that are more than an order of magnitude higher than in the standard configuration.

The comparison between the two modes is depicted in Figure 4.17, where in both panels the "static" EDCs (i.e. with no pump laser) are plotted in gray, and compared to the EDCs after excitation with pump pulses of different intensity. With the microscope in extractor mode, a pump fluence of 5 mJ/cm^2 is sufficient to induce a SC shift of $\approx$ 300 meV (red curve, top panel of figure (4.17). In "repeller" mode, instead, a smaller SC shift of $\approx$ 100 meV is obtained with a fluence five times larger (22 mJ/cm^2). It is not until above 30 mJ/cm^2 that the stochastic electron-electron scattering becomes dominant and smears the EDC to an unrecoverable state.

It is to be noted that the "repeller" mode used for these measurements was an adaptation of the standard momentum micrscope configuration. A dedicated lens design is expected to outperform these improvements by an order of magnitude or even more, at the cost of momentum FOV, which is reduced to about 1.5 Å^{-1}.[72]

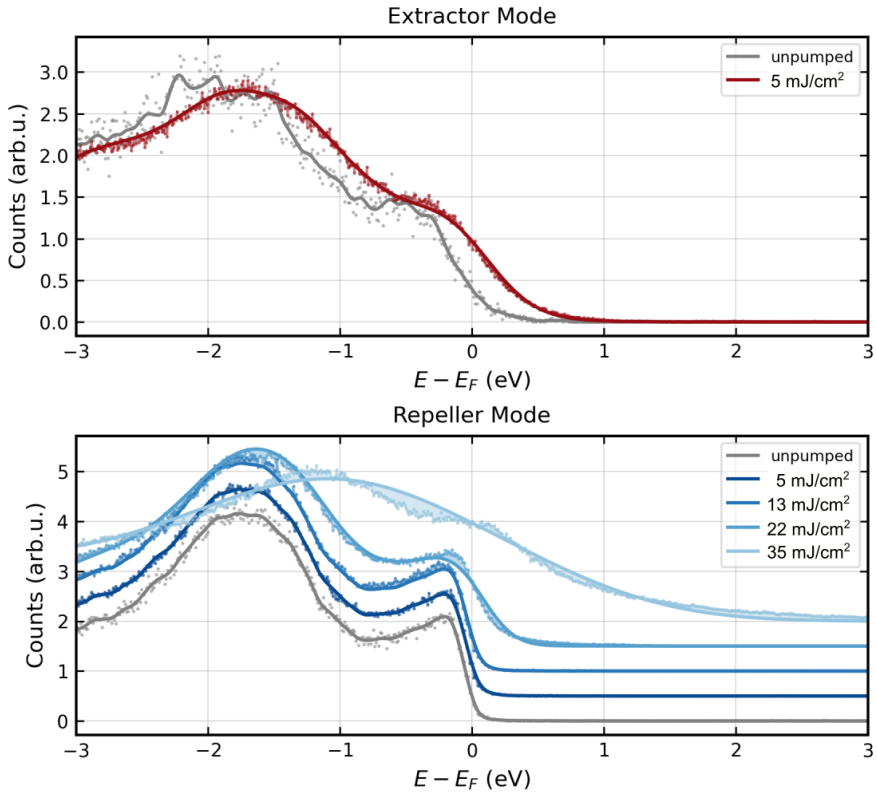

Figure 4.17: Space-Charge (SC) induced energy shift and broadening in $TaTe_2$, measured with a momentum microscope in "extractor" mode (top) and "repeller" mode (bottom). The solid lines show the fit of the convolution of a Gaussian kernel with the "static" (unpumped) data to EDCs recorded after pumping with different fluences.

Concluding remarks

This chapter summarized most of the technical aspects of the data processing tools developed for time-resolved momentum microscopy. The different calibration and correction methods for the kinetic or binding energy, momentum and pump-probe delay axes were described in detail. Methods used to correctly evaluate the fluence and absorbed energy density of the pump laser in pump-probe measurements were also provided, together with other post processing methods and numerical artefact corrections.

An extensive section was dedicated then to the Space-Charge effects, as these are probably the most troublesome problems in time-resolved photoemission. However some correction methods which helped our analysis were presented, together with an out-

look to future machine improvements which could strongly reduce the impact of the SC effects.

CHAPTER 5

$YbRh_2Si_2$

This chapter summarizes the results obtained from High Energy X-Ray Photoelectron Spectroscopy (HAXPES) momentum microscopy measurements on the prototypical heavy fermion Kondo lattice system $YbRh_2Si_2$. The most interesting properties of these strong correlated electron have origin in the electronic states near the Fermi surface. In superconductors, the many-body interactions lead to the opening of a gap in this region. In Kondo systems however, the density of states at the Fermi surface is increased at low temperatures.

The aim of this work was to study the temperature dependence of the Fermi surface of this system, and understand at what temperature, above the Kondo temperature T_K, the transition from a large to small Fermi surface takes place. We chose hard X-ray momentum microscopy as the ideal technique as it provided us with two advantages: the bulk sensitivity and wide FOV, that avoids surface states and resolve the full 3d-momentum space Fermi surfaces.

Studying this system at temperatures from 20 K to 300 K, we could show how the large Fermi surface, typical of Kondo systems survives up to 200 K, well above the Kondo

transition temperature of 25 K.

All figures and information contained in this chapter is derived from the work published as Agustsson et al. [2].

5.1 Heavy Fermion Compounds

Heavy fermion systems are intermetallic compounds characterised by partially filled 4*f* or 5*f* electron shells which, interacting with the itinerant electrons, lead to quenching of local magnetic moments. This is caused by the formation of Kondo spin-singlet many-body states and leads to a drastic increase of the effective mass of conduction electrons, hence the name *heavy fermion*.

In superconductors, electron correlations give rise the formation of cooper-pairs, which form a gap near the Fermi surface, leading to a reduction of the single-particle EDC observed in photoemission spectroscopy measurements. In Kondo systems instead, the correlated state resulting from hybridization of the f-shell electrons with conduction electrons, which form Kondo singlets, leads to an increase of the density in states at the Fermi surface, below the characteristic transition temperature T_K. As photoemission spectroscopy is measures the occupied electronic states, correlated states such as cooper-pairs or Kondo singlets are not directly observable using this technique. However, the hybridization between the f-states and the itinerant electrons leads to an increase of the the electronic density of states, which can be observed through photoemission.[73]

Also the momentum dependence of the states forming the Fermi surface reacts to the formation of Kondo quasiparticles and changes topology. As the conduction electrons increase their effective mass, the hybridized f-electrons are included in the Fermi surface.[75] If the screening of the magnetic moments is lifted, either by formation of an ordered magnetic state at lower temperature, or by breaking the Kondo coupling above the Kondo temperature T_K, the f electrons are again excluded from the Fermi surface. These two pictures are known as the large and small Fermi surfaces, respectively.[76,77]

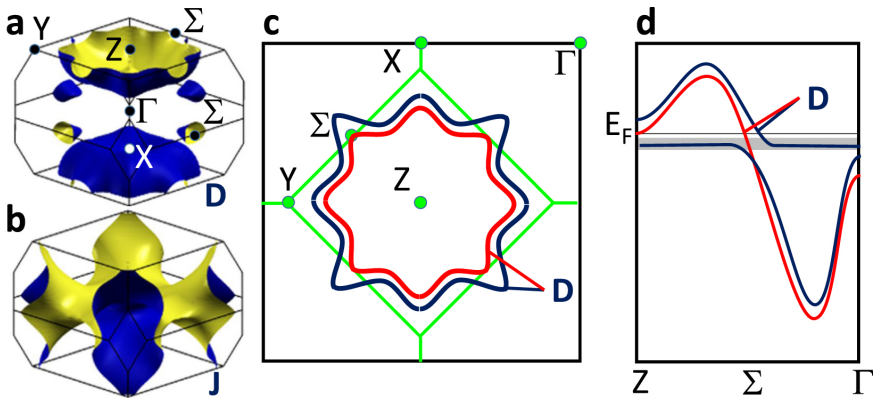

Figure 5.1: Panels (a) and (b) show the Fermi surface of $YbRh_2Si_2$ from calculations, showing the doughnut sheed D (a) and the jungle-jim sheet J (b), as presented in Rourke et al. [74]. Panel (c) shows a schematic representation of the large and small Fermi surfaces in a cut through the doughnut along the $Z-Y-\Sigma$ plane. Panel (d) shows the schematic band dispersion along the $Z-\Sigma-\Gamma$ direction, for the correlated state (blue) and the high temperature uncorrelated state (red). The gray area indicates the non-dispersing f-electron states. From Agustsson et al. [2]

An example can be seen in Figure 5.1, where the blue and red lines in panel c represent a schematic view of the large and small Fermi surface in $YbRh_2Si_2$.

The large Fermi surface formed in the Kondo phase is reduced to the small Fermi surface when reaching below the Néel temperature T_N, at around 70 mK in $YbRh_2Si_2$. When increasing the temperature instead, the temperature at which the small Fermi surface is formed is still under discussion. The Anderson model[78] predicts the Kondo transition temperature t_K, with the loss of coherence in the heavy fermion quasiparticles, to coincide with the formation of the small Fermi surface. In contrast, dynamical mean-field theory calculations[79] predict a higher temperature for this transition. Angle-resolved photoemission experiments[80] have shown a large Fermi surface, up to 100 K.

5.2 Method

This work differs from what is presented in the rest of this thesis as it is the only experiment not performed with HEXTOF. Here we performed HAXPES measurements using a momentum microscope installed at the P22 beamline of the storage ring PETRA III at

DESY in Hamburg. Samples were grown in Frankfurt, using high-temperature indium-flux, as described in Krellner et al. [81], and were fixed on the sample holder, orientated with the (100) plane parallel to the sample holder, with an epoxy resin. The samples were cleaved using a wire cutter prior the measurement. High energy X-ray photon energy was selected with a Si(311) double-crystal monochromator, producing 5.297 keV photons with a bandwidth of 155 meV.

5.2.1 Bulk sensitive momentum microscopy

As was mentioned above, the choice of high energy X-ray photons has a double advantage: the bulk sensitivity and the large FOV. The increase of inelastic mean free path for the electrons excited with hard X-rays allows one to gain bulk sensitivity in photoemission measurements.

Typically, surface states dominate, as signals originating at the surface outweight those originating from electrons sitting deeper inside the crystal. Increasing the electron mean free path, however, allows more electrons from the deeper layers of the material to escape from the surface, and be detected, increasing the relative count of "bulk" electrons as compared to surface electrons. This comes at the cost of the low cross section and significantly increased background. Momentum microscopy is the ideal tool to overcome these issues, with the high efficiency full 3D acquisition.

5.2.2 Decoupling bands and diffraction

The long paths the bulk electrons need to travel through the crystal create strong diffraction patterns on top of the band structure which we aim to study. These diffraction patterns however can be removed and treated as background when exploiting the little variation they show as a function of energy.

By smoothing (low pass filtering with a Gaussian kernel) the data along the energy axis, the diffraction patterns are isolated from the band structure. Subtracting this from the original data acts in effect as a high pass filter, resulting in amplified band structure features and minimised diffraction patterns. This way, we were able to resolve the band

structure of $YbRh_2Si_2$ resulting from deep lying bulk states, with no visible trace of surface states.[82,83]

5.2.3 Full 3D momentum reconstruction

The other advantage of high energy X-ray photoemission is the large FOV obtained when applied to momentum microscopy. With the microscope settings and photon energy we used, we could observe a momentum FOV of over 12 $Å^{-1}$, encompassing over 25 full BZ simultaneously.

In such a large FOV, the perpendicular momentum shows a strong change across the detector, covering a range of $\Delta k_z = 0.5\ G_{001}$, with G_{001} being the reciprocal vector in the perpendicular momentum direction. Using the perpendicular momentum component reconstruction technique, explained in Section 4.2.1, we could resolve the full 3D momentum space.

To achieve the full momentum reconstruction, we tried two approaches: staking neighbouring Brillouin zones, and a SED approach.

Brillouin zone stacking

First, we considered each of the 25 2D BZs resolved as representing a cut of the 3D BZ at different k_z.Each 2D zone was divided in 4 squares, and was assigned a k_z value, evaluated at the center of each square. These squares were combined with those diametrically opposite with respect to the center of momentum space Γ_0, reconstructing a slice representing the full BZ with the smallest possible variation of k_z. Stacking these slices resulted in the reconstruction of half the 3D BZ, which could be extended to the full k_x, k_y, k_z BZ by exploiting the mirror symmetry along the z-dimension.

Finally, the data cube is symmetrized following the crystal symmetries. As the crystal structure of $YbRh_2Si_2$ belongs to the I4/mmm group, 4-fold rotation and mirror symmetries can be applied in the xy plane, and mirror symmetry applies for the z axis. The resulting symmetrized array is plotted at a few selected binding energies in Figure 5.2.

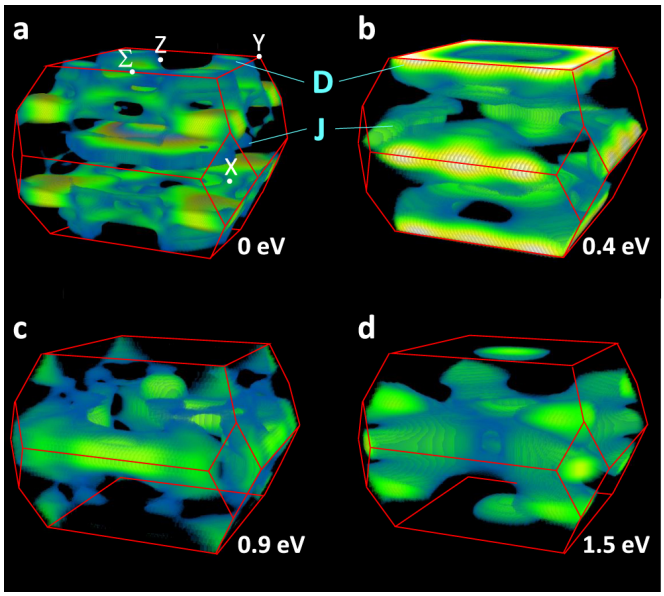

Figure 5.2: 3D momentum volumes taken at different constant energies. The Doughnut band D and the jungle jim band J can be identified in the energy cuts from the Fermi level (Fermi surface) down to 0.4 eV below. From Agustsson et al. [2].

Single Event Data frame approach

The second method is based on the same Single Event Data frame (SED) discussed in Chapters 3 and 4. The experimental setup used in these measurements is also equipped with DLD detectors. However, the data is only collected to a local PC by integrating the detected events into a rigid 3D array.

A SED can be built backwards from volumetric data by listing each voxel of the array as a table entry, with its coordinates in the original array as column values together with the value of the voxel itself. Binning (see Section 3.7) can then be performed by doing weigted binning. Here, instead of counting the number electrons found in the SED for each bin of the histogram array, the value of the weight is added.

Other than that, every other aspect remains the same. Calibrations can be performed on the SED level, even though the lack of electron resolved correction parameters will impose these corrections to be made on averaged values.

Operations such as reconstructing the perpendicular momentum are here much sim-

pler than the geometric approach presented above, as a simple mathematical formula relates perpendicular momentum to the detector coordinates, as described in Section 4.2.

The higher precision in the determination of the k_z values obtained by using this approach creates a sparse array in the k_z direction, which requires interpolation of the data after binning. Such an interpolation should always be applied after the symmetrization, and before any smoothing by Gaussian blurring.

5.2.4 Warping

A large momentum field of view, resolving 25 BZs makes each BZ relatively small in the detector image. This makes such measurements very sensitive to aberrations induced by the electron optics, and requires careful correction before any symmetrization or 3D momentum reconstruction method can be applied.

In order to align all BZs and ensure that they all have the same size, I developed a multi-perspective warping method based on selection of high symmetry points. The details of this method are described in Section 4.2.2(see also the resulting corrections in Figure 4.4).

5.3 Experimental Results

For tracking changes between large and small Fermi surfaces, the most decisive section of the BZ has been identified to be in the plane around the Z-point.[76,77] Panel a (and h) in Figure 5.3 shows a cut through the D (doughnut) sheet of the Fermi surface.

The high intensity at the corners originates from the pill-box band centered at the Γ-point. At the higher binding energy of $E_B = 0.4$ eV, depicted in panel b, the doughnut is almost circular, indicating that the band shrank below the $4f$-electron shell. This is in contrast to the expected behaviour for hole-like bands, which should show increased wave vectors with increasing binding energy. This character is however recovered as the band continues deeper in energy, as can be clearly observed in panel e and f. Below

1.5 eV a second band appears, also hole-like, centered at the Z-point.

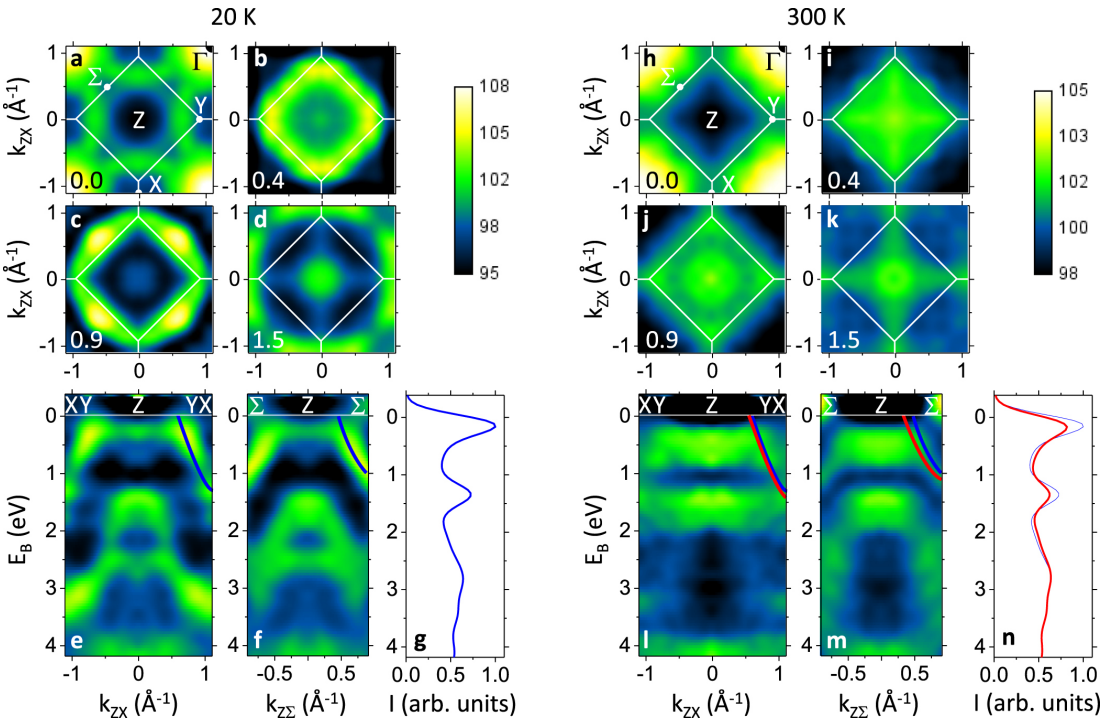

Figure 5.3: Comparison between the spectral density of electronic states at different energy-momenta cuts at high and low temperatures. The square panels show isoenergy cuts at different energies of the $Z-Y-\Sigma$ plane (top of 3D BZ) as the central diamond, while the corners cut through the $\Gamma-X-\Sigma$ plane, due to the BZstacking. The rectangular panels below show the energy-momentum dispersion along the $X-Z$ and $\Sigma-Z$ directions. These energy dispersion plots are normalized to the mean of each momentum cut. The integrated, non-corrected intensity is plotted in panels g and n. From Agustsson et al. [2].

The contrast emphasized by the color-code, visible in Figure 5.3, spans over a rather small range of the actual intensity variation of the images. The larger contribution to the signal is due to the quasi-elastic scattering of electrons with phonons, that results in electrons which almost conserve energy (small variations induce broadening in the features) and completely loose momentum information.

Furthermore, the two maxima in EDCs seen in panels g and n, which represent the momentum integrated EDC, correspond to the spin-split Yb 4*f* states. These peaks are suppressed in the energy dispersion plots (panel e,f,l and m) by normalizing each energy plane to the mean across momentum space, in order to emphasize the underlying band

structure.

5.3.1 Comparing 20 K with 300 K data

The high temperature plots shown in panels h through m, are affected by a stronger broadening induced by the Debye-Waller factor,[84] which increases background. The energy resolution of ≈ 100 meV is not sufficient here to resolve the Fermi surface directly, and therefore the doughnut shape is no longer visible, while the intensity at the Γ-point seems increased when compared to the low temperature data.

The cross-like shape the doughnut band shows at $E_B = 0.4$ eV reveals a substantial reduction in the D band wave vector along the $Z-\Sigma$ direction. Such a trend is confirmed when looking deeper at 0.9 eV, where the circular band at 20 K becomes a square at 300 K.

The D band at lower binding energies (see the energy dispersion plots, panels e,f,i and m in Figure 5.3) looks qualitatively similar at high and low temperatures. At higher temperature, this band appears to be shifted by 100 meV to higher binding energies, i.e. away from the Fermi energy. The bands below 1 eV appear unchanged, except for the stronger broadening at high temperatures.

Finally, a comparison of the momentum integrated EDCs shows no measurable energy shift of the Yb 4*f* states with our resolution, and just a slight reduction of the density of states close to the Fermi energy, in line with what previously observed by Kummer et al. [80].

Overall, the MDCs show a substantial shift of band D between 20 K and 300 K in the energy region between 0.4 eV and 1.1 eV. Therefore the momentum slice at a binding energy of 0.4 eV can be used to indirectly track at which temperature the change between the large and the small Fermi surface takes place.

5.3.2 Temperature dependence of the Fermi Surface

The cooling process with the cryostat used at P22 is rather slow, due to the large metal block being in thermal contact with the sample. Therefore, we were recordingh the data during the slow cooling from 300 K to 20 K. This data, while showing smallerSNR, is still sufficient to track the change of the size of the D band at 0.4 eV binding energy.

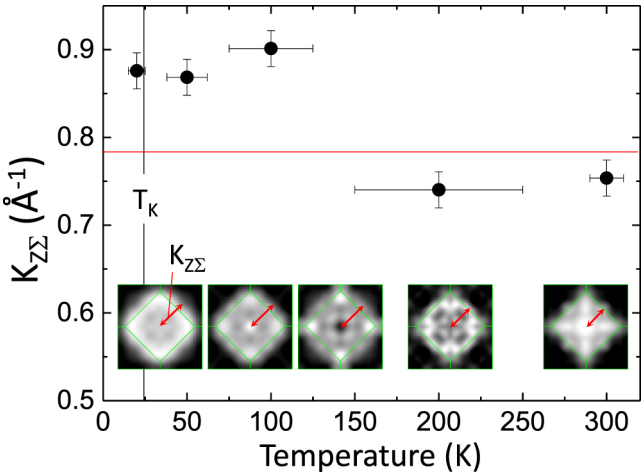

Figure 5.4: Temperature dependence of the width of the Fermi surface, indicating a transition from a large to a small fermi surface between 100 K and 200 K. The insets show the momentum slice at $E_B = 0.4$ eV, with the red arrow indicating the measured width, plotted above as dots. The large error bars originate from the change in temperature (see text) during the measurement of each data set. From Agustsson et al. [2].

In Figure 5.4 the width of the D band ring at 0.4 eV is plotted as a function of temperature. From this evaluation, we estimate the transition between a large and a small Fermi surface to take place at a temperature between 100 K and 200 K.

Concluding Remarks

This chapter presented the results of the HAXPES momentum microscopy measurements on the Kondo system $YbRh_2Si_2$. The main goal of this experiment was to track the temperature dependence of the Fermi surface, and identify where the transition between the so called small and large Fermi surfaces takes place. This is interesting as such changes arise from the hybridization of conduction electrons with the localized $4f$-electron states.

Also this helps to understand which of the underlying theoretical descriptions should be used, as Kondo theory originates from dilute impurity limit, while hybridization is a lattice effect.

However, the application of the technique itself is possibly even more interesting. By using high energy X-rays of over 5 keV as photon source, we were able to have a direct probe of the bulk states of $YbRh_2Si_2$. Such a probe can be used to study many classes of materials in which surface states are masking or modifying the underlying electronic structures, or to study buried surfaces or interfaces in layered materials.

Furthermore, the large field of view in momentum space, encompassing up to 25 Brillouin zones simultaneously, allows immediate full reconstruction of the 3D momentum space, making a 3D momentum microscope an effective 4D microscope, which records Energy and full momentum space simultaneously.

Finally, these data provided a great test case to develop momentum space unwarping techniques, based on multiple high symmetry points. Such a technique can be applied also to smaller FOVs, given that a few symmetry points are visible.

CHAPTER 6

PHOTO-DOPING OF La_2CuO_4

This chapter describes the work I did on photo-doping of high-T_c cuprate superconductors, specifically on the parent compound La_2CuO_4 (LCO). After a brief introduction to cuprates, I will describe the time-resolved momentum microscope measurements we performed on LCO, the parent compound of $La_{2-x}Sr_xCuO_4$ (LSCO). These experiments were performed at the HEXTOF end-station installed at FLASH, on both single crystals and thin films of LCO, as well as on a thin film of a slightly doped ($x = 0.02$) LSCO.

6.1 HIGH TEMPERATURE SUPERCONDUCTIVITY IN CUPRATES

After more than 30 years from the discovery of high temperature superconductivity in cuprates,[19] this class of materials still attracts great interest as the underlying mechanism of superconductivity and its interplay with competing orders is still unclear and strongly debated.[85–90]

In this work, we studied La_2CuO_4 (LCO), the parent compound of the La based cuprates $La_{2-x}Sr_xCuO_4$ (LSCO) and $La_{2-x}Ba_xCuO_4$ (LBCO). Historically, these were the first cuprates in which high-Tc superconductivity was detected.[19] Cuprates have

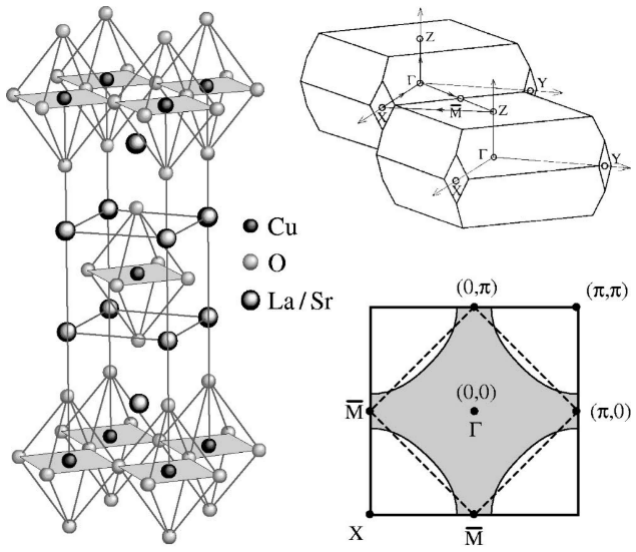

Figure 6.1: Crystal structure (left) of La_2CuO_4 / $La_{2-x}Sr_xCuO_4$ together with the reciprocal space representation of the Brillouin Zone and the expected Fermi surface (in the metallic state) in the $\Gamma X \bar{M}$ plane. Adapted from Damascelli, Hussain, and Shen [86].

Perovskite-like structured crystals composed of copper-oxide (CuO_2) planes spaced by 3D transition metal block layers (e.g. LaO). LCO and its doped variants, as well as $Pr_{2-x}Ce_xCuO_4$ or $Nd_{2-x}Ce_xCuO_{4-y}$, show the simplest of these structures (Figure 6.1), and are referred to as single-layer compounds. They consist of a single CuO_2 plane, interleaved with LaO planes formed by strong ionic bonds. Many other cuprates instead present more CuO_2 planes, like the bi-layer compounds $YBa_2Cu_3O_{7-y}$ (YBCO) or $Bi_2Sr_2CaCuO_{8+y}$ (Bi2212) or the tri-layer compounds such as $Bi_2Sr_2Ca_2Cu_3O_{10+\delta}$.

6.1.1 Phase Diagram

Whether it comes to electron or hole doping, all cuprates share qualitatively the same phase diagram. A simple sketch is presented in Figure 6.2.

The parent compounds of superconducting cuprates are characterized by an AFM Mott-insulator ground state. With increasing hole concentration, as in the case of LSCO when the La^{3+} ions are substituted with Sr^{2+} ions, loss of long-range magnetic ordering gives way to the superconducting dome. The so called optimal doping is at the

doping level where the superconducting dome is at its maximum, i.e. when T_c, the transition temperature of the superconducting phase, is the highest. When moving beyond into the overdoped region, the sample finally reaches a more or less metallic phase.

Electronic structure studies show the superconducting-gap has a d-wave symmetry.[91] Moreover, spectroscopic studies reveal the presence of a pseudogap in DOS at temperatures higher than the transition temperature T_c.[92]

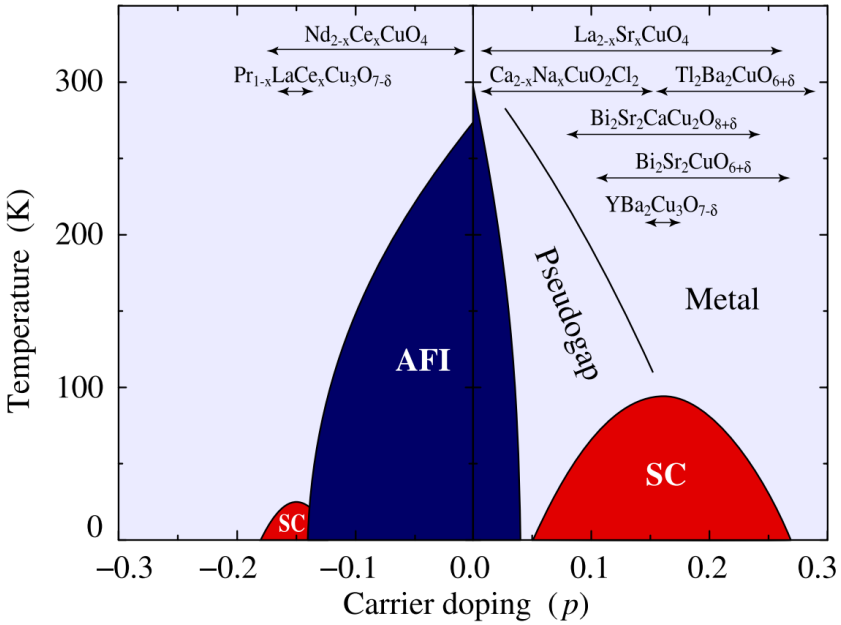

Figure 6.2: Doping-temperature phase diagram of cuprates, with electron ($p > 0$) and hole ($p < 0$) doping. On top, the range of doping accessible to different materials in the cuprate family. Adapted from Peets et al. [93].

Through the many years in which high temperature superconductivity has been studied with great effort, many different theoretical models have been proposed to answer one or the other phenomenological peculiarities of this exotic and elusive phase, but consensus is still lacking.

As opposed to conventional superconductors, which are in most cases Fermi-liquids which become superconducting due to electron-phonon coupling, as described in the BCS theory,[94] most of the models for high temperature superconductors such as *Res-*

onating valence bond,[95] *stripes* and *quantum criticalities*, although very different and sometimes contradicting, mostly agree on superconductivity arising not from the paired quasiparticles but from the pairing mechanism itself.[86] For further details about microscopic models for high T_c superconductivity we refer to Damascelli, Hussain, and Shen [86], Plakida [96], Micnas, Ranninger, and Robaszkiewicz [97], Kaldis, Liarokapis, and Müller [98], and Sigmund and Müller [99].

6.1.2 Electronic Structure

The electronic bands close to the Fermi level, which govern most of the electronic properties in these materials, are formed by Cu 3*d* and O 2*p* orbitals from the CuO_2 planes. A schematic representation of the crystal field splitting and hybridization of these states, forming the CuO bands, is shown in Figure 6.3, next to the momentum integrated EDC of optimally doped (superconducting) LSCO measured with ARPES.

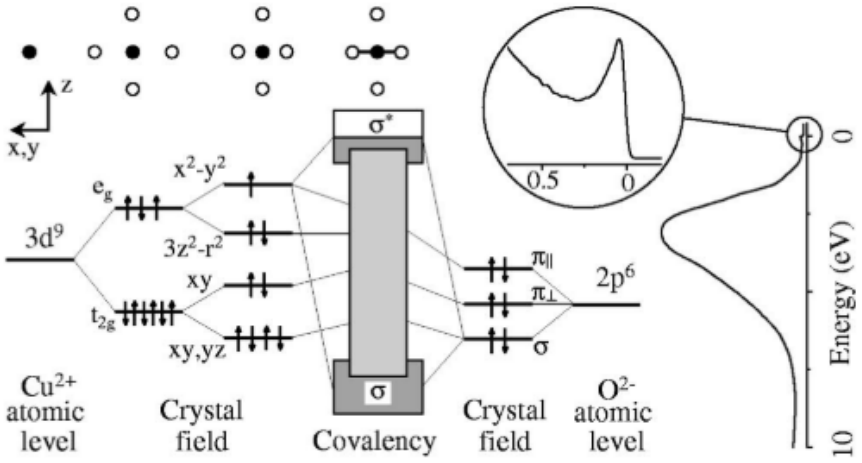

Figure 6.3: Crystal field splitting and hybridization of Cu 3*d* and O 2*p* states which form the electronic structure of the low binding energy region. The right vertical plot shows an EDC formed by these states measured by ARPES. Adapted from Damascelli, Hussain, and Shen [86]

From a Local-Density Approximation (LDA) calculations perspective, the parent compounds of cuprate high T_c superconductors are expected to be metallic, as represented in panel a of Figure 6.4. However, the ground state is instead an (antiferromagnetic) insulator. This discrepancy arises from the single particle assumptions, which fail in the

presence of strong electron correlations.

The *Mott-Hubbard* model[100–102] was proposed to understand cuprates. In these systems the large on-site electron-electron repulsion U leads to a splitting of the Cu $3d$ bands in the Upper Hubbard Band (UHB) and Lower Hubbard Band (LHB) (Figure 6.4 b). Moreover, the Cu-O charge transfer energy Δ is smaller than the Coulomb repulsion U, making cuprates *charge-transfer insulators* (Figure 6.4 c). The minimum model is a three-band extended Hubbard model, with explicit inclusion of Cu $3d_{x^2-y^2}$ as well as O $2p_x$ and O $2p_y$ orbitals.

However, these materials are often still described as effective Mott insulators, where the LHB is substituted by the *Zhang-Rice singlet* band,[103] born out of the localization of a strongly bound hole on the central Cu ion in an oxygen plaquette (Figure 6.4 d). This leads to an effective Mott gap of the order of the charge-transfer gap Δ.[86]

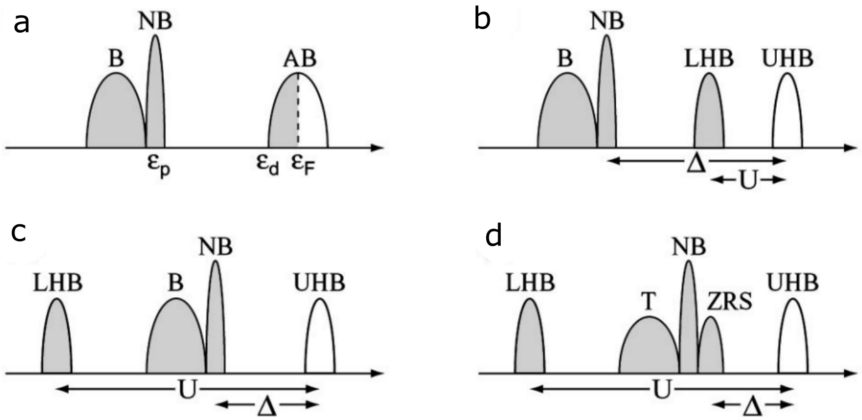

Figure 6.4: Effect of strong correlations described by the Hubbard model. (a): metallic band structure. (b) simple Hubbard model. (c) small charge-transfer gap, and (d) formation of Zhang-Rice singlet band. Adapted from Damascelli, Hussain, and Shen [86].

6.1.3 Low Energy Excitations

A question which still remains unanswered, is what happens to the low energy states in the low-doping regime. Is the chemical potential shifted downwards towards the top of the Valence Band (VB) (panel (c) of Figure 6.5), or is it pinned at the mid-gap, leading

to the formation of an in-gap state (panel (b) of Figure 6.5)?

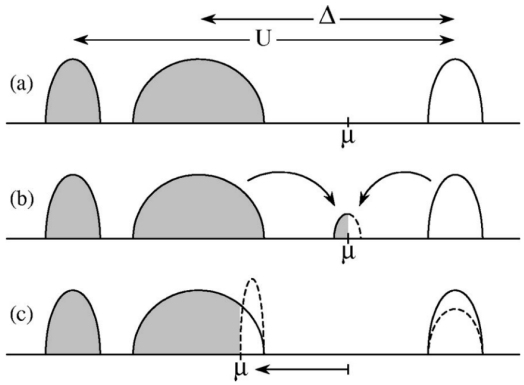

Figure 6.5: Effect of doping in a Mott-Hubbard insulator. Panel (a) shows the Mott-insulating ground state. Panel (b) shows the formation of in-gap states at the Fermi level, generating new states which host conductivity when reaching metallicity at higher doping, and superconductivity. Panel (c) depicts the scenario where the chemical potential shifts to the VB, where conductivity will take place, and leading to a transfer of spectral weight from the CB to the VB. Adapted from Damascelli, Hussain, and Shen [86] and Van Veenendaal, Sawatzky, and Groen [104].

Optical conductivity measurements (see Figure 6.6) show, upon doping, a shift of spectral weight from the charge transfer region into a broad Mid-InfraRed (MIR) peak, both in electron and hole doped systems,[105] together with, at higher doping, a sharp free carrier Drude-like peak centered at $\omega = 0$. As doping increases the MIR spectral weight shifts towards lower energies and finally merges into the free carrier peak when the optimal doping level for superconductivity is reached.

Several models have been proposed to account for the MIR absorption, ranging from incoherent motion of doped carriers against the background of AFM spin fluctuations,[106,107] optical transitions involving doping-induced in-gap[108] and Zhang-Rice singlet states,[109] polaronic effects,[110–112] the interplay between the strong correlations and strong electron-phonon interaction (Hollstein-Hubbard model).[113] Although there is yet no agreement on the origin of this MIR peak, better understanding of its origin would certainly bring closer to understanding high Tc superconductivity.

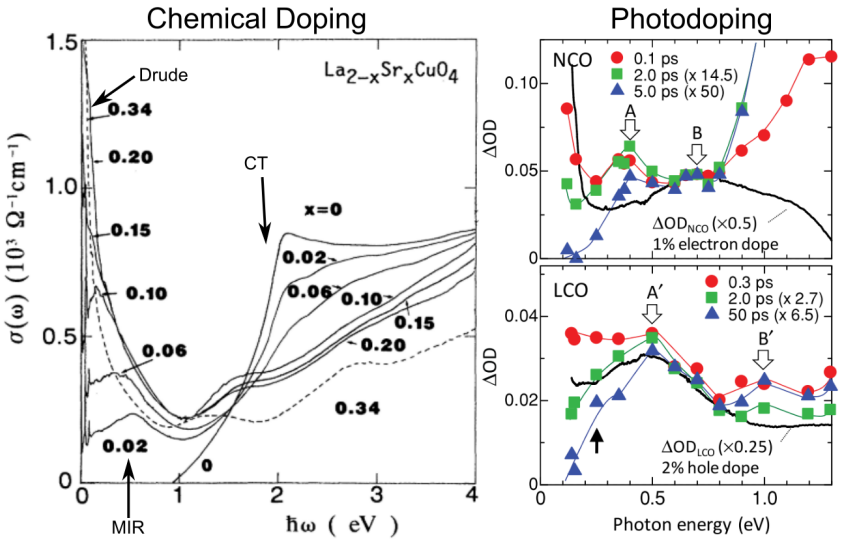

Figure 6.6: Changes in optical conductivity induced by doping. Left is the result of chemical doping, adapted from Uchida et al. [105]. The right panels shown instead the photoinduced changes of the optical conductivity at different time delays from the optical excitation in LCO and NCO, adapted from Okamoto et al. [3].

6.1.4 Photodoping

The most common doping technique consists of substituting one atom with another element with the same orbital structure but a different number of valence electrons. This process is commonly referred to as chemical doping, and can be either electron- or hole-doping, depending on whether the substitute ion has more or less electrons than the original ion.

A similar redistribution of charges can also be obtained through photoexcitation of electrons across the gap, leaving behind a hole. Eventually these holes might form long-lived defect states such as polarons, bipolarons and solitons.[114] These quasiparticles effectively transiently dope the material, inducing phases which are normally achieved by chemical doping.

A surprising similarity in the changes in optical conductivity between chemical doping and photo-doping experiments was observed when studying La_2CuO_4.[114] Here, by exciting electrons across the charge-transfer gap, a MIR peak appears, similar to what is

observed upon weak chemical doping.[3,115,116] It is to be noted however, that photodoping is generating both electrons and holes, and can be interpreted as simultaneous electron and hole doping. This could lead to the formation of two in-gap states, which might however be indistinguishable one from the other.

Such a similarity between photo- and chemical doping allows to study the low doping phases in the transient optically excited regime, by means of ultrafast optical techniques. In Figure 6.6 the parallelism between the effects of chemical doping[105] and optically induced changes in the optical conductivity[115] show remarkable similarities.

However, transient features resembling chemical doping can be attributed to a number of different microscopic origins, due to the two-particle nature of all optical experiments. This motivated us to perform the same photodoping experiments, using photoemission spectroscopy as a probe instead, as this might allow us to detect from where, in energy and momentum these excitations originate.

6.2 Samples

In our time resolved momentum microscopy experiments at FLASH we studied photodoping in LCO and LSCO by measuring both single crystalline and thin film samples.

6.2.1 Single Crystals

The single crystals we measured were prepared from a rod-like sample, grown by the floating-zone method.[117] In order to assert the correct crystal orientation, with the c-axis along the long dimension of the sticks, Laue measurements were performed. All crystals we measured showed excellent alignment along the c-axis, as can be seen in Figure 6.7.

Photoemission measurements are highly surface sensitive. In order to ensure the best measuring conditions, most materials require a *fresh* surface to be prepared in-situ just before the measurement. Such care was required as the samples needed to be cleaved

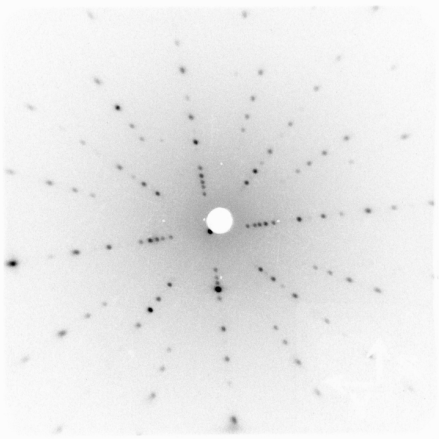

Figure 6.7: A Laue image obtained from a rod shaped single crystal La_2CuO_4 sample, showing the alignment of the top face along the a-b crystal plane. The alignment was prepared in the Laboratories of C. Krellner.

in vacuum prior to measurements. Layered 2D materials, as well as some cuprates such as Bi2212 are easy to cleave, as it can be performed using adhesive tape. LCO and its doped variants have instead a strong 3D character. Thus, there is no preferential plane where the crystal can *break*, to produce a clean flat surface, making the cleaving process not trivial.

The reason why we chose to study LCO and not, for example, Bi2212, is that the latter does not exist in the Mott insulating form which we aim to study. We tested 2 different approaches to cleave such hard crystals.

Rod cleaving

First, small platelets, of $1 \times 1 \times 0.5$ mm were cut out of the main rod using a wire cutter. The shorter side was along the crystalline c-axis. These were glued on the sample holder using silver-epoxy glue. Finally, a ceramic rod was glued on the top surface of the sample. We attempted to cleave the sample by applying force on the ceramic rod in vacuum. However, the LCO samples cut in this geometry proved stronger than the glue, and all cleaving attempts resulted in fractures in the glue instead of in the sample itself.

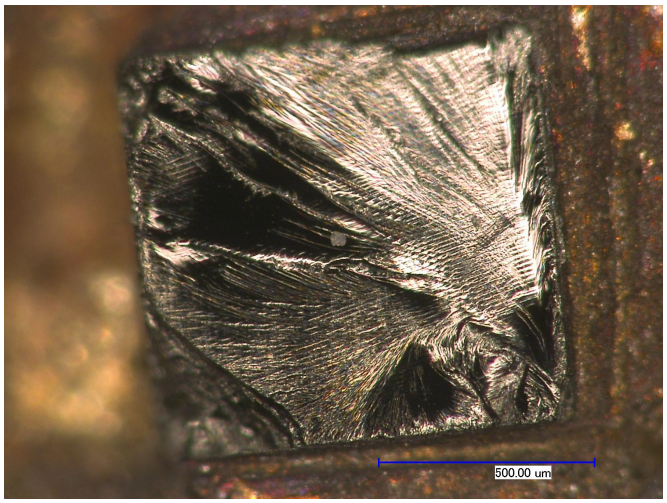

Figure 6.8: Single Crystal of LCO after pincer cleaving. Image taken with an optical microscope after measurements.

Pincer cleaving

A second approach was to cut the crystals into rod shaped higher sticks, namely $1 \times 1 \times 4$ mm, again using the wire cutter, with the long dimension along the crystalline c-axis. These sticks were then glued on a flag style sample plate. A round metal plate, with a 1.1 mm hole in the center was glued on the plate. The sample was glued in the hole of the round plate, to ensure mechanical stability along the direction parallel to the plate surface. A small dent was also cut on the side of the sample rod, to facilitate a breaking point at mid-height of the sample.

Using this second technique for cleaving proved to be more successful. This was done by squeezing the sides of the sample, where the dent was cut, using mechanical pincers.

The build-up of SC effects made some cleaves unstable due to the roughness of the resulting surface. An example of one of the successful cleaves in shown in Figure 6.8, which shows a photograph of the surface after cleaving. Even though the surface was not flat, it was possible to identify a small region where the surface quality was good enough to measure the EDCs shown in Figure 6.9 and 6.10.

6.2.2 Thin Films

As cleaving such hard samples has proven to be challenging, we considered and applied another approach. Instead of cutting single crystals, we relied on the growth of epitaxial thin films on a substrate. These films were grown on $LaSrAlO_4$ (001) substrates using layer-by-layer oxide molecular beam epitaxy.[118]

One of the main difficulties that arises with thin films is how to ensure that a clean surface is available for measurements. As these can obviously not be cleaved, the surface can be *renewed* by annealing or heating methods. However, flashing (heating) the surface can lead to thermal expansion mismatch or even changes in the chemical environment at the surface.

Selenium capping

We instead took a different approach. We protected the thin film surface by coating it with a 50 nm think layer of Se. Such a technique had proven successful in previous work on Pr_2CuO_4.[119] The Se layer is deposited on the film in vacuum, right after growth. This should be sufficient to protect the surface for transport between the growth chamber to the experimental chamber. The deposited Selenium layer can then be removed by annealing at temperatures higher than the evaporation temperature of Se of 170 °C.

However, first test showed that after contact with air, the Se layer had oxidised, forming SeO which evaporates at much higher temperature than Se. This can strongly affect the decapping process, as the evaporation temperature of SeO is above 500 °C, much higher than Se. Annealing at such high temperatures is most likely to damage the underlying LCO surface, by creating oxygen vacancies and changing the chemical and, in turn, electronic structure of the surface layer.

Transport of films using the UHV suitcase

In order to avoid formation of SeO we transported the samples from the growth facility to FLASH using a vacuum suitcase. As the samples were grown on plates not compatible with the measurement machine, a transfer from the growth plate to the flag style sam-

ple plate was required. In order to avoid air contact in this step, we built a glove-box around the exit port of the sample growth chamber and the vacuum suitcase, made of transparent plastic sheets. This glove box was then filled and purged with Nitrogen to remove all residual air. Once the sample transfer gate of the growth chamber was open, a steady flow of nitrogen was blown through it into the glove box. A vacuum pump, controlled by a needle valve placed behind the vacuum suitcase pumps, was used to pull out the excess nitrogen, to ensure the glove-box would not over-inflate.

By using the two *gloves* built in the glove bag, the samples were removed from their original plates and cleaned from the residuals of $SrRhO_3$ powder which was used as absorber when heating the substrate during growth. The samples were then mounted on the experimental sample holders (see Appendix A) and finally mounted in the sample cartridge and loaded in the vacuum suitcase. Finally, the vacuum suitcase was pumped over night to ensure a pressure lower than 10^{-8} mbar, in order to be ready for transport.

Before the experiment, the vacuum suitcase was bolted to the preparation chamber, from which the sample holders could be transferred to the experiments cartridge and in turn to the microscope. With this technique, we were able to successfully transfer 4 films of LCO and 2 films of LSCO with 2% doping.

Capping removal

The annealing process used to remove the Se capping on the thin film was performed in situ, by heating the sample holder, in thermal contact with the sample, to 260 °C for two cycles of 30 minutes, and finally another 30 minutes at 310 °C. The evolution of the decapping process was monitored by performing XPS measurements in between all cycles. The measured spectra are plotted in Figure 6.9. Here, the Se 4 d core level peaks are visible in the left panel, plotted on a log-scale to compare the strong signal from the capped samples to the residual after the annealing process. For comparison, also the XPS signal from a single crystal is plotted, which shows (of course) no trace of Se, unequivocally identifying those peaks to the Se core levels.

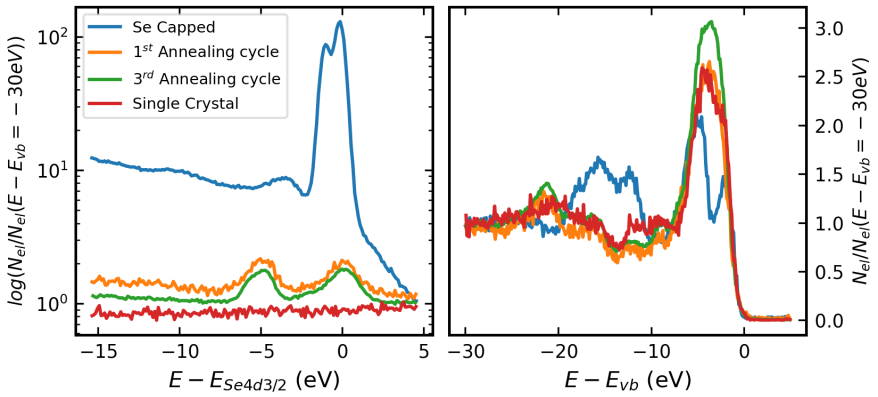

Figure 6.9: EDCs obtained with XPS measurements @ 165 eV with HEXTOF. The different curves show the changes induced by multiple annealing processes on the Se-capped LCO thin films. Prominent Se 4d core level peaks are shown in the left panel,which disappear after the first 30 minutes annealing process at 260 °C (note the log-scale in the left panel). Further annealing a second cycle at the same parameters showed no change (not plotted). A third annealing process, at 310 °C for 30 minutes showed only a marginal change, with slight relative increase of spectral weight at the top of the VB region (right panel), compared to the Se core levels region(left panel). A qualitative change in the VB region is clearly visible in the right panel. For comparison, the EDC obtained from a LCO single-crystal is plotted in red. All EDCs are normalized to the integral count in the energy region $-50\ \text{eV} < E - E_{vb} < -30\ \text{eV}$.

Furthermore, the VB region is plotted in the right panel of Figure 6.9. A strong qualitative change of the electronic states in this region shows the difference between a pure Se signal, contaminated with dirt from transport and the signal from LCO, after decapping. The de-capped LCO signal is in good agreement with the signal observed from the single-crystals, confirming the removal of Se was successful.

6.3 Experimental Results

In our measurements performed with HEXTOF at FLASH we investigated the time-dependence of the electron energy and momentum distributions on different LCO and LSCO thin films and single crystals.

In our photodoping experiments on LCO, we do not have an *a-priori* expectation of where the excitations we are aiming to study might appear. As a matter of fact, the scope of these measurements was to determine where, in energy but also eventually

in momentum-space, does the shift in spectral weight originate from in the electronic structure of these crystals? Indeed the large FOV, able to cover an entire BZ or more with a wide energy window offered by a momentum microscope is the reason we chose such a setup for this experiment.

Here I will present the results obtained on three specific samples, to which most of the acquisition time was dedicated. These are two thin films, of LCO and LSCO and an LCO single crystal.

6.3.1 Energy distribution curves

To try to understand the data we obtained, we start by analyzing the VB region of the EDC, looking only at the unpumped electrons, i.e. the electrons which were detected with no pump laser.

These EDCs are plotted in Figure 6.10 for the three samples. An immediate difference between the three can be seen in the 5 eV range below the top of the VB, where the LCO single crystal shows a double-peak structure, as opposed to the single-peak of the two thin films. These however are not two distinct peaks, as they are formed by a multitude of bands, strongly broadened, as is typical in highly correlated electron systems.

In the previous work from the late '80s, when much attention was dedicated to cuprates as the novel class of high temperature superconductors, it has been shown that these two-peak structures originate from the Cu $3d$ and O $2p$ states,[120] and are common across the whole cuprate family.

The difference between the single crystal and the thin film EDCs in this region, observed in our data, might be attributed to different surface terminations. In thin films, the termination is well defined, as the entire film is grown uniformly and will always present, in the case of LCO and its doped variants, a CuO layer on the top.[118] The single crystal is instead cleaved in-situ and results, in La based cuprates, in rather rough cuts along arbitrary crystal directions, as these crystals do not present a preferential cleaving

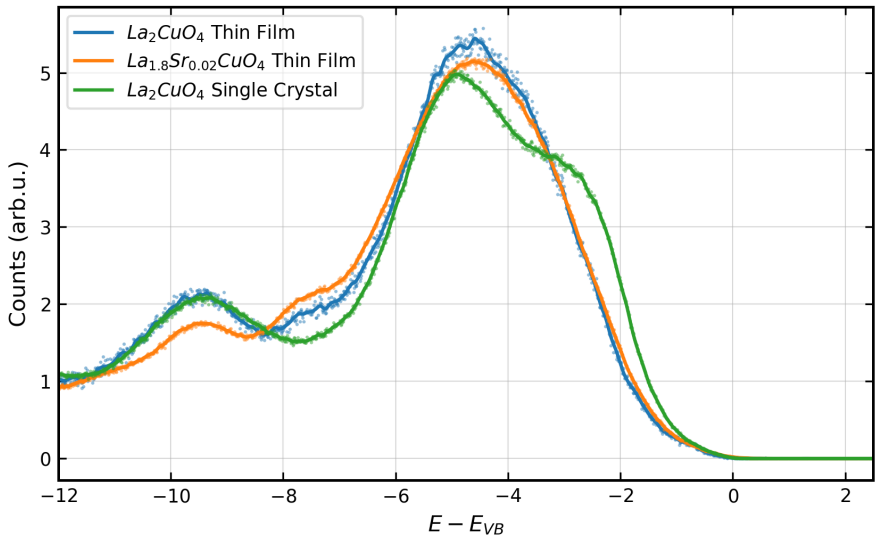

Figure 6.10: Comparison of the VB region of the EDCs of the three samples measured with a photon energy of 55 eV. These curves were obtained evaluating only the electrons detected with no pump laser, i.e. the "unpumped" electrons. The curves are all normalized to the total number of detected electrons.

plane. The cleaving process we used, described in Section 6.2.1, forced cleaving roughly along the a-b plane.

No distinct Fermi edge could be detected in the low doping LSCO sample. This is due to the low doping level, combined with a relatively large broadening induced by space-charge and the limited energy resolution.

6.3.2 The −9.5 eV peak

A peak at around −9.5 eV was often observed in early photoemission experiments on cuprates, and most studies claim it originates from surface contamination.[85,121] It has been shown to be related to the excess oxygen concentration on the surface, showing an anti-correlation to the 2 eV region below the Fermi level when annealing in Ultra-High Vacuum (UHV) to deliberately reduce the oxygen concentration at the surface. A relation to carbon content has also been argued,[120] further supporting its relation to surface contamination.

In this work, this −9.5 eV peak has been used as a means of correcting the energy

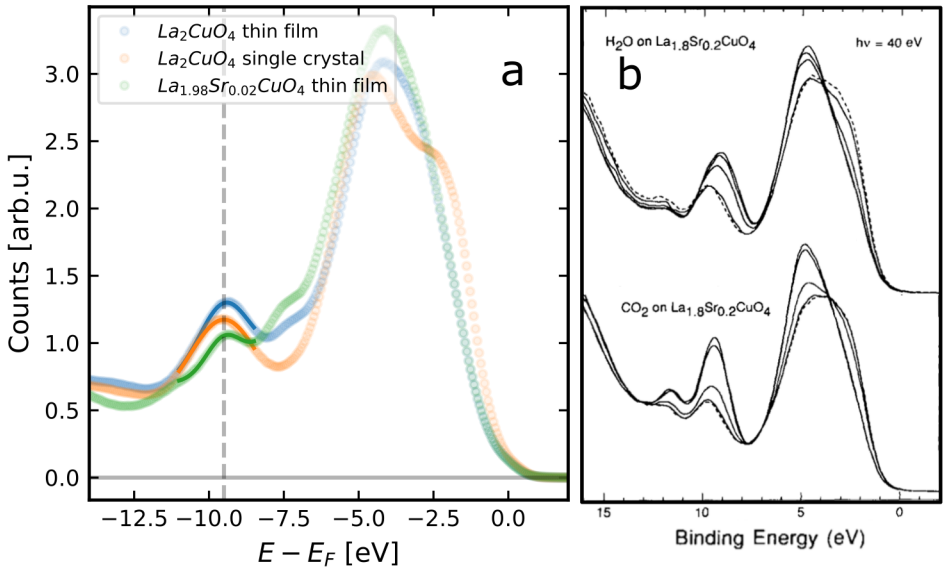

Figure 6.11: Comparison of the momentum integrated static EDCs of the three samples measured (left panel) with the results of Kurtz et al. [121] (right panel, adapted from their work), where the samples were exposed to H_2O and CO_2, showing an increase of the spectral weight in the −9.5 eV peak. This peak is therefore an indication of surface contamination but could be exploited for energy alignment.

offset in the energy calibration. All EDC alignment methods (see Section 4.1.5) were performed fitting a Gaussian to this feature and forcing its center to −9.5 eV, as shown in Figure 6.11.

6.3.3 Momentum integrated dynamics

As the scope of the experiment was to observe the time evolution of the electronic states upon excitation on the sub-picosecond time scale, we selected a time window around time zero t_0 (see Section 4.3.1) of about 2 ps. The effective resulting time window is however smaller, as drifts in timing synchronization leads to shift in the position of t_0, resulting in a consistently measured time window of 1.2 ps. A larger time window could also be studied, but the changes of the noise floor make interpretation of the data outside the 1.2 ps window unreliable.

Anyhow, this time window is still sufficient to investigate the time scale of interest, as from our previous optics measurements[4] the main dynamics were observed on the

sub-picosecond time scale.

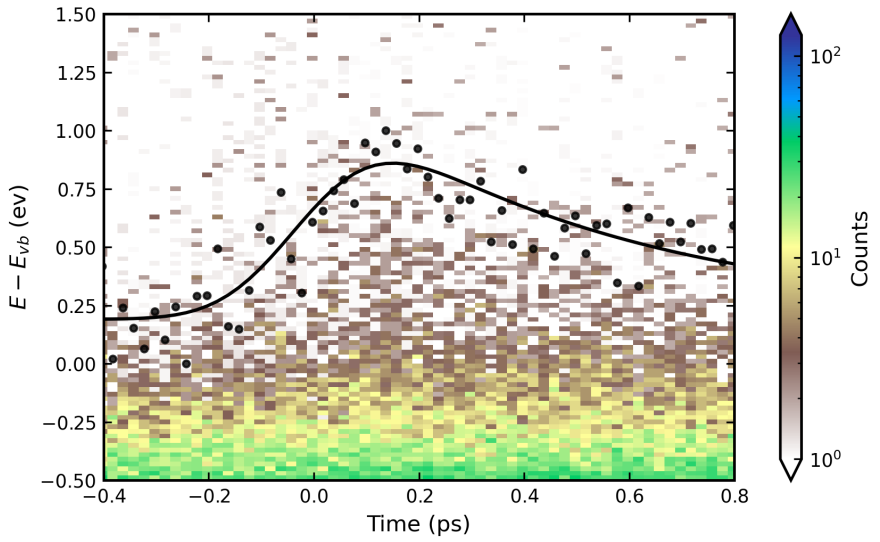

Figure 6.12: Logarithmic false-color plot of the time-resolved momentum-integrated dynamics of the EDC at the top of the valence band. The pump-induced electrons detected above the top of the valence band are plotted as black dots. A fit to these data was performed with the model described by Equation 6.1. See text for further details.

We observed photoexcited electrons in a < 1 eV range above the top of the VB, appearing upon optical excitation. The transient changes have a resolution limited rise time and a slower decay. Such dynamics are plotted in Figure 6.12, where the logarithm of the number of photoelectrons is plotted as a function of pump-probe delay and energy in a false-color-plot. The log-scale is necessary to show the time-resolved signal, as the total number of electrons plotted here above the VB, is ≈ 6 orders of magnitude smaller than the average electronic density in the VB region.

The black curve is a fit to the integral of the number of electrons detected above the top of the VB, plotted as black dots. The function used to fit the data is a single exponential decay multiplied by the step function, convoluted with a Gaussian to account for the duration of the excitation pulse. The analytical solution of a simple 3 level system, as described in supplementary information of Eichberger et al. [122], can be written as

$$I(t) = \frac{I_0}{2} e^{\frac{\sigma^2}{16ln2\tau^2}} \left[1 - erf\left(\frac{\sigma^2 - 8ln2 \cdot \tau \cdot t}{4\sqrt{ln2} \cdot \sigma \cdot \tau} \right) \right] e^{-\frac{t}{\tau}} \tag{6.1}$$

where $I(t)$ and I represent the dynamic and unpumped signals respectively, *erf* is the error function, τ is the exponential decay constant and σ is the FWHM of the pump pulse time profile. This trace is further convoluted with another Gaussian which accounts for the finite X-ray probe pulse duration.

The time scale of the relaxation process evaluated through this fit is around 500 fs, with pump and probe pulses evaluated at $\approx$ 150 fs (FWHM). This is in good agreement with the time scales observed in all-optical measurements[3,4,115].

Figure 6.13 shows the same analysis performed on the three different samples: an LCO thin film, a single crystal of LCO and a weakly doped LSCO thin film. The similar time scales and energy range in the pump-induced changes on all three samples confirms the observed signal to be originating from electron dynamics in the sample, and not from SC effects or other experimental artifacts. The data acquired on the LSCO sample however did not achieve sufficient SNR to resolve the dynamics through the fit.

The analysis on the three samples was done independently, but following the same procedures. For each sample, the optimal calibration and correction parameters were first evaluated independently, and later used to apply the corrections on each SED. The data for each sample were recorded over 16 to 20 hours, through different experimental runs. All drifts and manual changes to the experimental settings throughout these measurements were automatically corrected by using parameters stored together with the data. Also the fitting of the dynamics shown in Figure 6.13 was performed using the same initial parameters. The methods and details about these procedures were discussed at length in Chapter 4.

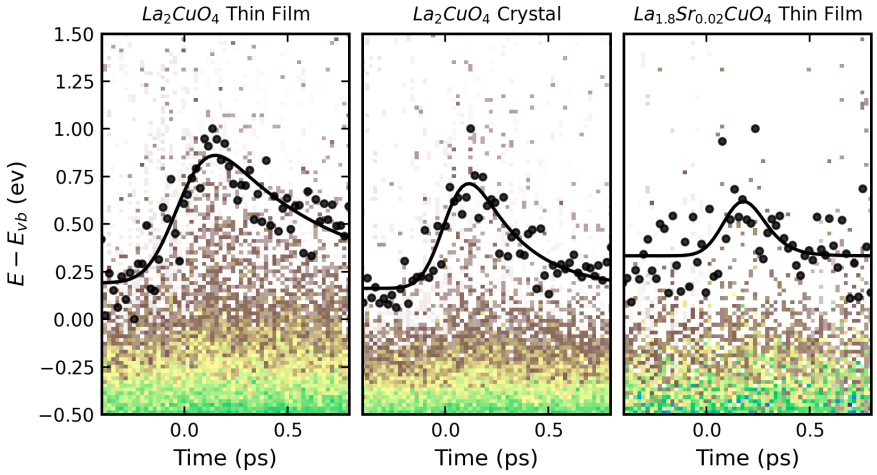

Figure 6.13: Comparison of the time-resolved momentum integrated EDC at the top of the valence band for the three samples measured. The qualitative similarity in the dynamics rules out experimental artifacts as their origin. However the low signal-to-noise ratio in the LSCO data (right-most panel) was not sufficient for a successful fit.

6.3.4 Discussion

A clear change in time-scale of the photoexcited electron states can be observed when examining how the time-resolved traces evolve with increasing energy above the top of the VB. Shortly after t_0, electrons are detected until just below 1 eV above the VB. With increasing time-delay, the excited electrons show increasing decay times as they approach the VB.

The highest energy, where photoexcited electrons are observed, being below 1 eV rules out a semiconductor-like behaviour of this system. Here, the 3.1 eV excitation photons of the pump would excite electrons above the optical gap of 2 eV (see figure 6.6) and excite electrons directly into the CB.

Transport measurements have reported an indirect gap of only 0.89 eV.[123] The time resolution of $\approx$ 150 fs would not be able to resolve the fast electronic decay from the direct optical transition to the bottom of the CB. In any case, a longer lifetime of the electrons would be expected after relaxing into the pocket at the bottom of the CB. These are however not observed in our data, where the highest photoexcited electrons

we clearly observe are still less than 1 eV above the VB.

The dynamics observed in our data suggest a scenario in which new states are formed inside the gap, near the Fermi level, as depicted in panel (b) of Figure 6.5. Mid-gap states would be centered at ≈ 450 meV above the VB. There is no evident signature of any gap in our data, which can however be caused by low signal to noise and an energy resolution of ≈ 150 meV, which we expect from the experimental conditions.

Such a picture is in contrast with the conclusions of Van Veenendaal, Sawatzky, and Groen [104], which suggested shift of the chemical potential towards the VB. Their conclusion was, however, supported by the doping induced shift observed in the core level spectra of Bi2212. As the relative energy of the core levels from the Fermi level does not change, a shift in the Fermi energy would induce a shift in the core level spectra as well. In LCO, however, core level studies[1] have shown no shift in the core levels upon doping, which supports our observation of the formation of in-gap states, not for all cuprates, but for the LCO in particular.

6.3.5 Fluence Dependence

In all-optical pump-probe measurements, the recorded changes in optical properties can often have multiple possible interpretations. Therefore most experiments also vary one or more of the other parameters to observe how the changes vary across the sample temperature, or excitation laser fluence, for example.

The changes we recorded with our trMM experiments showed a weak pump-induced signal, which was not sufficient for a high contrast momentum differential analysis. One of the reasons for such small signals can be attributed to the instability of the optical pump laser, as is plotted and described in Section 4.4.3 and Figure 4.11. This led to most of the data to be pumped with a fluence less than 0.2 mJ/cm^2, over an order of magnitude smaller than the set fluence, which was aimed for in this experiment. As a comparison, similar photodoping measurements performed with all-optical pump-probe measurements showed only a small transient signal in this fluence range. Effects

comparable to 15% chemical doping required instead fluences in the 10 mJ/cm^2 range.[4] In such a weak perturbation regime, it is therefore expected to observe a weak pump-induced signal.

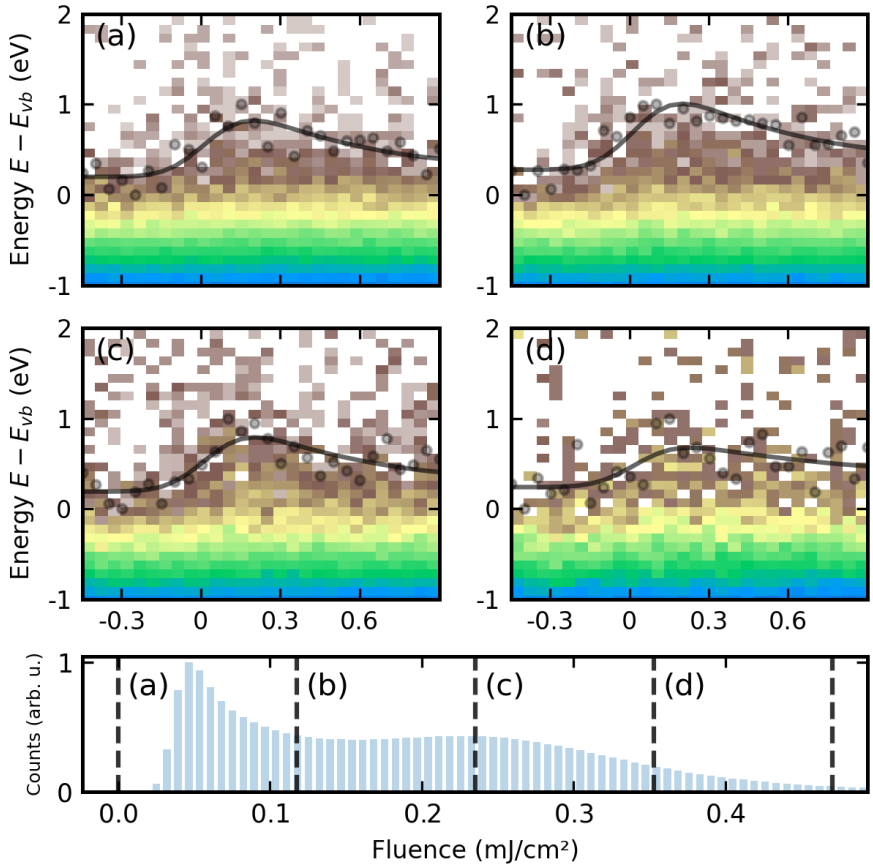

Figure 6.14: Fluence dependence of the dynamics induced in the electronic structure of LCO, obtained by exploiting laser intensity variation. Panels a-d show the pump induced changes as false-color-plot at different fluences, corresponding to the regions indicated in the bottom panel. The black lines are a fit to the data above the top of the valence band (see text for details). The bottom panel shows the distribution of photoelectrons detected at different pump fluences, normalized to its maximum.

However, by taking advantage of the electron-resolved data frames, we could exploit these laser fluctuations to evaluate the fluence dependence across a limited range of fluences. The results are shown in Figure 6.14, where panels (a)-(d) show the EDCs as a function of pump-probe delay at increasing fluences. The black lines show the fit to these data of the function described in equation 6.1. The distribution of electrons,

detected as a function of pump fluence, is plotted in the panel below. Here, the dashed lines indicate the regions used to select the data plotted in the panels (a)-(d) above.

Throughout the entire fluence range, the signal appears similar both in energy range as well as in time-scale. The fit was performed leaving as free parameters only the exponential decay constant τ, and the width of the convoluting gaussian σ, to account for changes in SC-induced broadening. The value obtained for τ appears to decrease by 10% across a fluence range spanning half an order of magnitude, while σ does not show a measurable change. This rules out SC to be the cause of the transient signal observed, as the SC shift in energy would be linearly increasing with increasing pump fluence.

6.3.6 Momentum distributions

All the results presented so far were obtained integrating over the entire momentum space in our FOV. The weak time resolved signals observed, leave little hope to observe momentum-resolved dynamics.

However, we could identify dispersions in the top of the valence band, which are common to all three samples. These resemble the electron-pockets observed in the (π,π) points in previous works of Wei et al. [124], Ino et al. [125, 126], and Yoshida et al. [127].

The top of the valence band of the three studied samples is presented in Figure 6.15. The signal plotted here is 4-fold symmetrized, with both rotation and inversion symmetry, following the symmetry of the crystal structure (I4/mmm group). Furthermore, smoothing by convolution with a Gaussian kernel was used as a low-pass filter, to boost SNR.

The reason why most of the signal is in the outer rim of the FOV, is because the matrix elements of 55 eV photons amplify signals from the second BZ and suppress those from the first. This leads to a dark square at the center (1^{st} BZ) surrounded by the borders of the 2^{nd} BZ.

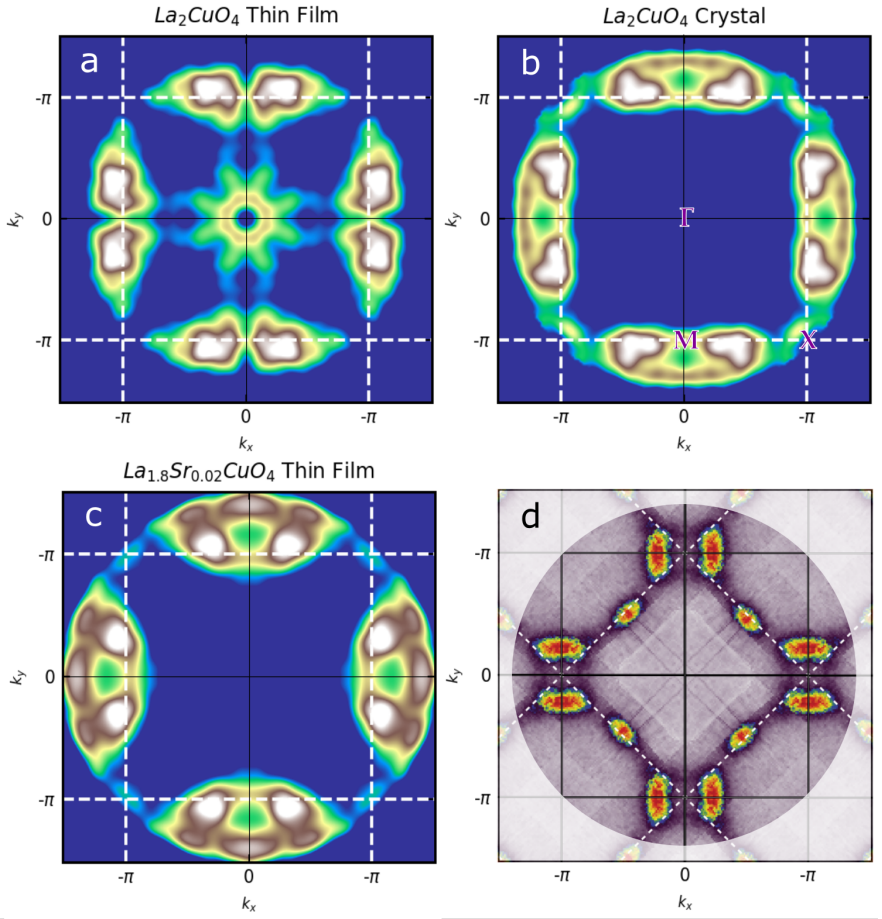

Figure 6.15: Momentum dispersion, taken at the top of the valence band $E = E_{VB}$. Panels a,b and c show the data obtained at FLASH on the three studied samples, while panel d shows the fermi surface of electron-doped LCO, measured by Wei et al. [124]. Matrix elements of the 55 eV photons suppress signals from the 1st BZ resulting in the dark areas in the center. The resulting pockets from the 2nd BZ are in good agreement with previous results shown in panel d.

The exception posed by the LCO thin film data, with the intensity visible in the center the BZ, is to be attributed to a pronounced space-charge effect. Even though partially corrected for, this still "lifts" signal in the center of the detector from the lower kinetic energies. Furthermore, a detector artifact, arising from the overlap of the DLD meanders (see sections 2.3.1 and 4.4.5), induces fake-electron counts in the center of the detector throughout the entire time-of-flight range. This effect is usually small, but contributes with the space-charge, to create the artificial pattern in the center of panel a in Figure 6.15.

An attempt was made to study the momentum resolved dynamics. It turns out that the time-resolved signal, plotted in Figure 6.12 and 6.13 originates almost entirely from the border regions. However, these dynamics cannot be directly attributed to be originating in a specific high symmetry point, as the majority of the detected electrons originate from this region (due to the matrix elements discussed above).

Concluding remarks

In this chapter I reported the results and current status of the analysis of our time-resolved momentum microscopy measurements on LCO. The aim of these photodoping experiments was to observe where, in energy-momentum space, electrons forming a MIR peak visible in all-optical pump probe measurements reside. The main challenges were posed by photoemission experiments on high-correlated electron systems such as LCO, which result in strong broadening of band structure features, together with broadening induced by space-charge effects.

This data resulted in a small yet visible pump-induced electron redistribution, with energy- and time-scales in good agreement with the results observed in all-optical pump-probe measurements.

The energy distribution of the photoexcited electrons suggests the formation of in-gap states as the most probable scenario for LCO, in contrast to other cuprates like Bi2212.[104]

This is supported by the indirect measurements of core-level shifts which show a shift in binding energy of the core levels of Bi2212[104] and YBCO, while record no change in LCO.[1]

These results are however still preliminary, as the data we recorded can be analysed in further detail, and maybe shed more light on the photodoping process in LCO cuprates.

CHAPTER 7

Conclusions

In this Thesis I have presented the development of an innovative data processing workflow for multidimensional momentum microscopy, exemplified through two experiments which were made possible by it. The relevance of such tools is not, however, limited to the scientific cases discussed in this thesis, but has positively affected the work of all the many experiments performed with the High Energy X-ray Time of Flight (HEXTOF) end station at Free-electron -LASer in Hamburg (FLASH), as well as other momentum microscopes, which chose to implement our approach.

After a brief introduction to the technique of momentum microscopy, the data treatment techniques were discussed extensively. These chapters demonstrated how the Single Event Data frame (SED) can be used to retain information on the detected electrons throughout an experiment, together with all relevant parameters which might be used to define its state (energy, momentum) or eventual system jitters and other parameters, such as pump laser fluence. It is then further described how all these parameters can be used to refine energy, momentum or time resolution, and how they can be used to calibrate the physical axes of interest.

Chapter 4 presents, in greater detail, these corrections and how they can be applied and described the methods available in the open-source package `hextof_processor`.[58] A rather substantial section was dedicated to the Space-Charge (SC) effect, given the strong impact it has on momentum microscopy and in particular on its time-resolved variant. Methods for correcting the energy shifts induced by the SC effects were also presented, together with the outlook towards the development of electron optics which would partially suppress SC, enabling time-resolved experiments with unprecedented high pump-fluences.

The data processing tools presented here are still only the start of a longer term project in which these data structures can be applied to multiple different microscopes, performing different variations of Multidimensional Photoemission Spectroscopy (MPES). To this end, the fusion between different projects, `hextof_processor` and `mpes` would certainly lead to improved computational performance as well as versatility, making it possible to apply the data processing methods on any type of single-event resolved data, as that acquired with delay-line-detectors (DLDs). Furthermore, reaching a community wide acceptance of a set of metadata descriptors would allow to extend automation of all these features across different research groups and institution with minimal human intervention. Such a standardization of the data acquisition and processing workflows will pave the way between experiments and F.A.I.R. and Artificial Intelligence (AI)-ready data.

The last two chapters illustrated and explained the two main research topics I investigated throughout my doctoral studies, and on which I developed many of the tools presented before.

First, the studies of the temperature at which the transition between large and small Fermi surface occurs in the Kondo compound $YbRh_2Si_2$, was presented. Although the energy resolution did not allow direct observation of the Fermi surface at all temperatures, a temperature for this transition (between 100 K and 200 K) could be identified.

This was achieved by tracking the changes in binding energy of the bands in the 1 eV to 0.4 eV binding energy range. The success is based on the fact that the hybridization, which gives rise to these changes, is the same that drives the change between small and large Fermi surfaces.

The most relevant aspects of these measurements arise from the choice of the hard X-ray photon energy, around 5 keV, which resulted in a large Field of View (FOV) in momentum space, resolving over 25 Brillouin Zones (BZs). By exploiting the changes in perpendicular momentum with increasing parallel momentum, the full 3D momentum space could be reconstructed simultaneously, without changing photon energy. Furthermore, the long mean-free-path of the electrons generated with such high kinetic energies provided greatly enhanced bulk sensitivity. These results can be seen as a proof-of-principle that bulk sensitive photoemission can be performed in such experiments, which is of great interest for research in systems where surface states might mask bulk properties, as well as for investigation of buried interfaces.

The data acquired for these experiments were originally recorded in an electron-resolved fashion, but converting the volumetric data to a tabular data structure similar to the Single Event Data frame (SED) allowed the same processing methods to be used.

Finally, the work done on the parent compound of the high-temperature superconducting cuprates La_2CuO_4 (LCO) was presented. These results constitute the main experimental result of this Thesis. We used time-resolved momentum microscopy at FLASH, Deutsches Elektronen-Synchrotron (DESY), to study the effects of photodoping, i.e. excitation with above gap photons (3.1 eV).

Many challenges arose from these experiments, starting from the intrinsic difficulty of performing photoemission experiments on strongly correlated electron systems. The correlations in these systems induce a strong broadening of the bands, making it hard to detect symmetry points in momentum space. We were nonetheless able to identify momentum resolved features in good agreement with previous measurements.

The changes induced by the pump laser were very small, totalling 6 orders of magnitude less electrons per unit time and energy than in the unperturbed valence band region. In spite of that, applying all the jitter and artifact corrections, as well as the signal-to-noise ratio (SNR) enhancement methods described in Chapter 4, we were able to resolve a distinct time-resolved change in the electronic distribution, common to three different samples measured and evaluated independently.

These results support the theoretical picture where, upon photodoping, new electron states are formed inside the Mott-Hubbard gap, near the Fermi level. These are the states which at higher photo- or chemical doping will give rise to metallicity and host superconductivity below the superconducting transition temperature. Our results are in line with previous studies of core level shifts, indicating a different behaviour for La_2CuO_4 (LCO) compared to other cuprates, such as $Bi_2Sr_2CaCuO_{8+y}$ (Bi2212)[104] and $YBa_2Cu_3O_{7-y}$ (YBCO),[1] where instead, upon doping, a shift in the binding energy of the core levels is linked to a shift in the Fermi edge to the top of the valence band.

Laser fluctuations induced strong deviations from the expected pump fluence. Normally this would result in inconclusive data. However, exploiting the single-electron detection, where each detected electron was recorded together with the laser intensity in the pulse which affected it, we transformed such fluctuations in an effective fluence dependence study

This is a good example of how fluctuations of some experimental parameters, which typically would result in high noise, can instead be used to resolve changes along such dimensions. This is only possible when retaining full information of the acquired data, together with all the available parameters of the experimental apparatus. When integrating data over a quantity, as is commonly done in photoemission experiments, valuable information is lost. The same quantity could otherwise be used to filter out outliers, correct jitters and overall improve resolution and SNR.

APPENDIX A

Thin-film Sample holder

The design of a custom sample holder for the Se capped samples was necessary to ensure electrical contact between the LCO surface and the sample holder was retained after decapping. This is important when dealing with insulating samples, as the surface can charge positively when electrons are photoemitted and no compensation current from grounding can flow. A front and back view of this plate is shown in figure A.1

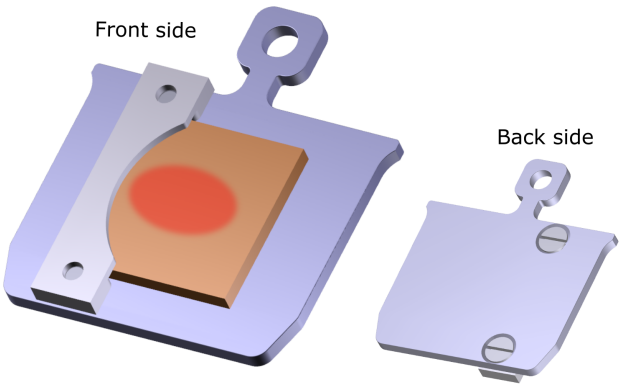

Figure A.1: Custom made flag style sample plate for thin films on 10 × 10 × 1 mm substrates. On the front side view, the sample (orange square) is held in place by a metal bracket. The screws holding the bracket are visible on the back side of the sample holder. The red area on the sample indicates the region of interest where the photoemission experiment can take place.

The experimental apparatus required use of a flag style Omicron plate. To mount the $10 \times 10 \times 1$ mm samples on these platelets, I designed a small side clamp which by tightening two screws on the back plate, would keep in place the sample while also ensuring electrical contact of the front surface with the bulk of the sample holder. Particular care was also taken to ensure the screws do not stick out of the back plate, as this needs to be completely flat in order to slide in the different sockets of sample cartridge as well as on the measurement position in front of the microscope.

Publications

The following is the list of published articles I authored during my doctoral studies.

[1] S. Y. Agustsson et al. "Temperature-dependent change of the electronic structure in the Kondo lattice system YbRh2Si2". *Journal of Physics Condensed Matter* **33** (2021), p. 205601. DOI: 10.1088/1361-648X/abe479.

[2] D. Curcio et al. "Ultrafast electronic linewidth broadening in the C core level of graphene". *Physical Review B* **104** (2021), pp. 1–16. DOI: 10.1103/PhysRevB.104.L161104.

[3] F. Pressacco et al. "Subpicosecond metamagnetic phase transition in FeRh driven by non-equilibrium electron dynamics". *Nature Communications* **12** (2021), p. 5088. DOI: 10.1038/s41467-021-25347-3.

[4] G. Schönhense et al. "Suppression of the vacuum space-charge effect in fs-photoemission by a retarding electrostatic front lens". *Review of Scientific Instruments* **92** (2021), p. 053703. DOI: 10.1063/5.0046567.

[5] A. R. Pokharel et al. "Robust hybridization gap in the Kondo insulator Yb B12 probed by femtosecond optical spectroscopy". *Physical Review B* **103** (2021), p. 115134. DOI: 10.1103/PhysRevB.103.115134.

[6] R. P. Xian et al. "An open-source, end-to-end workflow for multidimensional photoemission spectroscopy". *Scientific Data* **7** (2020), p. 442. DOI: 10.1038/s41597-020-00769-8.

[7] H. J. Elmers et al. "Néel Vector Induced Manipulation of Valence States in the Collinear Antiferromagnet Mn2Au". *ACS Nano* **14** (2020), pp. 17554–17564. DOI: 10.1021/acsnano.0c08215.

[8] O. Fedchenko et al. "Emitter-site specificity of hard X-ray photoelectron Kikuchi-diffraction". *New Journal of Physics* **22** (2020), p. 103002. DOI: 10.1088/1367-2630/abb68b.

[9] M. Dendzik et al. "Observation of an Excitonic Mott Transition through Ultrafast Core- cum -Conduction Photoemission Spectroscopy". *Physical Review Letters* **125** (2020), p. 096401. DOI: 10.1103/PhysRevLett.125.096401.

[10] D. Kutnyakhov et al. "Time- And momentum-resolved photoemission studies using time-of-flight momentum microscopy at a free-electron laser". *Review of Scientific Instruments* **91** (2020), p. 013109. DOI: 10.1063/1.5118777.

Bibliography

[1] K. Maiti et al. “Doping dependence of the chemical potential and surface electronic structure in YBa2 Cu3 O6+x and La2-x Srx CuO4 using hard x-ray photoemission spectroscopy”. *Physical Review B - Condensed Matter and Materials Physics* **80** (2009), pp. 1–16. DOI: 10.1103/PhysRevB.80.165132.

[2] S. Y. Agustsson et al. “Temperature-dependent change of the electronic structure in the Kondo lattice system YbRh2Si2”. *Journal of Physics Condensed Matter* **33** (2021), p. 205601. DOI: 10.1088/1361-648X/abe479.

[3] H. Okamoto et al. “Ultrafast charge dynamics in photoexcited Nd2 CuO4 and La2 CuO4 cuprate compounds investigated by femtosecond absorption spectroscopy”. *Physical Review B - Condensed Matter and Materials Physics* **82** (2010), p. 060513. DOI: 10.1103/PhysRevB.82.060513.

[4] A. Pokharel et al. “Light induced holon-doublon dynamics in the charge transfer insulator La2CuO4”. *in preparation* (2022).

[5] A. Agrawal and A. Choudhary. “Perspective: Materials informatics and big data: Realization of the "fourth paradigm" of science in materials science”. *APL Materials* **4** (2016), p. 053208. DOI: 10.1063/1.4946894.

[6] C. Draxl and M. Scheffler. “The NOMAD laboratory: From data sharing to artificial intelligence”. *JPhys Materials* **2** (2019), p. 036001. DOI: 10.1088/2515-7639/ab13bb.

[7] A. Zakutayev et al. “An open experimental database for exploring inorganic materials”. *Scientific Data* **5** (2018). DOI: 10.1038/sdata.2018.53.

[8] A. Jain et al. *Commentary: The materials project: A materials genome approach to accelerating materials innovation*. 2013. DOI: 10.1063/1.4812323.

[9] S. Curtarolo et al. “AFLOWLIB.ORG: A distributed materials properties repository from high-throughput ab initio calculations”. *Computational Materials Science* **58** (2012), pp. 227–235. DOI: 10.1016/j.commatsci.2012.02.002.

[10] J. E. Saal et al. “Materials design and discovery with high-throughput density functional theory: The open quantum materials database (OQMD)”. *JOM* **65** (2013), pp. 1501–1509. DOI: 10.1007/s11837-013-0755-4.

[11] M. D. Wilkinson et al. “Comment: The FAIR Guiding Principles for scientific data management and stewardship”. *Scientific Data* **3** (2016), p. 160018. DOI: 10.1038/sdata.2016.18.

[12] J. M. Perkel. “Workflow systems turn raw data into scientific knowledge”. *Nature* **573** (2019), pp. 149–150. DOI: 10.1038/d41586-019-02619-z.

[13] F. Pressacco et al. “Subpicosecond metamagnetic phase transition in FeRh driven by non-equilibrium electron dynamics”. *Nature Communications* **12** (2021), p. 5088. DOI: 10.1038/s41467-021-25347-3.

[14] F. Pressacco et al. “Laser induced phase transition in epitaxial FeRh layers studied by pump-probe valence band photoemission”. *Structural Dynamics* **5** (2018), pp. 1–11. DOI: 10.1063/1.5027809.

[15] M Cardona and L Ley. *Photoemission in Solids I - General Principles*. 1978.

[16] F. Reinert and S. Hüfner. “Photoemission spectroscopy - From early days to recent applications”. *New Journal of Physics* **7** (2005), pp. 97–97. DOI: 10.1088/1367-2630/7/1/097.

[17] B. Lv, T. Qian, and H. Ding. “Angle-resolved photoemission spectroscopy and its application to topological materials”. *Nature Reviews Physics* **1** (2019), pp. 609–626. DOI: 10.1038/s42254-019-0088-5.

[18] N. Gedik and I. Vishik. “Photoemission of quantum materials”. *Nature Physics* **13** (2017), pp. 1029–1033. DOI: 10.1038/nphys4273.

[19] J. G. Bednorz and K. A. Müller. “Possible high Tc superconductivity in the Ba-La-Cu-O system”. *Zeitschrift für Physik B Condensed Matter* **64** (1986), pp. 189–193. DOI: 10.1007/BF01303701.

[20] H. Hertz. “Ueber einen Einfluss des ultravioletten Lichtes auf die electrische Entladung”. *Annalen der Physik* **267** (1887), pp. 983–1000.

[21] A. Einstein. “Über einen die Erzeugung und Verwandlung des Lichtes betreffenden heuristischen Gesichtspunkt”. *Annalen der Physik* **322** (1905), pp. 132–148. DOI: 10.1002/andp.19053220607.

[22] R. A. Millikan. “On the elementary electrical charge and the avogadro constant”. *Physical Review* **2** (1913), pp. 109–143. DOI: 10.1103/PhysRev.2.109.

[23] S. Hüfner. “Introduction and Basic Principles”. 2003, pp. 1–60. DOI: 10.1007/978-3-662-09280-4{_}1.

[24] K. Medjanik et al. “Progress in HAXPES performance combining full-field k -imaging with time-of-flight recording”. *Journal of Synchrotron Radiation* **26** (2019), pp. 1996–2012. DOI: 10.1107/S1600577519012773.

[25] M. Ossiander et al. “Absolute timing of the photoelectric effect”. *Nature* **561** (2018), pp. 374–377. DOI: 10.1038/s41586-018-0503-6.

[26] S. Doniach and M. Sunjic. “Many-electron singularity in X-ray photoemission and X-ray line spectra from metals”. *Journal of Physics C: Solid State Physics* **3** (1970), pp. 285–291. DOI: 10.1088/0022-3719/3/2/010.

[27] S. D. Kevan. *Angle-Resolved Photoemission: Theory and Current Applications*. Elsevier, 1992, p. 628.

[28] C. Kittel and D. F. Holcomb. *Introduction to Solid State Physics*. Vol. 35. 1967, pp. 547–548. DOI: 10.1119/1.1974177.

[29] M. S. Rogalski and S. B. Palmer. *Solid state physics*. 2014. DOI: 10.1201/9781482283037.

[30] S. Suga and A. Sekiyama. "Photoelectron spectroscopy: Bulk and surface electronic structures". *Springer Series in Optical Sciences* **176** (2014), pp. 1–396. DOI: 10.1007/978-3-642-37530-9.

[31] K. Siegbahn and C. Nordling. "ESCA, atomic, molecular and solid state structure studied by means of electron spectroscopy". *Nov. Act. Uppsaliensis* (1967).

[32] N. Mårtensson et al. "A very high resolution electron spectrometer". *Journal of Electron Spectroscopy and Related Phenomena* **70** (1994), pp. 117–128. DOI: 10.1016/0368-2048(94)02224-N.

[33] V. N. Strocov et al. "Three-dimensional electron realm in VSe 2 by soft-x-ray photoelectron spectroscopy: Origin of charge-density waves". *Physical Review Letters* **109** (2012), p. 086401. DOI: 10.1103/PhysRevLett.109.086401.

[34] H. Iwasawa. "High-resolution angle-resolved photoemission spectroscopy and microscopy". *Electronic Structure* **2** (2020), p. 043001. DOI: 10.1088/2516-1075/abb379.

[35] G. Schönhense, K. Medjanik, and H. J. Elmers. "Space-, time- and spin-resolved photoemission". *Journal of Electron Spectroscopy and Related Phenomena* **200** (2015), pp. 94–118. DOI: 10.1016/j.elspec.2015.05.016.

[36] A. Winkelmann et al. "Momentum-resolved photoelectron interference in crystal surface barrier scattering". *Physical Review B - Condensed Matter and Materials Physics* **86** (2012), p. 085427. DOI: 10.1103/PhysRevB.86.085427.

[37] A. Winkelmann et al. "Analysis of the electronic structure of copper via two-dimensional photoelectron momentum distribution patterns". *New Journal of Physics* **14** (2012), p. 043009. DOI: 10.1088/1367-2630/14/4/043009.

[38] E. Bauer. "The resolution of the low energy electron reflection microscope". *Ultramicroscopy* **17** (1985), pp. 51–56. DOI: 10.1016/0304-3991(85)90176-7.

[39] E. Bauer. "Low energy electron microscopy". *Reports on Progress in Physics* **57** (1994), pp. 895–938. DOI: 10.1088/0034-4885/57/9/002.

[40] A. Oelsner et al. "Microspectroscopy and imaging using a delay line detector in time-of-flight photoemission microscopy". *Review of Scientific Instruments* **72** (2001), pp. 3968–3974. DOI: 10.1063/1.1405781.

[41] A. Oelsner et al. "Time- and energy resolved photoemission electron microscopy-imaging of photoelectron time-of-flight analysis by means of pulsed excitations". *Journal of Electron Spectroscopy and Related Phenomena* **178-179** (2010), pp. 317–330. DOI: 10.1016/j.elspec.2009.10.008.

[42] *www.surface-concept.com*. 2021.

[43] D. Kutnyakhov et al. "Time- And momentum-resolved photoemission studies using time-of-flight momentum microscopy at a free-electron laser". *Review of Scientific Instruments* **91** (2020), p. 013109. DOI: 10.1063/1.5118777.

[44] W. Ackermann et al. "Operation of a free-electron laser from the extreme ultraviolet to the water window". *Nature Photonics* **1** (2007), pp. 336–342. DOI: 10.1038/nphoton.2007.76.

[45] S. Schreiber and B. Faatz. "The free-electron laser FLASH". *High Power Laser Science and Engineering* **3** (2015), e20. DOI: 10.1017/hpl.2015.16.

[46] K. Tiedtke et al. "The soft x-ray free-electron laser FLASH at DESY: Beamlines, diagnostics and end-stations". *New Journal of Physics* **11** (2009), p. 023029. DOI: 10.1088/1367-2630/11/2/023029.

[47] J. Feldhaus. "FLASH-the first soft x-ray free electron laser (FEL) user facility". *Journal of Physics B: Atomic, Molecular and Optical Physics* **43** (2010). DOI: 10.1088/0953-4075/43/19/194002.

[48] C. Pagani. "Developments and achievements at the TESLA Test Facility (TTF)". *IEEE Transactions on Applied Superconductivity* **9** (1999), pp. 276–281. DOI: 10.1109/77.783289.

[49] B. Faatz et al. "Simultaneous operation of two soft x-ray free-electron lasers driven by one linear accelerator". *New Journal of Physics* **18** (2016), p. 62002. DOI: 10.1088/1367-2630/18/6/062002.

[50] F. Sorgenfrei et al. "The extreme ultraviolet split and femtosecond delay unit at the plane grating monochromator beamline PG2 at FLASH". *Review of Scientific Instruments* **81** (2010), p. 043107. DOI: 10.1063/1.3374166.

[51] M. Martins et al. "Monochromator beamline for FLASH". *Review of Scientific Instruments* **77** (2006), p. 115108. DOI: 10.1063/1.2364148.

[52] N. Gerasimova, S. Dziarzhytski, and J. Feldhaus. "The monochromator beamline at FLASH: Performance, capabilities and upgrade plans". *Journal of Modern Optics* **58** (2011), pp. 1480–1485. DOI: 10.1080/09500340.2011.588344.

[53] S. Düsterer et al. "Spectroscopic characterization of vacuum ultraviolet free electron laser pulses". *Optics Letters* **31** (2006), p. 1750. DOI: 10.1364/ol.31.001750.

[54] H. Redlin et al. "The FLASH pumpprobe laser system: Setup, characterization and optical beamlines". *Nuclear Instruments and Methods in Physics Research, Section A: Accelerators, Spectrometers, Detectors and Associated Equipment* **635** (2011), S88–S93. DOI: 10.1016/j.nima.2010.09.159.

[55] M. Seidel et al. "Ultrafast MHz-rate burst-mode pump-probe laser for the FLASH FEL facility based on nonlinear compression of ps-level pulses from an Yb-amplifier chain" (2021).

[56] S. Schulz et al. "Femtosecond all-optical synchronization of an X-ray free-electron laser". *Nature Communications* **6** (2015), p. 5938. DOI: 10.1038/ncomms6938.

[57] E. Savelyev et al. "Jitter-correction for IR/UV-XUV pump-probe experiments at the FLASH free-electron laser". *New Journal of Physics* **19** (2017), p. 043009. DOI: 10.1088/1367-2630/aa652d.

[58] S. Y. Agustsson et al. "momentoscope/hextof-processor: hextofprocessor-v1.0.4". *Zenodo* (2021). DOI: 10.5281/ZENODO.4651325.

[59] R. P. Xian et al. "An open-source, end-to-end workflow for multidimensional photoemission spectroscopy". *Scientific Data* **7** (2020), p. 442. DOI: 10.1038/s41597-020-00769-8.

[60] A Agababyan et al. *THE DATA ACQUISITION SYSTEM (DAQ) OF THE FLASH FACILITY*. Tech. rep.

[61] The HDF Group. *Hierarchical data format version 5, 2000-2010*. 2010.

[62] Dask Development Team. *Dask: Library for dynamic task scheduling*. 2016.

[63] C. R. Harris et al. *Array programming with NumPy*. 2020. DOI: 10.1038/s41586-020-2649-2.

[64] J. Reback et al. "pandas-dev/pandas: Pandas 1.3.5" (2021). DOI: 10.5281/zenodo.5774815.

[65] T. Pincelli, S. Y. Agustsson, and R. P. Xian. *openCOMPES*. 2021.

[66] M. Könnecke et al. "The NeXus data format". *Journal of Applied Crystallography* **48** (2015), pp. 301–305. DOI: 10.1107/S1600576714027575.

[67] G. Schönhense et al. "Correction of the deterministic part of space-charge interaction in momentum microscopy of charged particles". *Ultramicroscopy* **159** (2015), pp. 488–496. DOI: 10.1016/j.ultramic.2015.05.015.

[68] R. P. Xian, L. Rettig, and R. Ernstorfer. "Symmetry-guided nonrigid registration: The case for distortion correction in multidimensional photoemission spectroscopy". *Ultramicroscopy* **202** (2019), pp. 133–139. DOI: 10.1016/j.ultramic.2019.04.004.

[69] O. Schmidt et al. "The spatial distribution of non-linear effects in multi-photon photoemission from metallic adsorbates on Si(1 1 1)". *Surface Science*. Vol. 482-485. North-Holland, 2001, pp. 687–692. DOI: 10.1016/S0039-6028(01)00926-8.

[70] M. Dendzik et al. "Observation of an Excitonic Mott Transition through Ultrafast Core- cum -Conduction Photoemission Spectroscopy". *Physical Review Letters* **125** (2020), p. 096401. DOI: 10.1103/PhysRevLett.125.096401.

[71] B. Schönhense et al. "Multidimensional photoemission spectroscopy - The space-charge limit". *New Journal of Physics* **20** (2018), p. 033004. DOI: 10.1088/1367-2630/aaa262.

[72] G. Schönhense et al. "Suppression of the vacuum space-charge effect in fs-photoemission by a retarding electrostatic front lens". *Review of Scientific Instruments* **92** (2021), p. 053703. DOI: 10.1063/5.0046567.

[73] S. Seiro et al. "Evolution of the Kondo lattice and non-Fermi liquid excitations in a heavy-fermion metal". *Nature Communications* **9** (2018), pp. 1–7. DOI: 10.1038/s41467-018-05801-5.

[74] P. M. Rourke et al. "Magnetic-field dependence of the YbRh2Si2 fermi surface". *Physical Review Letters* **101** (2008), p. 237205. DOI: 10.1103/PhysRevLett.101.237205.

[75] R. M. Martin. "The Fermi surface and Fermi liquid properties of periodic Kondo and mixed valence systems". *Journal of Applied Physics* **53** (1982), pp. 2134–2136. DOI: 10.1063/1.330757.

[76] S. Danzenbächer et al. “Insight into the f-derived Fermi surface of the heavy-fermion compound YbRh 2Si 2”. *Physical Review Letters* **107** (2011), p. 267601. DOI: 10.1103/PhysRevLett.107.267601.

[77] M. Güttler et al. “Divalent EuRh 2 Si 2 as a reference for the Luttinger theorem and antiferromagnetism in trivalent heavy-fermion YbRh 2 Si 2”. *Nature Communications* **10** (2019), pp. 1–7. DOI: 10.1038/s41467-019-08688-y.

[78] P. W. Anderson. “Localized magnetic states in metals”. *Physical Review* **124** (1961), pp. 41–53. DOI: 10.1103/PhysRev.124.41.

[79] H. C. Choi et al. “Temperature-dependent Fermi surface evolution in heavy fermion CeIrIn 5”. *Physical Review Letters* **108** (2012), p. 016402. DOI: 10.1103/PhysRevLett.108.016402.

[80] K. Kummer et al. “Temperature-independent fermi surface in the kondo lattice YbRh2Si2”. *Physical Review X* **5** (2015), p. 011028. DOI: 10.1103/PhysRevX.5.011028.

[81] C. Krellner et al. “Single-crystal growth of YbRh2Si2 and YbIr 2Si2”. *Philosophical Magazine*. Vol. 92. Taylor & Francis Group, 2012, pp. 2508–2523. DOI: 10.1080/14786435.2012.669066.

[82] D. V. Vyalikh et al. “Tuning the hybridization at the surface of a heavy-fermion system”. *Physical Review Letters* **103** (2009), p. 137601. DOI: 10.1103/PhysRevLett.103.137601.

[83] S. Danzenbächer et al. “Momentum dependence of 4f hybridization in heavy-fermion compounds: Angle-resolved photoemission study of YbIr2 Si2 and YbRh2 Si2”. *Physical Review B - Condensed Matter and Materials Physics* **75** (2007), p. 045109. DOI: 10.1103/PhysRevB.75.045109.

[84] S. Babenkov et al. “High-accuracy bulk electronic bandmapping with eliminated diffraction effects using hard X-ray photoelectron momentum microscopy”. *Communications Physics* **2** (2019), pp. 1–8. DOI: 10.1038/s42005-019-0208-7.

[85] P. A. Lindberg et al. “Photoemission studies of high-temperature superconductors”. *Surface Science Reports* **11** (1990), pp. 1–137. DOI: 10.1016/0167-5729(90)90002-U.

[86] A. Damascelli, Z. Hussain, and Z.-X. X. Shen. “Angle-resolved photoemission studies of the cuprate superconductors”. *Reviews of Modern Physics* **75** (2003), pp. 473–541. DOI: 10.1103/RevModPhys.75.473.

[87] P. A. Lee, N. Nagaosa, and X.-G. G. Wen. “Doping a Mott insulator: Physics of high-temperature superconductivity”. *Reviews of Modern Physics* **78** (2006), pp. 17–85. DOI: 10.1103/RevModPhys.78.17.

[88] M. Imada, A. Fujimori, and Y. Tokura. *Metal-insulator transitions*. 1998. DOI: 10.1103/revmodphys.70.1039.

[89] G. R. Stewart. “Unconventional superconductivity”. *Advances in Physics* **66** (2017), pp. 75–196. DOI: 10.1080/00018732.2017.1331615.

[90] I. M. Vishik. *Photoemission perspective on pseudogap, superconducting fluctuations, and charge order in cuprates: A review of recent progress*. 2018. DOI: 10.1088/1361-6633/aaba96.

[91] K. Maki. "Introduction to d-wave superconductivity". *AIP Conference Proceedings*. Vol. 438. American Institute of PhysicsAIP, 1998, pp. 83–128. DOI: 10.1063/1.56343.

[92] T. Timusk and B. Statt. "The pseudogap in high-temperature superconductors: An experimental survey". *Reports on Progress in Physics* **62** (1999), pp. 61–122. DOI: 10.1088/0034-4885/62/1/002.

[93] D. C. Peets et al. "Tl2Ba2CuO6+δ brings spectroscopic probes deep into the overdoped regime of the high-Tc cuprates". *New Journal of Physics* **9** (2007), p. 28. DOI: 10.1088/1367-2630/9/2/028.

[94] J. Bardeen, L. N. Cooper, and J. R. Schrieffer. "Microscopic Theory of Superconductivity". *Physical Review* **106** (1957), pp. 162–164. DOI: 10.1103/PhysRev.106.162.

[95] P. W. Anderson. "The resonating valence bond state in La2CuO4 and superconductivity". *Science* **235** (1987), pp. 1196–1198. DOI: 10.1126/science.235.4793.1196.

[96] N. M. Plakida. *High-Temperature Superconductivity*. Berlin, Heidelberg: Springer Berlin Heidelberg, 1995. DOI: 10.1007/978-3-642-78406-4.

[97] R. Micnas, J. Ranninger, and S. Robaszkiewicz. "Superconductivity in narrow-band systems with local nonretarded attractive interactions". *Reviews of Modern Physics* **62** (1990), pp. 113–171. DOI: 10.1103/RevModPhys.62.113.

[98] E. Kaldis, E. Liarokapis, and K. A. Müller, eds. *High-Tc Superconductivity 1996: Ten Years after the Discovery*. Dordrecht: Springer Netherlands, 1997. DOI: 10.1007/978-94-011-5554-0.

[99] E. Sigmund and K. A. Müller. *Phase Separation in Cuprate Superconductors*. Ed. by E. Sigmund and K. A. Müller. Berlin, Heidelberg: Springer Berlin Heidelberg, 1994. DOI: 10.1007/978-3-642-78805-5.

[100] N. F. Mott. "The basis of the electron theory of metals, with special reference to the transition metals". *Proceedings of the Physical Society. Section A* **62** (1949), pp. 416–422. DOI: 10.1088/0370-1298/62/7/303.

[101] P. W. Anderson. "New approach to the theory of superexchange interactions". *Physical Review* **115** (1959), pp. 2–13. DOI: 10.1103/PhysRev.115.2.

[102] J Hubbard. "Electron correlations in narrow energy bands III. An improved solution". *Proceedings of the Royal Society of London. Series A. Mathematical and Physical Sciences* **281** (1964), pp. 401–419. DOI: 10.1098/rspa.1964.0190.

[103] F. C. Zhang and T. M. Rice. "Effective Hamiltonian for the superconducting Cu oxides". *Physical Review B* **37** (1988), pp. 3759–3761. DOI: 10.1103/PhysRevB.37.3759.

[104] M. A. Van Veenendaal, G. A. Sawatzky, and W. A. Groen. "Electronic structure of Bi2Sr2Ca1-xYxCu2O8+δ: Cu 2p x-ray-photoelectron spectra and occupied and unoccupied low-energy states". *Physical Review B* **49** (1994), pp. 1407–1416. DOI: 10.1103/PhysRevB.49.1407.

[105] S. Uchida et al. "Optical spectra of La2-xSrxCuO4: Effect of carrier doping on the electronic structure of the CuO2 plane". *Physical Review B* **43** (1991), pp. 7942–7954. DOI: 10.1103/PhysRevB.43.7942.

[106] E. Dagotto et al. "Optical conductivity of the two-dimensional Hubbard model". *Physical Review B* **45** (1992), pp. 10107–10110. DOI: 10.1103/PhysRevB.45.10107.

[107] A. Comanac et al. "Optical conductivity and the correlation strength of high-temperature copper-oxide superconductors". *Nature Physics* **4** (2008), pp. 287–290. DOI: 10.1038/nphys883.

[108] D. S. Fisher, G. Kotliar, and G. Moeller. "Midgap states in doped Mott insulators in infinite dimensions". *Physical Review B* **52** (1995), pp. 17112–17118. DOI: 10.1103/PhysRevB.52.17112.

[109] J. Wagner, W. Hanke, and D. J. Scalapino. "Optical, magnetic, and single-particle excitations in the multiband Hubbard model for cuprate superconductors". *Physical Review B* **43** (1991), pp. 10517–10529. DOI: 10.1103/PhysRevB.43.10517.

[110] A. S. Alexandrov and P. E. Kornilovitch. "Mobile small polaron". *Physical Review Letters* **82** (1999), pp. 807–810. DOI: 10.1103/PhysRevLett.82.807.

[111] J. T. Devreese and A. S. Alexandrov. "Fröhlich polaron and bipolaron: Recent developments". *Reports on Progress in Physics* **72** (2009), p. 066501. DOI: 10.1088/0034-4885/72/6/066501.

[112] O. Rösch et al. "Polaronic behavior of undoped high-Tc cuprate superconductors from angle-resolved photoemission spectra". *Physical Review Letters* **95** (2005), p. 227002. DOI: 10.1103/PhysRevLett.95.227002.

[113] A. S. Mishchenko et al. "Charge dynamics of doped holes in high Tc cuprate superconductors: A clue from optical conductivity". *Physical Review Letters* **100** (2008), pp. 1–4. DOI: 10.1103/PhysRevLett.100.166401.

[114] J. M. Ginder et al. "Photoexcitations in La2CuO4: 2-eV energy gap and long-lived defect states". *Physical Review B* **37** (1988), pp. 7506–7509. DOI: 10.1103/PhysRevB.37.7506.

[115] H. Okamoto et al. "Photoinduced transition from Mott insulator to metal in the undoped cuprates Nd2CuO4 and La2CuO4". *Physical Review B - Condensed Matter and Materials Physics* **83** (2011), pp. 1–10. DOI: 10.1103/PhysRevB.83.125102.

[116] T Miyamoto et al. "Probing ultrafast spin-relaxation and precession dynamics in a cuprate Mott insulator with seven-femtosecond optical pulses". *Nature Communications* (2018). DOI: 10.1038/s41467-018-06312-z.

[117] L. Chaix et al. "Resonant inelastic x-ray scattering studies of magnons and bimagnons in the lightly doped cuprate La2-xSrxCuO4". *Physical Review B* **97** (2018), p. 155144. DOI: 10.1103/PhysRevB.97.155144.

[118] H. Wang et al. “Doping enhanced ferromagnetism and induced half-metallicity in CrI3 monolayer”. *Epl* **114** (2016), pp. 3–6. DOI: 10.1209/0295-5075/114/47001.

[119] M. Horio et al. “Angle-resolved photoemission spectroscopy of the low-energy electronic structure of superconducting Pr2CuO4 driven by oxygen nonstoichiometry”. *Physical Review B* **98** (2018), p. 020505. DOI: 10.1103/PhysRevB.98.020505.

[120] Z. X. Shen et al. “Anderson Hamiltonian description of the experimental electronic structure and magnetic interactions of copper oxide superconductors”. *Physical Review B* **36** (1987), pp. 8414–8428. DOI: 10.1103/PhysRevB.36.8414.

[121] R. L. Kurtz et al. “Electronic structure of high-Tc superconductors studied using photoelectron spectroscopy”. *Vacuum* **39** (1989), pp. 611–615. DOI: 10.1016/0042-207X(89)90002-X.

[122] M. Eichberger et al. “Snapshots of cooperative atomic motions in the optical suppression of charge density waves”. *Nature* **468** (2010), pp. 799–802. DOI: 10.1038/nature09539.

[123] S. Ono, S. Komiya, and Y. Ando. “Strong charge fluctuations manifested in the high-temperature Hall coefficient of high- Tc cuprates”. *Physical Review B - Condensed Matter and Materials Physics* **75** (2007), p. 024515. DOI: 10.1103/PhysRevB.75.024515.

[124] H. I. Wei et al. “Electron Doping of the Parent Cuprate La2CuO4 without Cation Substitution”. *Physical Review Letters* **117** (2016), pp. 1–7. DOI: 10.1103/PhysRevLett.117.147002.

[125] A. Ino et al. “Electronic structure of in the vicinity of the superconductor-insulator transition”. *Physical Review B - Condensed Matter and Materials Physics* **62** (2000), pp. 4137–4141. DOI: 10.1103/PhysRevB.62.4137.

[126] A. Ino et al. “Doping-dependent evolution of the electronic structure of (formula presented) in the superconducting and metallic phases”. *Physical Review B - Condensed Matter and Materials Physics* **65** (2002), pp. 1–11. DOI: 10.1103/PhysRevB.65.094504.

[127] T. Yoshida et al. “Systematic doping evolution of the underlying Fermi surface of La2-x Srx Cu O4”. *Physical Review B* **74** (2006), p. 224510. DOI: 10.1103/PhysRevB.74.224510.

Acknowledgements

Omitted in online version

Curriculum Vitae

Omitted in online version

Omitted in online version